The Pennsylvania State University

The Graduate School

College of Engineering

ADVANCED MEMBRANE ELECTRODE ASSEMBLIES FOR FUEL AND WATER MANAGEMENT IN DIRECT METHANOL FUEL CELLS

A Dissertation in

Mechanical Engineering

by

Christian E. Shaffer

Submitted in Partial Fulfillment
of the Requirements
for the Degree of

Doctor of Philosophy

August 2010

The dissertation of Christian E. Shaffer was reviewed and approved* by the following:

Chao-Yang Wang
Distinguished Professor of Mechanical and Chemical Engineering
Professor of Materials Science and Engineering
Dissertation Adviser
Chair of Committee

Fan-Bill Cheung
Professor of Mechanical and Nuclear Engineering

Robert J. Santoro
Professor of Mechanical Engineering

Ali Borhan
Professor of Chemical Engineering

Karen A. Thole
Professor of Mechanical Engineering
Head of the Department of Mechanical and Nuclear Engineering

*Signatures are on file in the Graduate School.

Abstract

The direct methanol fuel cell (DMFC) is being developed as a mobile power source for portable electronic devices, such as laptop computers and cellular telephones. In these applications, where space is at a premium, DMFCs are seen as a good fit, due in large part to the high theoretical energy density of DMFCs, directly related to the liquid nature of methanol fuel. However, DMFCs suffer from a practical energy density far lower than the theoretical value. A significant factor leading to this discrepancy is the inability of DMFCs to directly and efficiently use concentrated fuel. Because methanol and water react on a one-to-one molar basis in the methanol oxidation reaction in the anode, and because three moles of water are produced by the oxygen reduction reaction in the cathode for every one mole consumed in the anode, fuel (methanol) and water management are intricately tied together. In the work presented, a 1D, two-phase computational model is used to first explain fundamentally this intricate coupling between fuel and water management, and specifically how it relates to proper membrane electrode assembly (MEA) design. Next, a theoretical explanation is given as to how the inclusion of a hydrophobic anode micro-porous layer (MPL) is effective in reducing water crossover to the cathode, which is a prerequisite for the use of more highly concentrated fuel. Following this, a novel MEA design is described, incorporating an anode transport barrier, which in conjunction with the anode MPL facilitates the direct and efficient use of concentrated methanol fuel. Finally, we show that the membrane selectivity, the ratio of the membrane's ionic conductivity to methanol permeability, traditionally used as a membrane figure of merit to predict performance, is not overly

accurate. We demonstrate that a more inclusive figure of merit must also incorporate water transport characteristics of the membrane.

Table of Contents

List of Figures

List of Tables

Nomenclature

Acronyms and abbreviations

aBL	anode backing layer
aCL	anode catalyst layer
aMPL	anode micro-porous layer
aTB	anode transport barrier
BL	backing layer
cBL	cathode backing layer
cCL	cathode catalyst layer
cMPL	cathode micro-porous layer
CL	catalyst layer
DEFC	direct ethanol fuel cell
DMFC	direct methanol fuel cell
EOD	electro-osmotic drag
FOM	figure of merit
GDL	gas diffusion layer
HC-MFC	high concentration methanol fuel cell
HP	hydraulic permeation
MeOH	methanol (also CH_3OH)
MCO	methanol crossover ratio
MEA	membrane electrode assembly
MOR	methanol oxidation reaction

MPL	micro-porous layer
ORR	oxygen reduction reaction
PEFC	polymer electrolyte fuel cell
PEMFC	polymer electrolyte membrane fuel cell
PFSA	perfluorosulfonic acid
Pt	platinum
PTFE	polytetrafluoroethelene
Ru	ruthenium
SEM	scanning electron microscopy
STP	standard temperature and pressure (1 atm, 298 K)

Symbols

a	activity, volume specific reaction area, coefficient for c_{sat}^{H2O} correlation
$A_{m,a}$	mass-specific reaction area of catalyst (m^2 kg^{-1})
b	generic tafel slope, coefficient for c_{sat}^{H2O} correlation
c	molar concentration (mol m^{-3}or M)
D	diffusivity
E	electrical potential (V)
E^o	thermodynamic (reversible) cell potential at STP (V)
$E_{a,a}$	activation energy for MOR reaction (J mol^{-1})
E_T	thermodynamic (reversible) cell potential at temperature T (V)
EW	equivalent weight (kg/mol SO_3^-)
F	Faraday's constant; F = 96,485 C/mol charge

g	Gibbs free energy per mole of MeOH reacted (J $mol^{-1}K^{-1}$)
G	Gibbs free energy (Gibbs function) (J K^{-1})
h	enthalpy per mole of MeOH reacted (J mol^{-1})
H	enthalpy (J)
i	cell average current density (A m^{-2}), based on cell cross-sectional area
i_o	superficial exchange current density (A m^{-2})
$i_{ref,a}$	anode reference current density for anode stoichiometry (A m^{-2})
$i_{ref,c}$	cathode reference current density for cathode stoichiometry (A m^{-2})
$\tilde{i}_{o,ref}$	reference intrinsic (per reaction surface area) exchange current density(Am^{-2})
i_x	cross-over current density (A m^{-2}), based on cell cross-sectional area
I	cell current (A)
I_x	crossover current (A)
j	volumetric current density (A m^{-3})
$j_{cathode}^{ORR,H^+,Mem}$	volumetric ORR current in cathode coming from H^+ crossing membrane
$j_{cathode}^{MOR}$	volumetric MOR rate
$j_{cathode}^{ORR}$	volumetric ORR rate
J	Leverette function
k_H	Henry's constant
k_{rl}	relative liquid-phase permeability
M	molecular weight (g mol^{-1})
n	moles, exponent for effective diffusivity and MOR reaction kinetics
n_d	drag coefficient

N	molar flux (mol m^{-2} s^{-1})
N_{Mem}^{H2O}	membrane H_2O flux (mol m^{-2} s^{-1}), based on cell cross-sectional area
N_{Mem}^{MeOH}	membrane MeOH flux (mol m^{-2} s^{-1}), based on cell cross-sectional area
p	pressure
q	charge (C)
Q	heat (J)
r_{chem}	chemical reaction rate in the cathode catalyst layer (mol m^{-3} s)
R	universal gas constant
R_{cont}	contact resistance
s	entropy per mole of MeOH reacted (J mol^{-1} K^{-1}), liquid saturation
S	entropy (J K^{-1})
$\dot{S}'''$	volumetric source
T	temperature (K)
u	superficial velocity
U_o^{MOR}	standard equilibrium potential of methanol oxidation reaction (V)
U_o^{ORR}	standard equilibrium potential of oxygen reduction reaction (V)
V_{cath}	cathode potential (V)
V_{cell}	cell voltage (V)
w	work per mole MeOH reacted (J mol^{-1})
W	work (J)
x	through-plane coordinate direction
x_o^{MeOH}	location where MeOH ceases to exist in cathode catalyst layer
X	mole fraction

z^{MeOH}	moles of charge per mol of MeOH reacted
α	membrane net water transport coefficient
α_a	anodic charge transfer coefficient
α_c	cathodic charge transfer coefficient
δ	layer thickness (m)
Δ	out less in, and product state minus reactant state
ε	porosity
η	overpotential (V) or efficiency
κ^{H+}	ionic conductivity
K,κ	permeability (m^2)
λ	water content (mol H_2O/mol SO_3^-)
μ	viscosity
ν_i	stoichiometric coefficient of species i
θ	contact angle (degrees), surface coverage
ρ	density (kg m^{-3})
σ	surface tension (N m^{-1})
ω	catalyst loading (g m^{-2}) based on the cell cross-sectional area
ξ	stoichiometry

Subscripts

a	anode
aCL/Mem	anode catalyst layer and membrane interface
A,B	generic layers A, B
ads	adsorbed
bl	baseline
c	cathode, capillary
cCL/cMPL	cathode catalyst layer and cathode micro-porous later interface
diff	diffusion
eff	effective
elec	electrical
g	gas
in	into control volume
int	interface
l	liquid
max	maximum
Mem	membrane
Mem/cCL	membrane and cathode catalyst layer interface
o	reference
out	out of control volume
ref	reference
rev	reversible
rxn	reaction

sat	saturated gas-phase (equilibrium) value
t	total
thresh	threshold
volt	voltaic
xover	crossover
β	generic phase
Ω	ohmic

Superscripts and over-symbols

+	positive charge
-	negative charge
•	rate (per second)
o	standard state
‾	average value in cCL where MeOH is present
1,2	generic thermodynamic states
elec	electric
h	generic species
rxn	reaction
ψ	generic species

Acknowledgments

First and foremost I would like to thank Prof. Chao-Yang Wang for being such a great mentor, and for his support over the past few years. This work would not have been possible without his help, and I deeply appreciate everything he has done for me. I would also like to thank my committee members, Prof. Robert Santoro, Prof. Fan-Bill Cheung, and Prof. Ali Borhan, for their time and help. A great deal of thanks is due to members of the Electrochemical Engine Center for being such great co-workers, friends, and classmates. Additionally, the financial support of our ECEC sponsors is gratefully acknowledged. I would be remiss not to thank Dawn Fisher and Jenny Houser for all of their help over the years. Finally, I would like to thank my parents, sister and brother, and my fiancé Katie for their endless support, love, and encouragement.

The scientist does not study nature because it is useful; he studies it because he delights in it, and he delights in it because it is beautiful. If nature were not beautiful, it would not be worth knowing, and if nature were not worth knowing, life would not be worth living.

-- *Jules Henri Poincaré (1854-1912)*

Chapter 1. Introduction

In recent years there have been several factors which have lead to an increasing interest in fuel cell technology. Notably, the continued growing world demand for energy, the hope of a cleaner energy source to produce less pollution with a smaller impact on global warming, and the need to become more energy independent (U.S.) have lead to significant fanfare for fuel cell technology (see e.g. [1,2]). Most of this growing public attention has been centered on fuel cells designed for stationary and transportation applications. During this same time, there has also been a rapid, albeit less visible, development of mini- and micro- fuel cell technology primarily for portable consumer goods such laptops, cell phones, and PDAs, military equipment, and bio-medical devices such as pacemakers. In fact many consider mini- and micro-fuel cell technology as a developing replacement for lithium-ion (Li-on) batteries [3,4,5,6]).

Several types of fuel cells have been researched for use in the mini- and micro-fuel cell market including direct methanol fuel cells (DMFC), direct ethanol fuel cells (DEFC), and H_2/air polymer electrolyte fuel cells (PEFC or PEMFC). The major drawback of PEFCs is that they operate on gaseous hydrogen, which is the least dense gas in the universe. For portable applications of course this means that in comparison with methanol (MeOH, CH_3OH) or ethanol (which are both liquids under standard conditions), a much larger storage tank would be necessary leading to a much bulkier system. The hydrogen can be reformed on site from a hydrocarbon fuel such as methanol or even gasoline, but of course this process leads to more equipment and a larger parasitic load on the cell. Due to the liquid nature of the respective fuels, DMFCs and DEFCs bypass the storage issue encountered by H_2/air PEFCs. Additionally, in DMFCs and

DEFCs, the liquid fuels are used directly, electrochemically in the cell to produce electricity (no reformation or extra equipment needed). While DEFCs do have certain advantages over DMFCs such as the use of a non-poisonous fuel, the performance of DEFCs is currently not as good as the corresponding DMFC technology under similar conditions, due in large part to its very poor anode reaction kinetics (ethanol has a carbon-carbon bond which must be broken) [7].

1.1 Fuel cell history

The first concept of the fuel cell was developed in Great Britain by William R. Grove in 1839. In his original fuel cell Grove used dilute sulfuric acid as an electrolyte, along with two platinum electrodes, each covered by test tubes; the anode side electrode used hydrogen as a fuel, while the cathode side electrode used oxygen as an oxidizer [8]. Since Grove's original concept, many other types of cells have been investigated. Notable concepts and research include the direct coal fuel cell studied by A. C. Bacquerel, J. J. Jacques, and others in the mid- to late-1800s, and the H_2-O_2 cells worked on by W. Nernst in the early 1900s [8]. PEFCs were originally developed by General Electric and used in the NASA Gemini space missions in the mid-1960s [8,9]. For the Apollo space missions of the late 1960s and 70s, NASA opted to (very successfully) use alkaline fuel cells, researched extensively by Francis T. Bacon and others [9]. Starting in the late 1960s, significant research was performed with phosphoric acid fuel cells by Toshiba, United Technology Corporation (UTC), and others, but has waned recently.

Currently, most fuel cell research for stationary power generation is focused on solid oxide, polymer electrolyte, and to a lesser degree molten carbonate fuel cells. Research for residential and vehicular applications generally concentrates on PEFCs,

while DMFCs, PEFCs, and to a lesser degree DEFCs are the most widely researched for mini- and micro-fuel cell applications. In the roughly 170 years since Grove's first invention, many improvements and modifications have been made to the fuel cell concept, but the same basic principle still applies today: harness the electrical energy produced by flowing electrons generated by two half-cell electrochemical reactions. It should be noted that a fuel cell is distinguished from a battery in that (a) unlike a battery a fuel cell does not consume its electrodes, and (b) while a battery is a closed device which has fixed amount of mass, a fuel cell is inherently an open device for which the reactants must continuously be replenished and waste products removed.

1.2 DMFC basics

In a direct methanol fuel cell either pure oxygen, or more commonly oxygen in air, and methanol solution are reacted to generate electrical energy. For this process the basic half-cell and overall reactions are given by

$$CH_3OH + H_2O \rightarrow 6H^+ + 6e^- + CO_2 \quad (MOR) \tag{1.1a}$$

$$6H^+ + 6e^- + \left(3/2\right)O_2 \rightarrow 3H_2O \quad (ORR) \tag{1.1b}$$

$$CH_3OH + \left(3/2\right)O_2 \rightarrow 2H_2O + CO_2 \quad (overall) \tag{1.1c}$$

Here, the methanol oxidation reaction (MOR) occurs primarily on the anode side of the cell where the MeOH enters through the flow channel, and the oxygen reduction reaction (ORR) occurs on the cathode side of the cell, where air or O_2 is fed through the flow channel. A basic schematic of a classic DMFC design is given in Figure 1.1. The product carbon dioxide produced in the anode by the MOR reaction exits the cell via the anode flow channel, while the excess H_2O created in the cathode by the ORR reaction

exits through the cathode flow channel. The flow channels are machined into the bi-polar plates (also referred to as separator plates), which conduct the electrical current generated by the half-cell reactions, and hence are generally made of a graphite or metal (highly conductive) material. The designs of these bi-polar plates vary greatly, but all have "land regions" where the solid conducting material comes into direct contact with the porous media, and "channel regions" where the flowing fluid or ambient air is in direct contact with the porous media.

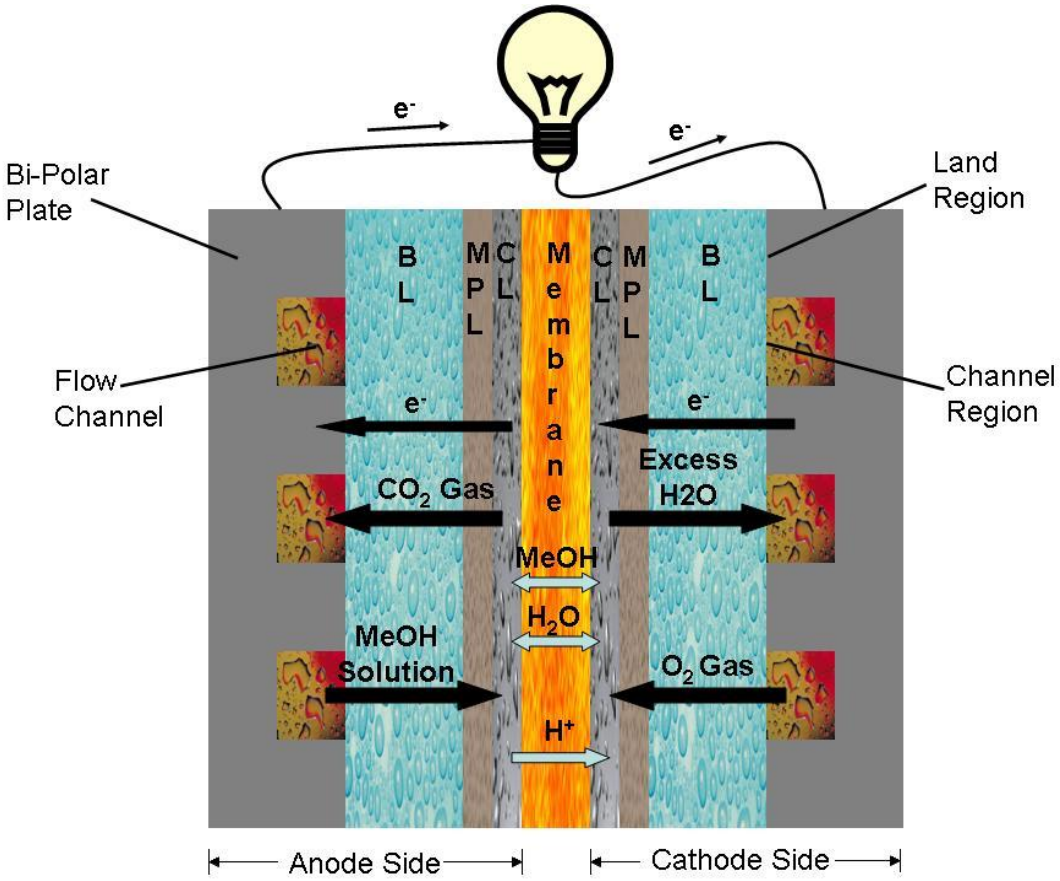

Figure 1.1. Generic force feed DMFC schematic.

The porous media on both sides of the cell serve two main purposes. First, they facilitate a more uniform fuel distribution into and product removal out of the catalyst layers. Secondly they make possible the lateral current collection from the catalyst layer

to the lands. In order to have a high electrical conductivity, the backing layers (BL), also referred to as gas diffusion layers (GDL), are generally made of a carbon material such as carbon paper or carbon cloth [10,11], which are shown in Figure 1.2. Also, as shown schematically in Figure 1.1, both the anode and cathode sides may also contain micro-porous layers (MPL). These layers can be tailored to improve certain desirable cell characteristics dealing with transport of fuel and water; the hydrophobic MPLs used in this work are typically made of a mixture of carbon black and polytetrafluoroethylene (PTFE, i.e. Teflon®). Figure 1.3 gives a scanning electron microscopy (SEM) image of a typical backing layer/micro-porous layer/catalyst layer; note that the typical thickness of a BL for a DMFC is roughly 200-400μm (the image in Figure 1.3 cuts off the backing layer) and the typical thickness of an MPL is generally 20μm and up.

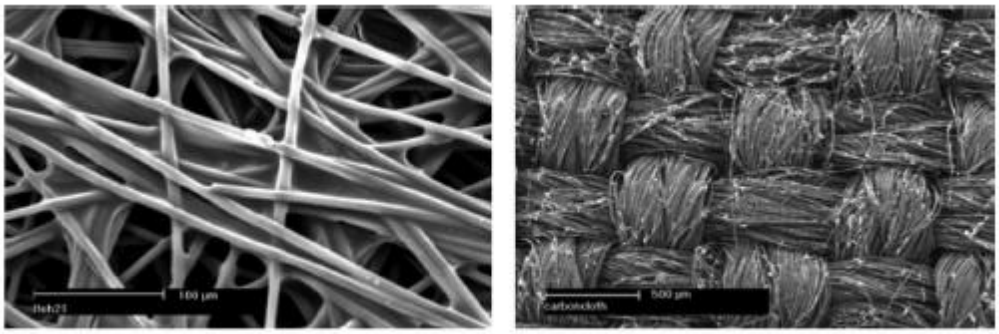

(a) (b)

Figure 1.2. SEM images of (a) carbon paper and (b) carbon cloth diffusion mediums [5].

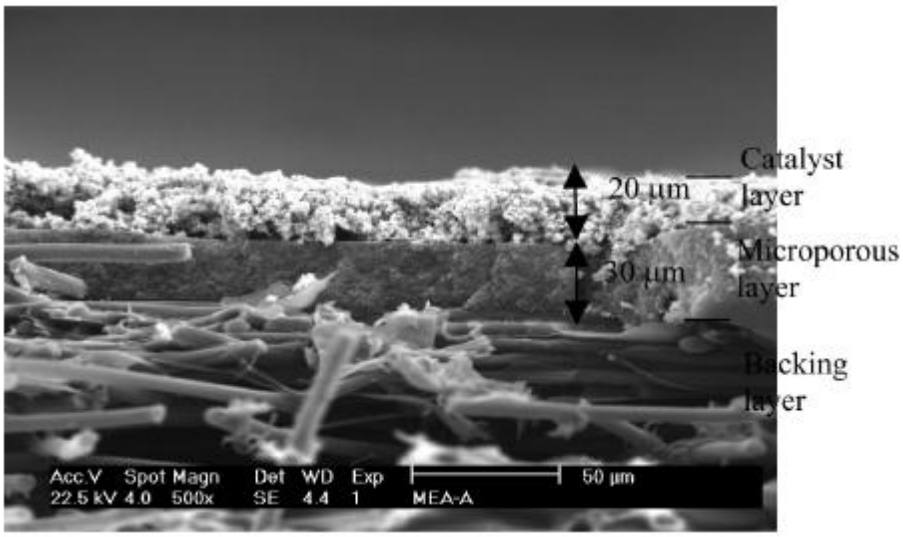

Figure 1.3. SEM image of typical backing layer/micro-porous layer/catalyst layer [5].

As depicted in figure 1.1, the membrane of the DMFC is sandwiched between the anode and cathode catalyst layers. In any type of fuel cell, the purpose of the membrane is to conduct the charge-carrying ions (in this case H^+), while simultaneously block electrons, thereby forcing them to travel through the external circuit. For a DMFC it is also highly desirable that the membrane block MeOH transport from the anode to cathode and facilitate back-transport of H_2O from cathode catalyst layer to anode catalyst layer. Most DMFC designs make use of a polymer membrane, such as Dupont's perfluorosulfonic acid (PFSA) Nafion®. The thickness of a DMFC membrane varies from design to design, but typically falls in the range between 25μm (Nafion® 112) and 175μm (Nafion® 117). A more detailed discussion of membranes, and how they are intricately tied with fuel and water management is given in section 1.9.

The catalyst layers (CL) of the fuel cell are where the actual half-cell reactions occur. These layers are very thin, generally only 10-20 μm. The primary reason for having a catalyst layer is to bring the ionic phase (H^+ ions), electronic phase (electrons,

e^-), and fuel together in one physical region in space, often referred to as the triple phase boundary, in order to allow the half-cell reactions (1.1a) and (1.1b) to take place. To this end, the catalyst layers are physically porous structures made of a complex mix of ionomer (membrane material), carbon (electronic conductor), and catalyst. An idealized depiction of a catalyst layer is given in Figure 1.4. The catalysts are necessary to reduce the activation energy; for a DMFC, Pt-Ru is generally used on the anode side, while Pt is typically used on the cathode side. Note that it is common for the membrane, CLs, MPLs, and BLs to be referred to as the membrane electrode assembly (MEA).

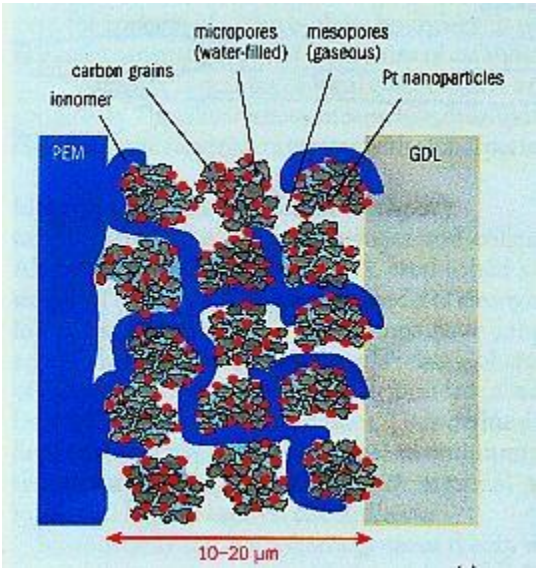

Figure 1.4. Idealized catalyst layer structure [12].

A few very important parameters for DMFCs are now defined, the significance of which will become clear in subsequent sections. The membrane net water transport coefficient, α, is defined as

$$\alpha = \frac{N_{Mem}^{H2O}}{i/F} \tag{1.2}$$

where $N_{Mem}^{H_2O}$ = net H_2O flux across the membrane, positive from anode to cathode (mol m^{-2} s^{-1})

F = Faraday's constant = 96,485 C mol ch.$^{-1}$

i = cell current density (A m^{-2} or C m^{-2} s^{-1})

It is evident from this definition that α is the net moles of H_2O transferred through the membrane (from anode to cathode) per mole of H^+ ions transferred through the membrane, i/F (see equations (1.1)). The crossover current density, i_x, is the equivalent current density that could be realized electrochemically if the MeOH crossover through the membrane, from the anode to cathode, were zero. By use of equations (1.1) the crossover current density is defined as

$$i_x = N_{Mem}^{MeOH} z^{MeOH} F \tag{1.3}$$

where N_{Mem}^{MeOH} = MeOH flux across the membrane (mol m^{-2} s^{-1})

z^{MeOH} = moles of electrons or H^+ transferred per mole of MeOH reacted

Alternatively, the MeOH crossing the membrane from anode to cathode can be described in terms of the methanol crossover ratio (MCO); the MCO is physically the fraction of MeOH fuel which is essentially wasted by crossing the membrane and reacting in the cathode, thereby not creating useable current.

$$MCO = \frac{i_x}{i + i_x} \tag{1.4}$$

The H_2O and MeOH fluxes, along with the current density and crossover current density are based on the cross-sectional area of the cell. Along with α and MCO, these parameters are, strictly speaking, local values, dependent upon the location within the cell. However, it is common simply to use these terms to refer to the average value (e.g., using the term "current density" to imply cell-averaged current density, or MCO to refer

to the average MCO). This convention will be adopted in this text; if it becomes necessary to discuss the local values of there parameters, it will be specifically noted.

The point should be made that the design and components of a DMFC are in many cases similar to those for an H_2/O_2 PEFC. Figure 1.1 basically holds true for a PEFC with the MeOH solution replaced by H_2 gas. While they may be designed in a slightly different manner, the BLs of a PEFC are generally made of carbon paper or carbon cloth, and use of MPL are also common. The PFSA membranes used for DMFCs and PEFCs are often times the same (e.g. Nafion® is commonly used in both DMFCs and PEFCs). While the PEFC cathode uses Pt as a catalyst (like the DMFC), the anode side generally uses Pt instead of Pt-Ru. Of course, other differences including auxiliary equipment external to the cell may exist, but due to the great number of similarities and extent of research done in the field of H_2/O_2 PEFCs, literature specifically written for H_2/O_2 PEFCs will be referred to throughout the text, where applicable.

1.3 Thermodynamics

In order to determine the upper limit on voltage from a fuel cell, one must turn to thermodynamics. A fuel cell can be analyzed utilizing a simple control volume as depicted in Figure 1.5. Applying the first law of thermodynamics and assuming a steady-state condition, the following equation can be derived:

$$\dot{W}_{out} = -\dot{Q}_{out} - \Delta\dot{H} \tag{1.5}$$

where $\dot{W}_{out}$ = rate of work being done by by the control volume (i.e. the fuel cell)

$\dot{Q}_{out}$ = rate of heat flowing out of control volume

$\Delta\dot{H} = \dot{H}_{out} - \dot{H}_{in}$, rate of enthalpy flowing out less rate of enthalpy flowing into control volume

For our purposes here, a fuel cell can well be approximated as isothermal. Using the average cell temperature, T, and using the thermodynamic relation G = H – TS, one can relate the change in enthalpy as

$$\Delta\dot{H} = \Delta\dot{G} + T\Delta\dot{S} \tag{1.6}$$

where $\Delta\dot{G} = \dot{G}_{out} - \dot{G}_{in}$ rate of Gibbs free energy flowing out less rate of Gibbs free energy flowing into control volume

T = average cell temperature

$\Delta\dot{S} = \dot{S}_{out} - \dot{S}_{in}$ rate of entropy flowing out less rate of entropy flowing into control volume

Inserting (1.6) into (1.5) yields the following expression:

$$\dot{W}_{out} = -\Delta\dot{G} - \left[\dot{Q}_{out} + T\Delta\dot{S}\right] \tag{1.7}$$

From the definition of entropy (see, e.g. [13]), we know that

$$S_2 - S_1 = -\left(\int_1^2 \frac{\delta Q}{T}\right)_{rev} \tag{1.8}$$

where 1 = generic thermodynamic state 1

2 = generic thermodynamic state 2

δQ = heat transferred ***out*** of the control volume at given boundary location

rev = reversible process (internally)

Approximating the cell as isothermal, replacing generic state 2 with the outlet state, and generic state 1 with the inlet state of the control volume given in Figure 1.5 yields

$$\dot{Q}_{rev} = -T\Delta\dot{S} \tag{1.9}$$

where Q_{rev} = heat transferred ***out*** of the control volume for an internally reversible process

Substituting (1.9) into (1.7) yields

$$\dot{W}_{out} = -\Delta\dot{G} - \left[\dot{Q}_{out} - \dot{Q}_{rev}\right] \tag{1.10}$$

We know from the second law of thermodynamics that the minimum possible amount of heat produced in moving from inlet to outlet states is realized for a reversible process. Therefore, the maximum amount of work that is possible is given when $\dot{Q}_{out} = \dot{Q}_{rev}$, or

$$\dot{W}_{\substack{out \\ \max}} = -\Delta\dot{G} \tag{1.11}$$

From this heuristic analysis it should now be evident that the maximum possible amount of work that can be obtained is equal to the change in the Gibbs free energy between outlet and inlet flows. Due to the reaction taking place inside the control volume, change in Gibbs free energy should be given by that of the reaction taking place. This being the case, dividing (1.11) by the molar flow of the MeOH reacted, we obtain

$$w_{\substack{out \\ \max}} = -\Delta g_{rxn} \tag{1.12}$$

where $w_{\substack{out \\ \max}}$ = maximum possible work output per mol of MeOH reacted

Δg_{rxn} = Gibbs free energy change for the reaction per mol of MeOH

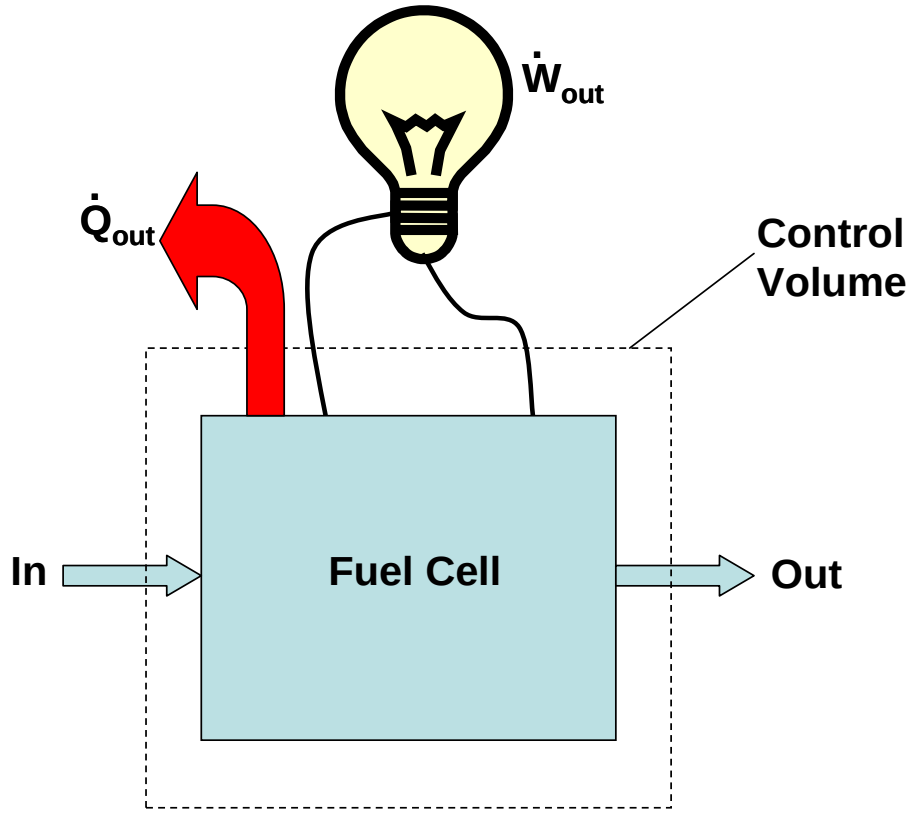

Figure 1.5. Control volume analysis of fuel cell for thermodynamic analysis.

The work required to move a charge q through a an electric potential difference E is given by (see, e.g. [14,15])

$$W_{elec} = Eq \tag{1.13}$$

where W_{elec} = electrical work required to move charge

Here, the charge q is measured in coulombs. The work in the external circuit is performed by electrons, which have a charge number of one (one mole of charge per mole of electrons). Therefore, the charge can be related to the moles of electrons carrying the charge, n_{e^-}, by

$$q = n_{e^-} F \tag{1.14}$$

Substituting (1.14) into (1.13) yields

$$W_{elec} = n_{e^-} EF \tag{1.15}$$

This expression can alternatively be written in rate form as

$$\dot{W}_{elec} = \dot{n}_{e^-} EF \tag{1.16}$$

where $\dot{n}_{e^-}$ = rate of electron flow (mol s^{-1})

Dividing (1.16) by the molar flow rate of fuel reacted, then equating with (1.12) yields the final expression which relates the thermodynamic (reversible) cell potential, E, with the Gibbs free energy of reaction:

$$E = \frac{-\Delta g_{rxn}}{\left(\dot{n}_{e^-} \Big/ \dot{n}_{MeOH} \right) F} \tag{1.17}$$

The term $\dot{n}_{e^-} \Big/ \dot{n}_{MeOH}$ stands for the moles of electrons transferred per mole of MeOH reacted, which we will define as z^{MeOH}. From equations (1.1) it is evident that for a DMFC, $z^{MeOH} = 6$, yielding

$$E = \frac{-\Delta g_{rxn}}{z^{MeOH} F} = \frac{-\Delta g_{rxn}}{6F} \tag{1.18}$$

At standard state conditions (STP: P = 1atm, T = 298K, 1M concentration), the reversible cell potential for the overall reaction given by (1.1c) is 1.21V [8]. In order to calculate the reversible cell potential at temperatures other than 298K, the thermodynamic relation $\left. \frac{\partial G}{\partial T} \right|_p = -S$ can be utilized along with (1.18) to give:

$$E_T = E^o + \left[\frac{\overline{\Delta s_{rxn}}}{z^{MeOH} F} \right] \left(T - T^o \right) \tag{1.19}$$

where E_T = thermodynamic cell potential at a given temperature, T, other conditions STP (V)

E^o = thermodynamic cell potential at STP (V)

$\overline{\Delta s_{rxn}}$ = average entropy change of reaction over ($T - T^o$)

Table 1.1 gives thermodynamic data for the overall reaction (1.1c). From this data, it can be shown that the reversible cell potential only decreases by about 10mV between 25°C (298K) and 100°C (373K). The typical operating range for DMFCs is between 40 and 100°C. Finally, to account for varying concentrations, the Nernst equation can be used [15]:

$$E = E_T - \left[\frac{RT}{z^{MeOH}F}\right] \ln \frac{\Pi a_{\text{products}}^{\upsilon_i}}{\Pi a_{\text{reactants}}^{\upsilon_i}} \qquad (1.20)$$

where R = universal gas constant

a = activity of species i

υ_i = stiochiometric coefficient of species i given by (1.1c)

One can show using (1.20) that over the temperature range in question, a change in MeOH concentration from 1 to 10M will only result in a change in open circuit potential of approximately 10mV.

Table 1.1. Thermodynamic data for $CH_3OH(l) + (3/2)O_2 \rightarrow CO_2 + 2H_2O(l)$ at STP [8].

Δg^o / kJ mol^{-1}	Δh^o / kJ mol^{-1}	Δs^o / kJ mol^{-1} K^{-1}	z	E^o / V	η_{rev}
-704	-727	-77	6	1.21	0.97

1.4 Overpotentials

The operating voltage of a DMFC is much lower than the reversible cell potential due to several irreversibilities, also referred to as losses or overpotentials. These

overpotentials can be grouped primarily into four categories: anode overpotential, cathode overpotential, ohmic overpotential, and contact overpotential.

$$V_{cell} = E - \eta_a - \eta_c - \eta_\Omega - \eta_{contact} \tag{1.21}$$

where V_{cell} = operating cell voltage

η_a = anode overpotential

η_c = cathode overpotential

η_Ω = ohmic overpotential

$\eta_{contact}$ = contact overpotential

Physically, the anode and cathode overpotentials account for the activation and the mass transport losses. The activation loss is simply the loss incurred by kinetics, i.e. the irreversible loss of energy required drive the reaction at the desired rate (current density). The mass transport loss is the loss incurred when the concentration of one or more reactant species tends to zero, and essentially starves the cell. The ohmic overpotential accounts for the resistance to flow of electrons and ions, while the contact resistance accounts for the resistance caused by non-ideal contact between two adjacent layers (e.g. the flow channel and the porous media).

Figure 1.6 gives a sketch of a typical vi (voltage–current density) curve given by Wang and Lu [5] for a DMFC. Note that for fuel cells, the current density is defined as the current per cross-sectional area of the cell; the current density is often used to quantify performance, as it allows cells of different cross-sectional areas to easily be compared. At low current densities, the shape of the vi curve is controlled primarily by activation overpotential. The qualitative nature of the activation and mass transport

overpotentials at the anode and cathode can be explained by analyzing a simplified generic form of the Tafel equation:

$$\eta = b \ln\left(\frac{i}{i_o}\frac{c_o}{c}\right) \tag{1.22}$$

where η = anode or cathode overpotential

b = generic tafel slope

i_o = a reference current density

i = operating current density

c = concentration of a reactant species

c_o = a reference concentration

The Tafel equation represents a simplified model for electrode kinetics which is sufficient in many cases. Here it is used simply to describe the generic nature of the vi curve; details of the models used for simulation will be discussed later.

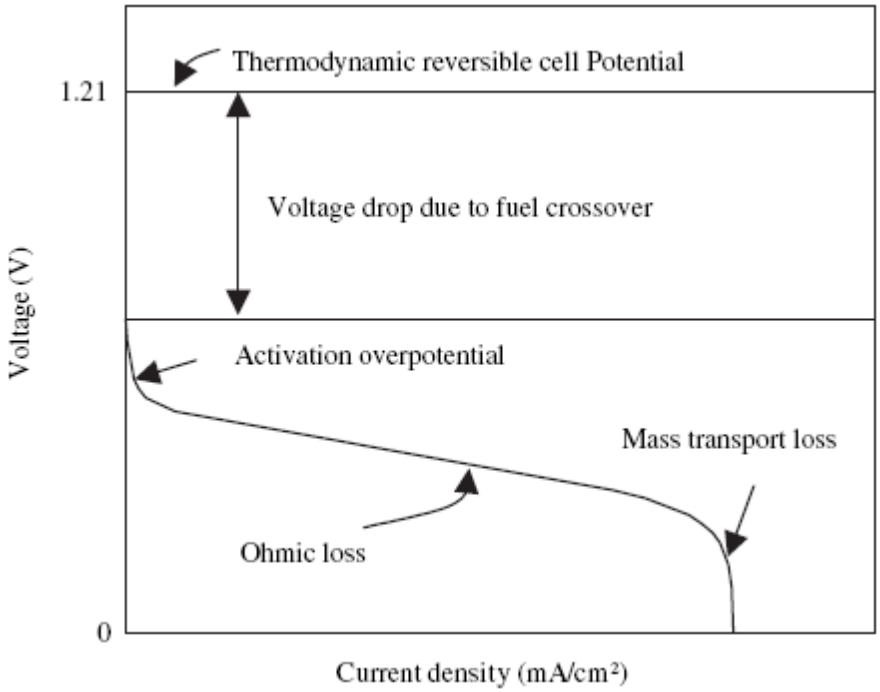

Figure 1.6. Sketch of a generic DMFC vi curve [5].

The reaction rate is directly proportional to the current density via equations (1.1). At low current densities, there is little change in the reactant concentrations, c, in the catalyst layer, and so the anode or cathode overpotential essentially have a logarithmic dependence on current density. Thus, the overpotential increases rapidly with i at low current densities; this is referred to as the activation overpotential. This behavior is reflected by the vi curve in Figure 1.6. In contrast to the activation overpotential, the ohmic overpotential is linearly related to the cell current density. This being the case, the effect of the ohmic loss on the vi curve is most prevalent at intermediate current density values. As the current density (i.e. reaction rate) increases, the reactant concentrations become reduced in the catalyst layers of the cell due to insufficient mass transport through the porous media. From equation (1.22) it is evident that as the reactant concentration tends to zero, the overpotential will go infinite. When this occurs, the cell voltage sharply goes to zero; the current density at which this occurs is referred to as the cell limiting current density, and is illustrated in Figure 1.6. The last thing to take from Figure 1.6 is the large voltage drop due to fuel crossover. The cause of this overpotential is that polymer membrane is unable to completely block the MeOH from moving from the anode side to the cathode side. When the MeOH reaches the cathode catalyst layer, it is reacted primarily electrochemically, thereby causing a significant cathode overpotential, even at open circuit. This issue will be discussed further in section 1.9 and chapter 3.

1.5 Efficiencies

The total energy efficiency of a DMFC, η, can be defined as the ratio of the useful amount of energy produced by the fuel used in the cell to the amount of heat that could be produced isothermally by the same amount of fuel in a constant-pressure combustion process (i.e. the chemical energy content of the fuel). For further insight the total energy efficiency can be broken down as

$$\eta = \eta_{rev}\eta_{volt}\eta_{fuel} \tag{1.23}$$

where η_{rev} = reversible (thermodynamic) efficiency

η_{volt} = voltaic efficiency

η_{fuel} = fuel efficiency

The thermodynamic efficiency is the upper limit of the total energy efficiency, obtainable only in an ideal cell with no irreversibilities. This efficiency can be described as the ratio of the maximum possible energy that can be produced electrochemically by the reacted fuel to the chemical energy content of the same fuel.

$$\eta_{rev} = \frac{EFz^{MeOH}\dot{n}^{MeOH}}{\Delta h_{rxn}\dot{n}^{MeOH}} = \frac{\Delta g_{rxn}}{\Delta h_{rxn}} \tag{1.24}$$

where $\dot{n}^{MeOH}$ = flow rate of all MeOH that reacts in the cell

Table 1.1 gives the thermodynamic efficiency for a DMFC as 97% under standard conditions. The voltaic efficiency can be thought of as the ratio of the energy that can be produced at the operating cell voltage by the fuel reacted to the maximum possible energy that can be produced electrochemically by the reacted fuel.

$$\eta_{volt} = \frac{V_{cell}Fz^{MeOH}\dot{n}^{MeOH}}{EFz^{MeOH}\dot{n}^{MeOH}} = \frac{V_{cell}}{E} \tag{1.25}$$

Finally, the fuel efficiency can be thought of as the actual amount of energy produced electrochemically at cell operating voltage to the energy that can be produced at the operating cell voltage by the fuel reacted.

$$\eta_{fuel} = \frac{V_{cell} I}{V_{cell}\left(I + I_x\right)} = \frac{I}{\left(I + I_x\right)} = \frac{i}{\left(i + i_x\right)} \tag{1.26}$$

where I = cell current

I_x = crossover current

i = current density (average)

One of the primary reasons for such attention for DMFC technology is the thermodynamic efficiency of 97% (in comparison, an H_2/O_2 PEFC has a thermodynamic efficiency of only 83% at STP). The voltaic and fuel efficiencies essentially amount to engineering issues. For example, improved catalyst materials, more efficiently designed catalyst layer structures, and better engineered diffusion media could all improve the voltaic efficiency. Likewise, the design of polymer membranes that are highly resistant to MeOH transport and novel MEA designs would both act to reduce the MeOH crossover, and hence increase the fuel efficiency.

1.6 Why DMFCs for Mobile Applications?

With the increasing functionality of portable electronics (e.g. smart phones with internet access, etc. replacing traditional cellular phones), there is an ever-increasing demand for a more efficient, longer-lasting power source. Due to the energy-dense, liquid nature of methanol fuel, the DMFC is a promising developing technology as a replacement for rechargeable Li-ion batteries. Dyer [16] and Pan [17], among others, present arguments for DMFCs to this extent. The main argument made by Dyer is that

the use of a DMFC will become more beneficial as the energy density demands become greater (Wh l^{-1}). Figure 1.7 shows the theoretical energy densities of several fuel cell and battery reactant combinations (note that this figure has nothing to do with the design of the cells, etc., it is simply a statement of the energy densities of the reactants themselves). It is evident from this figure that the MeOH/air combination used for DMFCs has nearly a four-fold greater energy density than the Li-ion battery materials. Figure 1.8 shows a projection of practical DMFC and Li-ion system volumes for a given energy content after battery/cell packaging is taken into account; it is assumed for both battery and DMFC that a total system conversion energy efficiency is around 25%. Another key assumption in this figure is that concentrated MeOH can be used for the DMFC; in order for this to be realized, innovative water management strategies will be required in order to supply H_2O to the anode side of the cell (see reaction 1.1a); this topic will be further discussed in section 1.9. It is evident from this projection that the potential benefits of a DMFC over a Li-ion battery increase as the energy content carried by the power source increase.

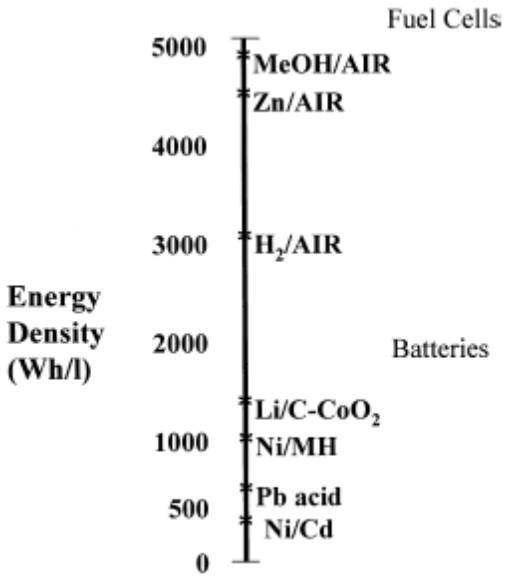

Figure 1.7. Theoretical energy densities of various fuel cell and battery reactants [16].

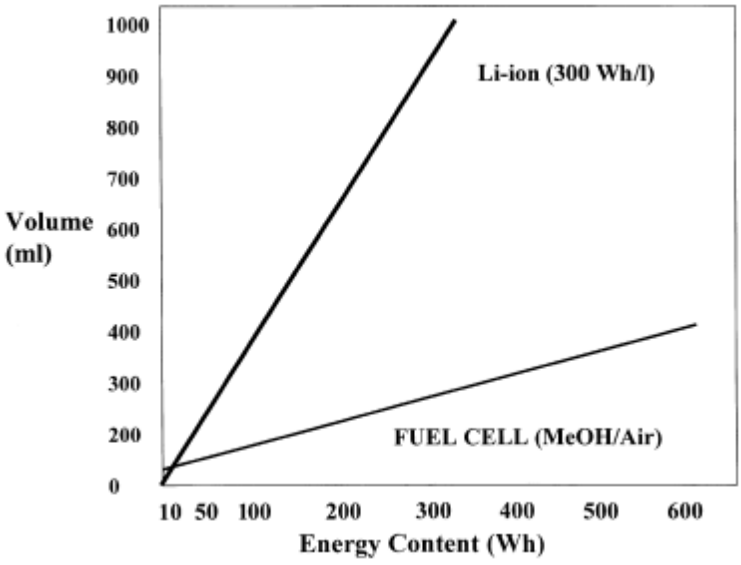

Figure 1.8. Practical system volumes for DMFC and 300Wh L^{-1} Li-ion battery [16].

From Figures 1.7 and 1.8, it becomes clear why there is great interest in DMFC technology from companies producing portable electronics. Some of the notable companies with extensive DMFC research and development efforts include Toshiba, Hitachi, Fujitsu, MTI Micro Fuel Cells [18], and Panasonic. Toshiba [19], Hitachi [19], and Panasonic [20] all have publicly presented DMFC-powered laptop prototypes. Further, just recently -- in October, 2009 -- Toshiba launched its first direct methanol fuel cell product, Dynario, which acts a mobile power source for portable electronic devices [21].

1.7 DMFC Models in the Literature

Wang [4] presents an extensive review of fuel cell models. All models reviewed, and the model presented later in this work, are termed macrohomogeneous models. Simply put, a macrohomogeneous model assumes that the domain being modeled (e.g. porous medium, membrane, etc.) can be thought of as homogeneous in a volume-

averaged sense, i.e. the material can be considered homogeneous on a scale smaller than the simulated domain. Wang [4] further notes that at this stage of research, DMFC modeling, "…aims to provide a useful tool for the basic understanding of transport and electrochemical phenomena in DMFC and for the optimization of cell design and operating conditions." In other words, at least in the short run, it is envisioned that largest benefit of DMFC modeling will be realized by providing a window into the basic physical processes occurring within a cell, and therefore facilitate new design concepts.

Oliveira et al. [22] review DFMC modeling approaches to date, and categorize the modeling types into three groups: analytical, semi-empirical, and mechanistic. The analytical models rely on many simplifying assumptions, and only characterize general cell behavior (e.g. vi curves) for simple cell designs. The benefit of the semi-empirical models is that they remain simple, and are computationally inexpensive; the down side of course is that the models are unique to specific design types, and therefore are generally incapable of being used to come up with new, innovative cell designs. The mechanistic models are based on fundamental conservation laws and electrochemical theory. For this reason, the authors [22] argue that improved mechanistic models will be required to enable better, advanced, innovative cell designs, a sentiment echoed by Wang [4] and Eikerling et al. [12]. Finally, Oliveira et al. [22] argue that one of the most important areas of research for current DMFC modeling is in the investigation of two-phase flows for anode and cathode, ideally to be performed hand-in-hand with experimental two-phase flow visualization. The understanding and modeling of two-phase flow in DMFCs are critical factors in being able to properly capture the water transport characteristics of cells.

There are many 1D models for DMFCS in the literature, with varying degrees of complexity. The models presented in Scott et al. [23,24,25], Cruickshank et al. [26], Sundmacher et al. [27,28], Argyropoulos et al. [29], and Dohle et al. [30] are all based on assumptions that greatly simplify the species transport in a DMFC (e.g. using a simple algebraic resistance-type equation to approximate the MeOH concentration in the catalyst layer). The main goal of these models seems to be to approximate general cell behavior, such as reproducing a vi curve. The models given by Kulikovsky [31,32] Meyers and Newman [33,34,35], Schultz and Sundmacher [36] , Dohle [37], and Garcia et al. [38] use transport equations to model species concentrations in the cell, but with rather significant simplifying assumptions; in particular, these models essentially neglect the effects of two-phase flow, and at least in the case of Kulikovsky [31,32], Meyers and Newman [33,34,35], Schultz and Sundmacher [36], and Garcia et al. [38] do not rigorously account for the presence of anode CO_2 gas. The models of Murgia, Shukla, et al. [39,40] have the most advanced species transport models for all of the 1D models surveyed. While these models attempt to take into account the effects of liquid saturation on the gas-phase effective diffusivity, they fail to rigorously account for capillary effects and liquid flow.

Wang and Wang [41], and Liu and Wang [42,43] developed advanced 3D, two-phase, steady-state models for force feed DMFCs. In their paper, Wang and Wang [41] used their model to study the details of MeOH crossover. One of the key findings in the paper is that the gas-phase transport of MeOH in the anode plays a significant role in delivering MeOH to the CL due to the high gas-phase diffusivity. In their first paper, Liu and Wang [42] use their model to reveal more details of the physics behind MeOH

crossover, and found that the MeOH crossover rate is spatially distributed over the cell cross-sectional area. Specifically the authors [42] found that the MeOH crossover rate was higher under the channel than under the land, due to more effective MeOH transport and corresponding higher MeOH concentration in the anode catalyst layer under the channel than under the land. In their second paper, Liu and Wang [43] implemented an interfacial liquid coverage model at the cathode BL/flow channel interface, and found that its implementation has a significant effect on the prediction of α.

1.8 Technical Challenges for DMFCs

Wang and Lu [5] outline four key technical challenges that must be addressed in order for DMFC technology to increase its practical energy density and compete with Li-ion batteries: (1) low rate of MeOH oxidation kinetics on the anode side, (2) MeOH crossover through the polymer membrane (i.e. fuel management), (3) water management, and (4) heat management. The authors note that the MeOH crossover, caused primarily by electro-osmotic drag (EOD) and diffusion, and low rate anode MOR kinetics are the prime reasons that the power density (power per cross-sectional *area* of the cell) of DMFCs are three to four times lower than that of an H_2/O_2 PEFC. In order reduce the losses incurred by the MOR, and thereby increase the cell power density, more active catalysts need to be discovered. Approaches to reduce MeOH crossover have typically included the development of novel membranes and "upstream MCO mitigation", whereby the DMFC system is designed to reduce MeOH concentration before its entrance into the diffusion media; an additional burgeoning area of research for reducing MeOH crossover is the development of advanced MEA designs. Water management

deals with the removal of water from the cathode in order to avoid flooding, while simultaneously trying to decrease the water flow through the membrane from anode to cathode (i.e. decrease α) in order to facilitate the use of high concentration MeOH. The use of highly concentrated MeOH for DMFCs is highly desirable from an energy density standpoint. The authors argue that the best way to achieve this "low-α" DMFC is by use of new MEA designs using MPL to tailor the water transport in the cell. Finally, for heat management, the authors note that for a given current density, heat generation in DMFCs is higher than for H_2/O_2 PEFC due to the lower DMFC energy efficiency (~20-30% for DMFC compared with ~50-60% for H_2/O_2 PEFC). The majority of the heat generated is removed via circulating liquid fuel on the anode side, and water evaporation on the cathode side.

Kamarudin et al. [6] provide a review of the current micro-DMFC technology. The authors outline the major challenges that currently need to be overcome in order to commercialize DMFCs on a wide scale. In addition to the same four major hurdles discussed by Wang and Lu [5] (MOR reaction kinetics, MeOH membrane crossover, water management, and thermal management), the authors also discuss the need to investigate the ageing mechanisms of DMFCs. They claim that while it is known that operating conditions such as fuel flow rate and operating temperature have an impact on the cell lifetime, a complete understanding of ageing mechanisms have yet to be fully determined.

Because they are especially relevant to the work done here, in the next section, we give a detailed review of fuel management, water management, and membrane design.

1.9 Fuel Management, H_2O Management, and Membrane Design

As touched on previously, the practical energy density of DMFC systems (Wh l^{-1}) suffer greatly when there is an inability to directly and efficiently use highly concentrated MeOH fuel. If highly concentrated fuel is used with traditionally-designed MEAs, the end result is an extremely low fuel efficiency and performance (e.g. low cell voltage at operating current) due to a high rate of MeOH crossover to the cathode. Further, because H_2O reacts on a 1:1 molar ratio with CH_3OH in the anode catalyst layer (see equation 1.1a), if highly concentrated fuel is to be carried in the system fuel tank, one must first ensure that he or she supplies a sufficient amount of H_2O to the anode catalyst layer for the MOR. Noting from equations (1.1) that three moles of H_2O are produced in the cathode for every one mole of H_2O reacted in the anode catalyst layer, ensuring a sufficient source of H_2O in the anode catalyst layer is traditionally achieved by recovering H_2O from the cathode waste stream with external equipment (external water management), and reintroducing the H_2O at some location on the anode side between the fuel tank and the MEA (e.g. a mixing chamber). However, the additional equipment is somewhat self-defeating, in that it adds to the system volume and weight (not to mention cost), thereby reducing the system energy density. Our approach taken in this work -- a burgeoning area of research -- is to internally manage the fuel and water through proper MEA design, in effort to eliminate external water recovery devices, thereby increasing the system energy density. It goes without saying that because the goal of fuel and water management is to reduce the MeOH and H_2O crossover through the membrane, the membrane design is intrinsically tied to fuel and water management.

Ideally, CH_3OH flows in the anode flow channel and moves through the anode diffusion media into the anode catalyst layer, where it reacts via the MOR (1.1a). As mentioned previously, however, some methanol crosses through the membrane into the cathode catalyst layer, where it reacts with O_2. This crossed over methanol has two detrimental effects: (1) it increases the cathode overpotential due to mixed-potential effect in the cathode catalyst layer [44,45], thereby reducing the cell voltage, and (2) it reduces the fuel efficiency (methanol is reacted without producing electrical current). The fraction of the total CH_3OH reacted which is essentially wasted by crossing into the cathode is given by the MCO, equation (1.4). As noted later in equation (4.3), MCO is another way to describe the fuel efficiency. At a typical operating current of a DMFC, MCO is typically in the range of 0.1 to 0.3 (corresponding to the fuel efficiency of 90-70%) for a relatively well-designed cell, and becomes higher at lower current densities.

Methanol is transported across the membrane from anode to cathode primarily by two mechanisms: electro-osmotic drag (EOD), and molecular diffusion. Because methanol transport to the cathode increases with methanol concentration for both of these mechanisms, in most traditional DMFC designs, the circulation of low concentration MeOH fuel in the anode flow channel is required to operate the cell at reasonable voltage and efficiency. This, of course, lowers the energy density of the system, as it effectively means that we are carrying extra liquid water in the fuel tank or system. Currently there is significant research ongoing in effort to mitigate the methanol crossover in DMFCs, thereby facilitating the use of high concentration methanol fuel. Two conventional approaches for accomplishing this task are altering the membrane [46,47] and altering the anode fuel delivery system [48,49,50,51,52,53,54].

A membrane's selectivity, the ratio of its proton conductivity to methanol permeability, has been a widely used figure-of-merit when developing and evaluating different membranes for DMFCs. Unfortunately membranes with reduced methanol permeability typically also have lower proton conductivity, and it has been exceedingly difficult to maximize this figure-of-merit. Neburchilov *et al.* [46] give a comprehensive review of membranes designed for DMFCs, and categorize the membranes into four groups: Nafion® membranes, non-Nafion® fluorinated membranes (e.g. Dow XUS®, Asahi Glass Flemion®, and membranes from Gore & Associates), composite fluorinated membranes (e.g. zirconium-based and silica-based membranes), and non-fluorinated membranes (e.g. polybenzimidazole (PBI)-based membranes, and PolyFuel polycarbon membranes). Out of the extensive types of membranes reviewed, hydrocarbon (non-fluorinated) membranes and composite fluorinated membranes are expected to have the highest ratio of proton conductivity to methanol permeability, while simultaneously attaining low cost. An alternative approach to membrane methanol crossover mitigation is the design of pore-filled electrolyte membranes, as described by Yamaguchi *et al*. [47]. In this approach the pores of a porous substrate are filled with polymer electrolyte; the substrate matrix is impermeable to water and methanol, and therefore resists swelling. The polymer electrolyte in the pores can take in water, giving it sufficient proton conductivity, while the lack of electrolyte swelling due to the presence of the matrix reduces the methanol crossover. A largely overlooked factor in the DMFC membrane development is the requirement for facilitated water transport through the membrane for internal water management. Generally speaking, nearly two-decade membrane development has been futile in terms of raising the methanol concentration in DMFCs.

There have been a variety of methods developed for altering the anode fuel delivery system to reduce MCO [48,49,50,51,52,53,54]. These methods include incorporating fuel and water mixing champers, using a dual-pump system for methanol and water balance along with an MEA with low or negative water crossover as described by Wang *et al.* [49], and using a porous plate between fuel solution and membrane electrode assembly (MEA), as explained by Abdelkareem and Nakagawa [50]. In a somewhat different approach, Kim *et al.* [51] have developed fuel cartridges that utilize hydrogels; while the details are different, the basic concept of increasing the resistance to transport of methanol into the anode remains the same. Several other approaches of altering the anode fuel delivery system have also been developed, including those utilizing a graphite-based anode plate and a self-regulated passive fuel feed system, as described by Zhang *et al.* [52], and Chan *et al.* [53], respectively.

Solely focusing on methanol transport and crossover in effort to use highly concentrated methanol fuel only paints part of the picture. Recall that water reacts stoichiometrically 1:1 with methanol in the MOR, equation (1.1a), and is produced in the ORR, equation (1.1b). A point that is often overlooked is that a great deal of water is lost to the cathode side of the cell through the membrane using typical DMFC MEA designs. With the notable exception of three patents [49,54,55], techniques altering the anode fuel delivery system generally violate water balance in the anode, and thus cannot work in steady state without adding some sort of external water management to the system. A fundamental key is to address water balance in the anode by considering water crossover through the membrane from anode to cathode.

Using the net water transport coefficient, α, given in equation (1.2), we can characterize the water crossover of different MEAs. Blum *et al.* [56] proposed a water-neutral state for a DMFC where there is a back flux of one H_2O molecule for every six protons that transport across the membrane from anode to cathode, i.e. $\alpha = -1/6$. The idea, of course, is that with this water-neutral state, no excess water must be supplied to the anode side of the cell for reaction; all of the water necessary for the MOR comes from the production of the ORR on the cathode side, i.e. pure methanol fuel can theoretically be used. MEAs designed to reduce or reverse the net transport of water into the cathode are commonly referred to as "low-α MEA technology" [57], for which much of the pioneering work was performed by Wang and coworkers [57,58,59,60,61,62]; table 1.2 lists a few milestones and important experimental confirmations for low-α MEA development.

Table 1.2. Milestones in low-α MEA technology.

Reference	α	aMPL/cMPL	Membrane	i ($mA\ cm^{-2}$)	T (^oC)	c_l^{MeOH} (M)	Stoichiometry a/c @ i_{ref} ($mA\ cm^{-2}$)	Notes/Significance
C. Lim and C.Y. Wang [59]	n/a	aMPL & cMPL Both 40 wt% PTFE	Nafion® 112		60, 90	2		First published design of low-α MEA; 210 and 105 mW cm^{-2} max power @ 90^{o}C and 60^{o}C.
A. Blum *et al.* [56]	~ -0.5 - 0.7	No aMPL Similar to cMPL with PTFE	NP-PCM*			1 - 6		Low perfomance (< 12.5 mW cm^{-2}); proposed water-neutral state.
G.Q. Lu *et al* . [58]	~ 0.6	aMPL & cMPL Both 40 wt% PTFE	Nafion® 112	~ 150	60	2	2/4 @ 150	Maximum power density of ~ 55-60 mW cm^{-2}.
F. Liu *et al.* [57]	~ 0.8	aMPL & cMPL Both 40 wt% PTFE	Nafion® 112	~ 150	60	3	2/3 @ 150	First to quantatively show effect of thin membrane in low-α MEA; ~50-60mW cm^{-2} max. power; first to fully elucidate H_2O management importance for HC-MFC.
	~ 1.0	aMPL & cMPL Both 40 wt% PTFE	Nafion® 1135	~ 150	60	3	2/3 @ 150	
C.Y. Wang and F. Liu [60]	~ 0.6	aMPL & cMPL Both 40 wt% PTFE	Nafion® 112	~ 150	60	10	1.2/3 @ 150	Low α with high concentration methanol fuel.
	~ 0.0	aMPL & cMPL Both 40 wt% PTFE	Nafion® 112	~ 150	60	20	1.3/3 @ 150	
F.Q. Liu [61,62]	~ 1.2	cMPL only 40 wt% PTFE	Nafion® 112	~ 150	60	2	2/3 @ 150	First to experimentally show hydrophobic aMPL effect on α.
	~ 0.3	aMPL & cMPL Both 40 wt% PTFE	Nafion® 112	~ 150	60	2	2/3 @ 150	
K.Y. Song *et al.* [64]	~ 1.0 - 2.5	aMPL & cMPL Both 23 wt% PTFE	Nafion® 1135	~ 120	60	3	2/Air Breathing	1.0 - 2.5 variance due to different cathode BL properties; confirms cMPL effect on α; further confirms membrane thickness effect on α.
	~ 2.7	aMPL only 23 wt. % PTFE	Nafion® 1135	~ 120	60	3	2/Air Breathing	
	~ 2.7	aMPL & cMPL Both 23 wt% PTFE	Nafion® 115	~ 120	60	3	2/Air Breathing	
J.Y. Park *et al.* [65]	~ 3.5	cMPL only 23 wt. % PTFE	Nafion® 1135	~ 160	70			Confirms aMPL effect on α; max. power density of ~90mW cm^{-2}, but α ~ 2-4x greater than reported by Lu *et al.* , Liu *et al.* , and Liu with Nafion 112 and two MPLs.
	~ 1.1	aMPL & cMPL Both 23 wt% PTFE	Nafion® 1135	~ 160	70			

*NP-PCM - Nano-Porous Proton Conducting Membrane.

Lu *et al.* [58], Liu *et al.* [57], and Wang and Liu [60] illustrated quantitatively how in order to use highly concentrated methanol fuel, the water crossover to the cathode must first be reduced. For example, Liu *et al.* [57] showed that in order to use even 3 M methanol fuel, we must have a maximum of $\alpha \approx 3$; a higher value indicates that the cell will run short of water before methanol. Considering that 3 M methanol fuel is only roughly 10% methanol by volume, and that traditional DMFCs not using low-α MEAs generally have $\alpha \approx 3$, this finding is rather astonishing. Extending the species balance analysis of Liu *et al.* [57], we obtain the following equation, which gives the methanol fuel concentration required for full use of CH_3OH and H_2O carried by the DMFC system as a function of α and MCO, assuming there is no external water management:

$$c_l^{CH_3OH} = \left\{ \left(\frac{1}{c_{l,pure}^{CH_3OH}} \right) + \left(\frac{1}{c_{l,pure}^{H_2O}} \right) (1+6\alpha)(1-MCO) \right\}^{-1} \qquad (1.27)$$

where c_l^{CH3OH} = Methanol fuel concentration required for CH_3OH/H_2O balance, i.e. full use of CH_3OH and H_2O carried in the system (mol m^{-3} or M)

$c_{l,pure}^{CH3OH}$ = Concentration of pure liquid CH_3OH (mol m^{-3} or M)

$c_{l,pure}^{H2O}$ = Concentration of pure liquid H_2O (mol m^{-3} or M)

Figure 1.9 gives a visual representation of equation (1.27) for MCO = 0.0, 0.1, 0.2, 0.3, and 0.4 If an actual fuel concentration is greater than that given in figure 1.9, the cell will run short on water before it runs short on methanol. This figure clearly illustrates the point that if we want to use high concentration methanol fuel, we must first limit α to a very low level; this further shows how clearly low-α MEA technology is a critical prerequisite for designing high concentration methanol fuel cells (HC-MFCs). For example, assuming that MCO = 0, if we desire to use 10 M methanol fuel, we must be

able to design an MEA that has α as low as 0.39. Further note from figure 1.9 that because the slope of the curve is steeper as α becomes lower, as we reduce α we get a greater return on being able to increase the maximum methanol concentration, i.e. the same reduction in α becomes more effective at low α values. This simple example underscores the absolute importance of reducing the water crossover from anode to cathode for successful use of high concentration methanol fuel.

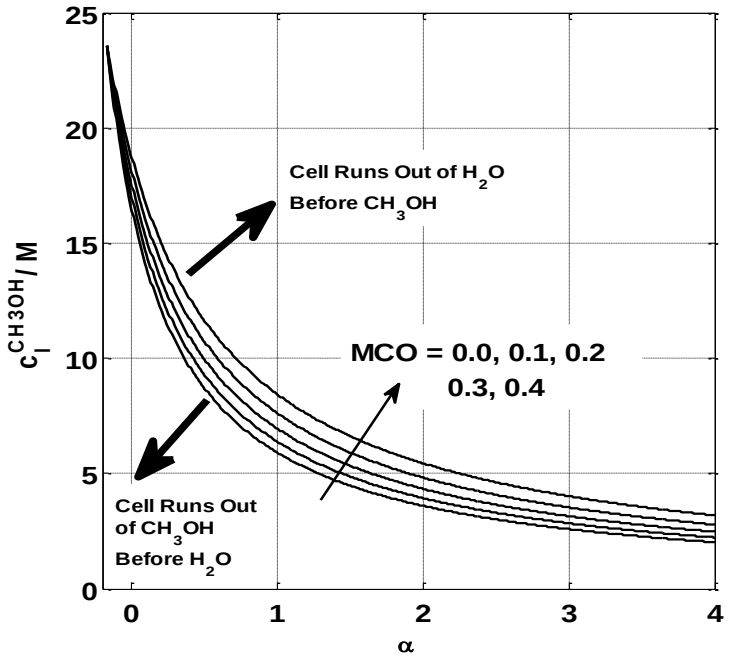

Figure 1.9. Methanol fuel concentration required for CH_3OH and H_2O balance, i.e for full use of CH_3OH and H_2O carried in system at steady-state operation; assumes no external water management; T = 60°C in this plot.

Lu *et al.* [58], Liu *et al.* [57], Wang and Liu [60,62], and Liu [61] demonstrated that by using a thin Nafion® 112 membrane along with hydrophobic micro-porous layers (MPLs), they could reduce water crossover to α ~ 0.3 - 0.8 at 60°C while still maintaining a high fuel efficiency (~ 80%), cell voltage (~ 0.4 V), and power density (~ 60 mW cm^{-2}). The hydrophobic cathode MPL/thin membrane combination in the low-α MEA was believed to be the primary reason for low water crossover, due to a buildup of liquid in

the cathode CL, and corresponding back diffusion and back-flow of water due to hydraulic permeation [5,55,63]. Liu *et al.* [57] and later Song *et al.* [64] experimentally found that a thin membrane reduces α. Liu *et al.* [57] showed that α jumped from ~ 0.8 to ~ 1.0 simply by removing a Nafion® 112 membrane and replacing it with a thicker Nafion® 1135 membrane, and Song *et al.* [64] reported α values of ~ 1.0 and ~ 2.7 for Nafion® 1135 and thicker Nafion® 115, respectively (see table 1.2 for more details). Several researchers have also experimentally confirmed that a hydrophobic cathode MPL acts to reduce α. For example, Song *et al.* [64] have reported α values of ~ 2.7 and ~ 1.0 - 2.5 for an MEA without and with hydrophobic cathode MPL respectively (see table 1.2 for more details).

More recently it was surprisingly discovered that the incorporation of a hydrophobic anode MPL can greatly reduce the water crossover from anode to cathode, playing even a more significant role than the hydrophobic cathode MPL [61,62]. Utilizing a Nafion® 112 membrane, Liu [61] first demonstrated experimentally that α dropped from ~ 1.2 to ~ 0.3 in his MEA by simply incorporating a hydrophobic anode MPL. Later Park *et al.* [65] confirmed the dramatic effect of the hydrophobic anode MPL, reporting α values of ~ 3.5 and 1.1 without and with hydrophobic anode MPL, respectively. The nearly four-fold larger α value reported by Park *et al.* [65] for MEAs with hydrophobic anode MPL (1.1 vs. 0.3) may be due to the fact that they used a thicker Nafion® 1135 membrane. Xu *et al.* [66] further give credence to the concept of a hydrophobic anode MPL reducing α, as the authors achieved no lower than α ~ 2.4 with a Nafion® 112-based MEA with only hydrophobic cathode MPL.

1.10 Contribution of this Work

The overall and common goal of all the work presented in this dissertation is to increase the practical energy density of direct methanol fuel cells. In chapter 4, we explain fundamentally how fuel and water management are intricately tied together. In addition to the standpoint of overall species balance, as illustrated in figure 1.9, in chapter 4, we further explain how fuel and water management are tied together in regards to MEA design, and how MEAs designed specifically for methanol crossover reduction must also attain a low rate of water crossover in order to be effective. We mentioned in the previous section that it has recently been demonstrated that the inclusion of a hydrophobic anode MPL significantly reduces water crossover. In chapter 5 we present a theoretical explanation of why a hydrophobic anode MPL is effective in reducing water crossover, and further perform case studies that indicate anode MPL properties that make a more effective anode MPL.

Chapter 6 presents a new MEA design with hydrophobic anode MPL and anode transport barrier in effort reduce methanol crossover while directly using concentrated MeOH fuel. The explanation of why this design is effective picks up on some of the fundamental principles developed in chapter 4, and we further elaborate via case studies what properties of the anode transport barrier make it more effective in reducing MeOH crossover. Finally, in chapter 7 we systematically analyze the validity of using the membrane selectivity as the traditional figure of merit for evaluating DMFC membranes. In this chapter, we further demonstrate the importance of considering water transport characteristics of the membrane, in addition to the traditionally considered proton conductivity and methanol permeability, for reasons of cell performance.

All of the work that we present in the forthcoming chapters, either directly (e.g. proposed MEA design with anode transport barrier) or indirectly (e.g. fundamental explanation of fuel and water management coupling within an MEA) enhances our knowledge of advanced MEA designs for the more efficient and direct use of highly concentrated methanol fuel. Naturally, this work contributes significantly to the overall goal of increasing the practical energy density of DMFCs.

Chapter 2. Background on Membrane Transport and Liquid Transport in Porous Media

Before jumping directly to an in depth description of our model, it is first pertinent to discuss, in general terms, mechanisms of fuel and water transport in the membrane, and liquid flow in porous media brought on by capillary action. These two items are discussed here because a reader with general knowledge in the thermal fluid sciences may not be overly familiar with these two topics, which are vitally important in the findings presented later.

2.1 Membrane MeOH and H_2O transport

The net water flux across the membrane can be broken into three parts: electro-osmotic drag (EOD), diffusion, and hydraulic permeation (HP):

$$N_{Mem}^{H_2O} = N_{Mem,EOD}^{H_2O} + N_{Mem,diff}^{H_2O} + N_{Mem,HP}^{H_2O} = \alpha \frac{i}{F} \tag{2.1}$$

where $N_{Mem,EOD}^{H_2O}$ = H_2O EOD membrane flux

$N_{Mem,diff}^{H_2O}$ = H_2O diffusion membrane flux

$N_{Mem,HP}^{H_2O}$ = H_2O hydraulic permeation membrane flux

Physically, EOD occurs as H_2O gets dragged along with H^+ ions as they move across the membrane. The number of H_2O molecules per H^+ ion that get dragged across the membrane varies based on how well hydrated the ionomer is, the type of ionomer material, and the temperature, and is characterized by the EOD coefficient:

$$N_{Mem,EOD}^{H_2O} = n_d^{H_2O}\left(\frac{i}{F}\right) \tag{2.2}$$

where $n_d^{H_2O}$ = H_2O electro-osmotic drag coefficient (mol H_2O/mol H^+)

The H_2O EOD coefficient for Nafion® is approximately unity when exposed to H_2O vapor [67,68], and is about 2.5-3.0 when exposed to liquid H_2O for temperatures between 30-60^oC [5,69]; the model equation used in this work is given in Appendix A, table A.5. Equation (2.2) shows that the EOD of H_2O across the membrane is always positive for any operating current density.

The diffusion of H_2O across the ionomer membrane is caused by a concentration difference of H_2O in the ionomer phase between anode and cathode. The concentration of H_2O in the ionomer phase is generally given in terms of the water content, defined by the moles of H_2O per mole of SO_3^- in the membrane, λ. For a 1D flux across the membrane

$$N_{Mem,diff}^{H_2O} = -\frac{\rho_{Mem}}{EW_{Mem}} D_{Mem}^{H_2O} \frac{d\lambda}{dx} \tag{2.3}$$

where λ = membrane water content (mol H_2O/mol SO_3^-)

EW_{Mem} = equivalent weight of membrane (kg/mol SO_3^-)

ρ_{Mem} = membrane density (kg m^{-3})

D_{Mem}^{H2O} = membrane H_2O diffusivity (m^2 s^{-1})

From (2.3) it is evident that the diffusion of H_2O across the membrane can be either positive or negative, depending on the gradient in water content. The model equation for water content as a function of liquid saturation is given in Appendix A, table A.5, along with the H_2O membrane diffusivity, which is a function of temperature.

Finally, the hydraulic permeation of H_2O across the membrane is caused by the gradient in liquid pressure:

$$N_{Mem,HP}^{H_2O} = -\frac{\rho_l K_{Mem}}{M_l \mu_l}\frac{dp_l}{dx} \tag{2.4}$$

where K_{Mem} = membrane permeability (m^2)

p_l = liquid pressure (Pa)

ρ_l = liquid density (kg m^{-3})

μ_l = liquid viscosity

The hydraulic permeation across the membrane is essentially a bulk flow across the membrane, due to a pressure differential. The physics behind liquid flow in porous media are discussed in more detail in the next section.

For MeOH, the membrane transport is driven primarily by EOD and diffusion:

$$N_{Mem}^{MeOH} = N_{Mem,EOD}^{MeOH} + N_{Mem,diff}^{MeOH} = \frac{i_x}{6F} \tag{2.5}$$

where $N_{Mem,diff}^{MeOH}$ = MeOH diffusion membrane. flux

$N_{Mem,EOD}^{MeOH}$ = MeOH EOD membrane flux

Similar to H_2O, the EOD of MeOH can also be characterized using an EOD coefficient:

$$N_{Mem,EOD}^{MeOH} = n_d^{MeOH}\left(\frac{i}{F}\right) \tag{2.6}$$

where n_d^{MeOH} = MeOH electro-osmotic drag coefficient

(mol MeOH/mol H^+)

It is known that the MeOH EOD coefficient is proportional to the MeOH concentration in the anode CL; the model equation we use in this work can once again be found in table A.5.

Similar to H_2O, the MeOH diffusion across the membrane is driven by a concentration gradient of MeOH in the membrane phase. The MeOH concentration in

the membrane phase can be characterized by the membrane MeOH content, γ^{MeOH}, which physically is the moles of MeOH per mole of SO_3^- in the membrane phase.

$$N_{Mem,diff}^{MeOH} = -\frac{\rho_{Mem}}{EW_{Mem}} D_{Mem}^{MeOH} \frac{d\gamma^{MeOH}}{dx} \tag{2.7}$$

where γ^{MeOH} = membrane methanol content (mol MeOH/mol SO_3^-)

$D_{Mem}{}^{MeOH}$ = membrane MeOH diffusivity ($m^2\ s^{-1}$)

If we integrate (2.7) over the thickness of the membrane, we obtain the following expression

$$N_{Mem,diff}^{MeOH} = \left[\frac{\rho_{Mem}}{EW_{Mem}} D_{Mem}^{MeOH}\right] \frac{\gamma^{MeOH}\big|_{aCL} - \gamma^{MeOH}\big|_{cCL}}{\delta_{Mem}} \tag{2.8}$$

Note here that $\gamma^{MeOH}\big|_{aCL}$ and $\gamma^{MeOH}\big|_{cCL}$ are the membrane phase MeOH contents at the anode and cathode catalyst layer interfaces, respectively. There is an equilibrium condition which relates the MeOH content in the membrane phase to the MeOH concentration in the adjacent porous media. For MeOH and a Nafion membrane, Gates and Newman [70], for example, have shown that this relationship is, to a very good approximation, is linear:

$$\gamma^{MeOH}\big|_{interface} = A_1 c^{MeOH}\big|_{interface} \tag{2.9}$$

Substituting (2.9) into (2.8) yields the following:

$$N_{Mem,diff}^{MeOH} = \left[\frac{\rho_{Mem} A_1}{EW_{Mem}} D_{Mem}^{MeOH}\right] \frac{c^{MeOH}\big|_{aCL} - c^{MeOH}\big|_{cCL}}{\delta_{Mem}} \tag{2.10}$$

The bracketed term in equation (2.10) is the membrane MeOH permeability, as defined in the chemical engineering literature. In order to distinguish between hydraulic permeability and permeability, which is physically a molecular diffusion process, Liu [75] referred to the bracketed term as the effective membrane diffusivity for MeOH.

$$\mathbb{P}_{Mem}^{MeOH} \equiv \mathfrak{D}_{Mem}^{MeOH} \equiv \left[\frac{\rho_{Mem} A_1}{EW_{Mem}} D_{Mem}^{MeOH} \right] \tag{2.11}$$

where $\mathbb{P}_{Mem}^{MeOH}$ = membrane methanol permeability ($m^2\ s^{-1}$)

$\mathfrak{D}_{Mem}^{MeOH}$ = effective membrane MeOH diffusivity ($m^2\ s^{-1}$)

Just like the H_2O membrane diffusivity, the permeability, or effective membrane MeOH diffusivity, is a function of temperature, as given in table A.5.

Before closing this section, we should mention why transport of H_2O by hydraulic permeability is considered, while it is not considered for MeOH. Physically, the hydraulic permeation is a bulk flow across the membrane, driven by a pressure differential across the membrane. As we will see later, at any realistic operating current density, the MeOH concentration in the anode catalyst layer must be low (< 1M) in order to mitigate methanol crossover. This means that the mole fraction of MeOH is $X_l^{MeOH} < 0.02$, and the mole fraction of H_2O is $X_l^{H2O} > 0.98$. Hence, to a very good approximation, we can ignore the MeOH transport across the membrane via hydraulic permeation, and approximate the water mole fraction coefficient to be unity ($X_l^{H2O} \sim 1$), which should technically appear in equation (2.4).

2.2 Liquid flow in porous media

Nam and Kaviany [71], and Pasaogullari and Wang [63] present the underlying theory of liquid flow in fuel cell porous media due to capillary action, and the theory developed in these papers is the basis of the liquid flow model used in this work. Characterizing the liquid flow in porous media is a critical part of DMFC modeling for several reasons. The first and most obvious reason is that water and MeOH in the liquid phase are transported by the liquid flow. Another very important reason is that the liquid

flow and saturation level in large part determine the membrane water flux. A final reason is that the liquid saturation level plays a major role in the gas- and liquid-phase effective diffusivities. All three of these points should become clearer with subsequent discussions in forthcoming chapters.

The liquid flow in porous media is driven by the liquid pressure gradient via the two-phase Darcy's law:

$$\overrightarrow{N_l} = \frac{\rho_l \overrightarrow{u_l}}{M_l} = -\frac{\rho_l K k_{rl}}{M_l \mu_l} \nabla p_l \tag{2.12}$$

where $\overrightarrow{N_l}$ = liquid-phase superficial molar flux (mol m^{-2} s^{-1})

$\overrightarrow{u_l}$ = superficial liquid velocity (m s^{-1})

M_l = molecular weight of liquid phase (g mol^{-1})

K = permeability of the porous media (m^2)

k_{rl} = relative permeability of the liquid phase

p_l = liquid pressure (Pa)

The relative permeability is due to the fact that the entire pore space is not occupied by liquid, and is a function of the liquid saturation. The dependence of the relative permeability on the liquid saturation is a hotly debated issue, but is generally assumed to depend on the third or fourth order (see, e.g. [71] or [72]) of liquid saturation:

$$k_{rl} = s^q \tag{2.13}$$

where q = order of dependence, generally assumed to be 3 or 4

Because both liquid and gas phases are present, it is convenient to define a capillary pressure, p_c, as the difference between the gas and liquid phase pressures:

$$p_c = p_g - p_l \tag{2.14}$$

In a fuel cell environment, the gas-phase pressure drop across the porous media can, to a good approximation, be neglected. Therefore, substituting (2.14) into (2.12) yields the liquid flux in terms of the capillary pressure gradient:

$$\overrightarrow{N_l} = \frac{\rho_l K k_{rl}}{M_l \mu_l} \nabla p_c \qquad (2.15)$$

Physically, the capillary pressure is determined by the curvature of the liquid/gas interface within the void space (pores) of the porous media. For hydrophobic porous media (contact angle, $\theta > 90^o$) the gas-phase is the wetting phase; for hydrophilic ($\theta < 90^o$), the wetting phase is the liquid phase. Sketches of the generic liquid/gas interfaces for hydrophobic and hydrophilic porous media are given in figure 2.1. In real porous media (see e.g. figure 1.2), the geometry of the solid phase is rather complicated, and so the curvature of the liquid/gas interface generally cannot be determined directly. However, in any real porous media, macroscopically the liquid saturation (physically, the volume fraction of the pore space occupied by the liquid phase) of the porous media can be used to approximate the average curvature, and hence the capillary pressure. Physically this can be explained in the following way. In real porous media, there is a distribution of pore sizes (void spaces). As liquid moves into hydrophobic porous media, it will first move into regions with the largest pores, where the local radius of curvature is largest, and the local capillary pressure is lowest. As more liquid moves into the hydrophobic porous layer (higher s), it must occupy smaller pores with corresponding smaller gas-liquid interface radii, and greater local capillary pressure. If the porous material can be considered macro-homogeneous, we can therefore predict the capillary pressure (volume-averaged) based on the liquid saturation (volume-averaged). For hydrophilic porous media, consider a fully saturated (s = 1) porous layer. If we force

liquid out of the layer by applying a gas pressure, the liquid will first leave the macro pores, where the curvature is largest, and local capillary pressure is smallest. To remove liquid from smaller pores (further reduce s) with greater local capillary pressure, a greater gas pressure must be applied. Once again, if the porous layer can be considered macro-homogeneous, then we can predict the capillary pressure in the porous media, based on the liquid saturation in a volume-averaged sense.

Generally, the Leverett function J(s) is used to model the relationship between capillary pressure and liquid saturation [73]:

$$p_c = \frac{\sigma cos\theta}{\left(K/\varepsilon\right)^{\frac{1}{2}}} J(s) \tag{2.16}$$

where $s = \frac{\forall_l}{\forall_{pore}}$ = liquid saturation

σ = surface tension (N m^{-1})

θ = contact angle of the porous material (degrees)

$$J(s) = \begin{cases} 1.417s - 2.120s^2 + 1.263s^3 & \theta > 90^o \\ 1.417(1-s) - 2.120(1-s)^2 + 1.263(1-s)^3 & \theta < 90^o \end{cases} \tag{2.17}$$

Equation (2.16) is an empirical constitutive relationship between the liquid saturation and the capillary pressure [73]. However, by rewriting equation (2.16) as follows, we can further physically explain this relationship.

$$p_c = \frac{2\sigma cos\theta}{\left[\frac{2\left(K/\varepsilon\right)^{\frac{1}{2}}}{J(s)}\right]} \tag{2.18}$$

In a horizontal capillary tube, where the diameter of the tube, R, is small enough such that the effects of gravity are negligible, the capillary pressure across the liquid-gas interface is given by $p_c = \frac{2\sigma cos\theta}{R}$. Note that the length scale $\left(K/\varepsilon\right)^{\frac{1}{2}}$ is proportional to,

yet typically smaller than, the pore dimension for the given porous media [73]. This being the case, the bracketed denominator in equation (2.18) can be thought of as the average pore radius for the fraction of the pores with liquid present. For example, for hydrophobic porous media, as $s \to 0$, J $\to 0$, and the bracketed term becomes extremely large. This indicates that for low s, the average pore radius of the pores occupied by liquid is large. Again for a hydrophobic porous layer, as $s \to 1$, J $\to 0.56$, its largest value, and the bracketed term goes to ~ $3.6\left(K/\varepsilon\right)^{\frac{1}{2}}$, i.e. its smallest value. This indicates that for high s, the average pore radius of the pores occupied by liquid is small. Note that this description of the capillary pressure by the empirical equation (2.18) is consistent with the physical explanation given in the previous paragraph.

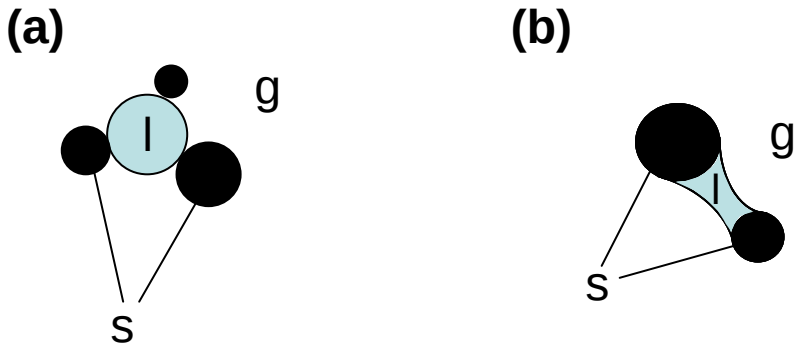

Figure 2.1. Generic depiction of liquid/gas interfaces for (a) hydrophobic, and (b) hydrophilic porous media. Here s = solid, l = liquid, g = gas.

Qualitative sketches of the liquid pressure versus liquid saturation are given in figure 2.2, using equations (2.14) and (2.16). A few things are of note here. First, for both hydrophobic and hydrophilic materials the liquid pressure decreases with decreasing liquid saturation. Therefore, in both hydrophobic and hydrophilic porous media, liquid will flow from a region with high s to a region with low s, as per equation (2.12), which is consistent with our physical description with respect to macro and micro pores.

Second, as the pore size decreases the capillary pressure increases (in magnitude) for a given value of s. Physically, this is due to the fact that the average radius of the gas-liquid interface decreases with pore size. Finally, the further the contact angle is from 90^o (larger θ for hydrophobic, smaller θ for hydrophilic), the greater the capillary pressure. Again, this can be attributed to a smaller radius of curvature at the gas-liquid interface.

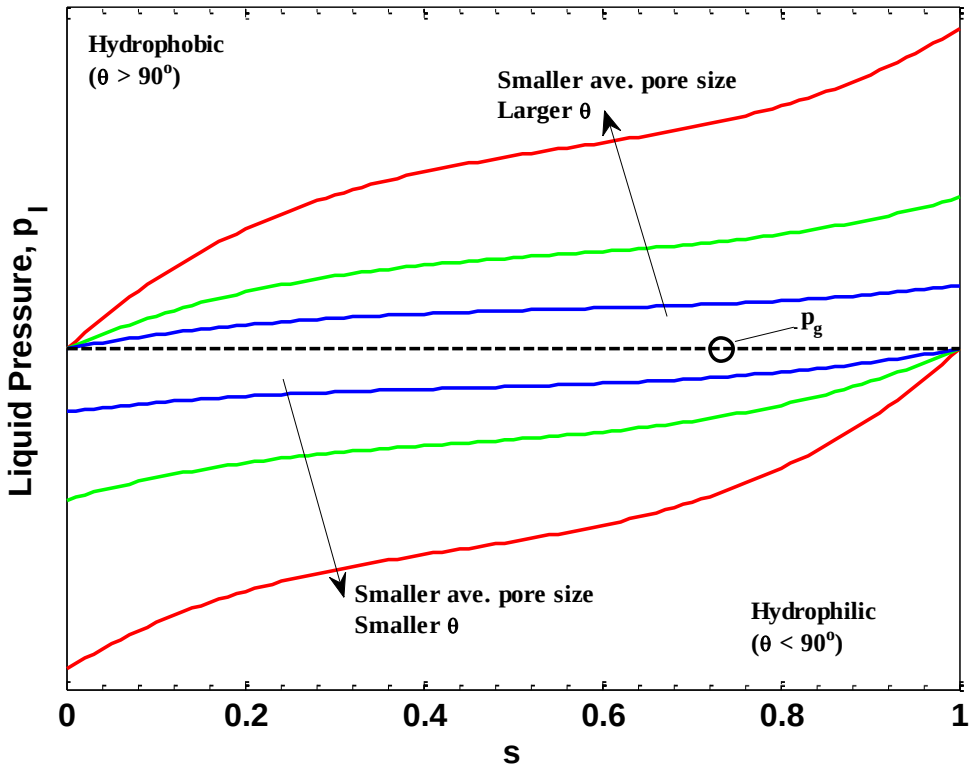

Figure 2.2. Qualitative sketches of the liquid pressure vs. s; here it is assumed that the gas-phase pressure is approximately constant.

Substituting equation (2.16) into (2.15) and assuming uniform properties leads to the following expression:

$$\overrightarrow{N_l} = \frac{\rho_l K k_{rl}}{M_l \mu_l} \frac{dp_c}{ds} \nabla s \qquad (2.19)$$

It is evident from (2.19) that as the relative permeability decreases (i.e. as s decreases), the gradient in liquid saturation must be larger in order to maintain the same liquid flux. Additionally, a larger permeability leads to a smaller liquid saturation gradient for the same flux.

Finally, at the interface between two porous layers A and B, the capillary pressure remains continuous. Pasaogullari and Wang [74] and Nam and Kaviany [71] describe that the liquid and gas phase pressures (and therefore the capillary pressure) remain continuous at the boundary between two different porous layers.

$$p_{c,A} = p_{c,B} \tag{2.20a}$$

$$\frac{\sigma cos\,\theta_A}{\left(K_A/\varepsilon_A\right)^{1/2}} J\left(s_{A,int}\right) = \frac{\sigma cos\,\theta_B}{\left(K_B/\varepsilon_B\right)^{1/2}} J\left(s_{B,int}\right) \tag{2.20b}$$

Physically, this continuous capillary pressure condition leads to a saturation jump at the interface. This can be further illustrated by looking at figure 2.2. Taking two hydrophobic curves to represent two porous layers placed together at an interface, it becomes evident that for a continuous capillary pressure from one layer to the other, there must be a saturation jump.

Chapter 3. Model

The model presented in the following sections is an extension of a 1D model previously presented by Liu [75]. Major expansions beyond the work [75] include: (1) incorporation of a saturation jump model; (2) incorporation of a cathode mixed potential electrochemistry model; (3) explicit treatment of CLs as zones of finite thickness rather than infinitely thin interfaces; (4) incorporation of an MPL model; and (5) the ability to model the transition between a single- and a two-phase region. The addition of the saturation jump model and explicit treatment of the MPLs and CLs are critically important in allowing us to explain the hydrophobic aMPL effect on water crossover, as will be discussed in the sections that follow.

3.1 Basic model setup and assumptions

Figure 3.1 gives the geometry of the 1D DMFC model used in this study, showing the distinct regions of the model: anode backing layer (aBL), anode micro-porous layer (aMPL), anode catalyst layer (aCL), membrane (Mem), cathode catalyst layer (cCL), cathode micro-porous layer (cMPL), and cathode backing layer (cBL). The model has the following assumptions:

- Steady-state
- Isothermal
- In all two-phase regions, there exists thermodynamic equilibrium between the liquid and gas phases
- Gas-phase pressure assumed uniform over the entire anode and cathode

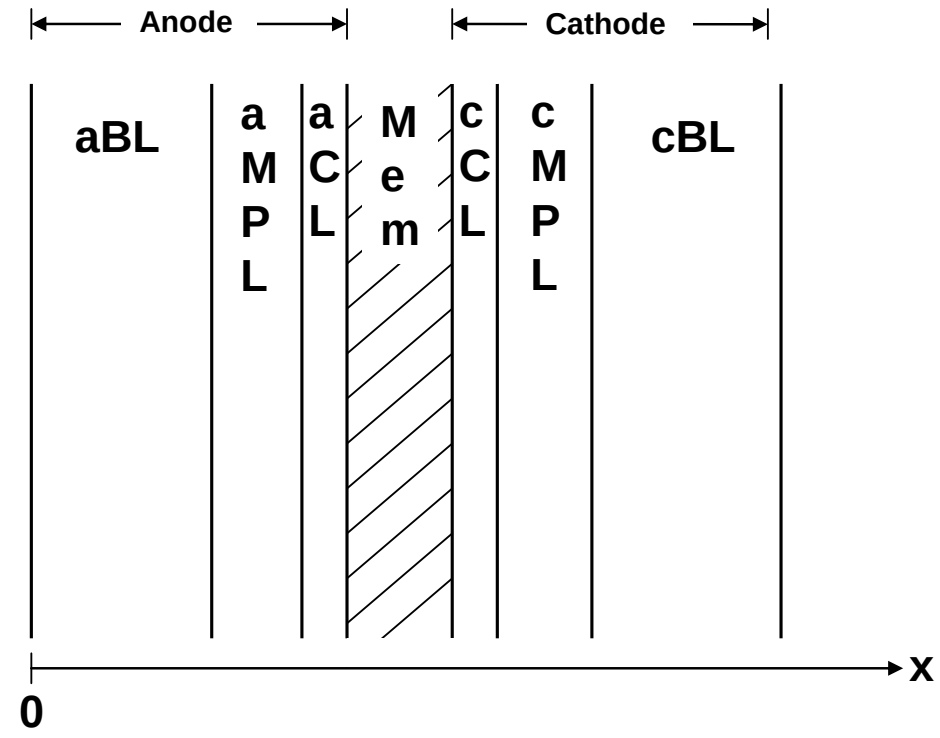

Figure 3.1. Geometry of 1D DMFC model.

3.2 Species fluxes

The anode side species transport in a DMFC generally occurs in two-phases within the porous media. The liquid phase is a binary solution of methanol and water, and the gas phase consists of methanol vapor, water vapor, and carbon dioxide gas. In these two-phase regions, the superficial flux of a given species, ψ, is equal to the sum of superficial fluxes of ψ in the liquid and gas phases:

$$N^{\psi}(x) = N_l^{\psi}(x) + N_g^{\psi}(x) \tag{3.1}$$

where N^{ψ} = superficial flux of species ψ (mol m^{-2} s^{-1}; based on physical cross-sectional area occupied by all solid, liquid, and gas phases present)

l = liquid phase

g = gas phase

In the two-phase region of the anode, there is methanol flux in both the liquid and gas phases:

$$N^{MeOH}(x) = N_l^{MeOH}(x) + N_g^{MeOH}(x) \quad \text{(two-phase region)} \tag{3.2}$$

Due to the assumptions that the cell is isothermal and that there is an equilibrium condition in all two-phase regions, we assume that there is negligible H_2O flux in the gas phase. The validity of this assumption is addressed further in Appendix C.

$$N^{H_2O}(x) = N_l^{H_2O}(x) \quad \text{(two-phase region)} \tag{3.3}$$

In a single-phase gas region, the H_2O and MeOH fluxes are, of course carried entirely in the gas phase:

$$N^{MeOH}(x) = N_g^{MeOH}(x) \quad \text{(one-phase region)} \tag{3.4}$$

$$N^{H_2O}(x) = N_g^{H_2O}(x) \quad \text{(one-phase region)} \tag{3.5}$$

Because CO_2 only exits in the gas phase, it is obvious that for any anode region

$$N^{CO_2}(x) = N_g^{CO_2}(x) \tag{3.6}$$

From a simple species conservation at steady-state conditions, the gradient of the superficial flux of species ψ can be related to the source of ψ:

$$\frac{dN^{\psi}}{dx} = -\dot{S}^{\psi'''} \tag{3.7}$$

where $\dot{S}^{\psi'''}$ = source of ψ (mol m^{-3} s^{-1})

For example, for methanol in the anode catalyst layer, it follows from equation (1.1a) that

$$\dot{S}^{MeOH'''} = -\frac{j_{anode}^{MOR}}{6F} \tag{3.8}$$

where j_{anode}^{MOR} = volumetric reaction rate of MOR in the anode CL (C m^{-3} s^{-1}), assumed positive as written in equation (1.1a)

It is assumed that the MOR rate is uniform throughout the anode catalyst layer, i.e. j_{anode}^{MOR} is constant. Applying the boundary condition that the MeOH flux is equal to the membrane MeOH flux at the membrane/CL interface, and that there is no source of MeOH outside of the CL, the following expression is obtained via integration of equation (3.7):

$$N^{MeOH}(x) = \begin{cases} N_{Mem}^{MeOH} + \dfrac{i}{6F} & (aBL, aMPL) \\ N_{Mem}^{MeOH} + \left(\dfrac{i}{6F}\right)\left(\dfrac{x_{aCL/Mem} - x}{\delta_{aCL}}\right) & (aBL, aMPL) \end{cases} \tag{3.9}$$

where δ_{aCL} = anode CL thickness

$x_{aCL/mem}$ = x location of anode CL, membrane interface

Here, the following relationship, which comes from the conservation of H^+ in the anode catalyst layer, has been utilized to relate the cell current density to the volumetric MOR reaction rate in the anode CL:

$$i = \int_{CL} j_{anode}^{MOR} dx = j_{anode}^{MOR} \delta_{aCL} \tag{3.10}$$

The H_2O and CO_2 species fluxes on the anode side are derived in the exact same manner, and are listed in table 3.1.

Table 3.1. Species fluxes for 1D DMFC model*.

Region	Species Fluxes
aBL, aMPL	$N^{MeOH}(x) = N_{Mem}^{MeOH} + \frac{i}{6F}$; $N^{H_2O}(x) = N_{Mem}^{H_2O} + \frac{i}{6F}$; $N^{CO_2}(x) = -\frac{i}{6F}$
aCL	$N^{MeOH}(x) = N_{Mem}^{MeOH} + \left(\frac{i}{6F}\right)\left(\frac{x_{aCL/Mem} - x}{\delta_{aCL}}\right)$; $N^{H_2O}(x) = N_{Mem}^{H_2O} + \left(\frac{i}{6F}\right)\left(\frac{x_{aCL/Mem} - x}{\delta_{aCL}}\right)$; $N^{CO_2}(x) = \left(-\frac{i}{6F}\right)\left(\frac{x_{aCL/Mem} - x}{\delta_{aCL}}\right)$
cCL	$N^{MeOH}(x) = \begin{cases} N_{Mem}^{MeOH} - \left[\frac{\overline{j_c^{MOR}}}{6F} + \overline{r_{chem}}\right](x - x_{Mem/cCL}) & \left(x_{cCL/Mem}^{MeOH} < x < x_o^{MeOH}\right) \\ 0 & \left(x_o^{MeOH} < x < x_{cCL/cMPL}^{MeOH}\right) \end{cases}$
	$N^{H_2O}(x) = \begin{cases} N_{Mem}^{H_2O} + \left[\frac{\overline{j_c^{ORR}}}{2F} - \frac{\overline{j_c^{MOR}}}{6F} + 2\overline{r_{chem}}\right](x - x_{Mem/cCL}) & \left(x_{cCL/Mem}^{MeOH} < x < x_o^{MeOH}\right) \\ N^{H_2O}\big\|_{x_x^{MeOH}} + \left[\frac{\overline{j_c^{ORR}} - \overline{j_c^{MOR}}}{2F}\right](x - x_o^{MeOH}) & \left(x_o^{MeOH} < x < x_{cCL/cMPL}^{MeOH}\right) \end{cases}$
	$N^{O_2}(x) = \begin{cases} -\left[\frac{\overline{j_c^{ORR}}}{4F} + 1.5\overline{r_{chem}}\right](x - x_{Mem/cCL}) & \left(x_{cCL/Mem}^{MeOH} < x < x_o^{MeOH}\right) \\ N^{O_2}\big\|_{x_x^{MeOH}} - \left[\frac{\overline{j_c^{ORR}} - \overline{j_c^{MOR}}}{4F}\right](x - x_o^{MeOH}) & \left(x_o^{MeOH} < x < x_{cCL/cMPL}^{MeOH}\right) \end{cases}$
cMPL, cBL	$N^{MeOH}(x) = 0$; $N^{H_2O}(x) = N^{H_2O}\big\|_{x=x_{cCL/cMPL}}$; $N^{O_2}(x) = N^{O_2}\big\|_{x=x_{cCL/cMPL}}$

*Note that $x < x_o^{MeOH}$ is the region of the cCL where MeOH is present, and $x > x_o^{MeOH}$ is the region where MeOH is not present.

On the cathode side of the cell, the generic superficial flux equations (3.2) and (3.3) hold for MeOH (where it is present in the cathode CL) and H_2O. The derivation of the superficial species fluxes on the cathode side are slightly more complicated due to the simultaneous occurrence of MOR, ORR, and chemical reaction, which is modeled with a detailed electrochemistry model. The final results are presented in table 3.1, but the further discussion of these terms will be given in section 3.6.

3.3 Membrane Model

To couple the anode and cathode sides of the cell, a resistance-type model is used to simulate the MeOH and H_2O diffusion across the membrane. The membrane methanol flux is given by equation (2.5); the EOD is modeled directly by using equation (2.6), and the molecular diffusion equation (2.10) can be written as follows:

$$N_{Mem,diff}^{MeOH} = \mathfrak{D}_{Mem}^{MeOH} \frac{c^{MeOH}|_{aCL} - c^{MeOH}|_{cCL}}{\delta_{Mem}} \tag{3.11}$$

where δ_{Mem} = membrane thickness

The membrane H_2O flux is given by equation (2.1); the H_2O EOD flux is modeled directly by equation (2.2), and the diffusion and hydraulic permeation terms given by equations (2.3) and (2.4) can be written as follows:

$$N_{Mem,diff}^{H_2O} = \frac{\rho_{Mem}}{EW_{Mem}} D_{Mem}^{H_2O} \frac{\lambda|_{aCL} - \lambda|_{cCL}}{\delta_{Mem}} \tag{3.12}$$

$$N_{Mem,HP}^{H_2O} = \frac{\rho_l K_{Mem}}{M_l \mu_l} \frac{p_l|_{aCL} - p_l|_{cCL}}{\delta_{Mem}} \tag{3.13}$$

As alluded to previously, in our model, the aCL and cCL are of finite thickness. Because physically water enters and exits the ionomer phase throughout the thickness of the CLs,

we approximate λ and p_l in our algebraic membrane model -- equations (3.12) and (3.13) -- as their average values in the appropriate aCL and cCL. Also, we assume that the EOD coefficients are determined by the water content and MeOH concentration conditions in the aCL (see table A.5).

3.4 Species transport

To model multi-species transport in the porous media, the Stefan-Maxwell (SM) equation can be used (see, e.g. [76]):

$$\nabla X_\beta^\psi = \sum_{h \neq \psi} \frac{X_\beta^\psi \vec{N}_\beta^h - X_\beta^h \vec{N}_\beta^\psi}{c_{t,\beta} D_{eff,\beta}^{\psi,h}} \tag{3.14}$$

where X_β^ψ = mole fraction of species ψ in the phase β

$\vec{N}_\beta^\psi$ = superficial flux of species ψ in the phase β

$D_{eff,\beta}^{\psi,h}$ = effective diffusivity of the species combination ψ, h, in phase β

Note here that the effective diffusivity accounts for the presence of the porous media and two phases [77]; when the superficial fluxes are used, they must be used in conjunction with the effective diffusivity. In this study, the effective diffusivity is calculated using the classic Bruggeman correlation to account for the tortuosity of the porous media:

$$D_{eff,g}^{\psi,h} = \left[\varepsilon(1-s)\right]^n D_g^{\psi,h} \tag{3.15a}$$

$$D_{eff,l}^{\psi,h} = \left[\varepsilon s\right]^n D_l^{\psi,h} \tag{3.15b}$$

where ε = porosity

$D_\beta^{\psi,h}$ = molecular diffusivity of components ψ and h in phase β

n = exponent for correlation; generally n ~ 1.5-3.0, in this work we assume 2.1

The exact nature of the diffusivity $D_{\beta}^{\psi,h}$ depends on the conditions for which the transport takes place.

On the anode side of the cell where two-phase conditions prevail, the liquid phase is a binary mixture consisting of methanol and water. Applying the SM equation (3.14) to this 1D case for MeOH leads to

$$\frac{dX_l^{MeOH}}{dx} = \frac{X_l^{MeOH} N_l^{H_2O} - X_l^{H_2O} N_l^{MeOH}}{c_{t,l} D_{eff,l}^{MeoH,H_2O}} \tag{3.16}$$

Because the liquid phase is a binary solution of MeOH and H_2O, the diffusivity used is simply the liquid binary diffusivity between MeOH and H_2O. Assuming an ideal solution, the following relationship between total liquid concentration and liquid MeOH concentration can be derived:

$$c_{t,l} = c_l^{MeOH} + \frac{\rho_{pure}^{H_2O}}{M^{H_2O}}\left(1 - \frac{c_l^{MeOH} M^{MeOH}}{\rho_{pure}^{MeOH}}\right) \tag{3.17}$$

where $c_{t,l}$ = total liquid molar concentration (mol/m^3)

c_l^{MeOH} = liquid MeOH molar concentration (mol/m^3)

ρ_{pure}^{i} = density of pure species i in the liquid phase (g/m^3)

M^{i} = molecular weight of species i (g/mol)

Figure 3.2 displays methanol and water concentrations versus methanol concentration for ideal and actual solutions. The mole fraction is related to the liquid concentration by

$$X_l^{MeOH} = \frac{c_l^{MeOH}}{c_{t,l}} \tag{3.18}$$

Using figure 3.2, it can be shown that up to about 10M MeOH concentration, the derivative of (3.18) can be sufficiently approximated as

$$\frac{dX_l^{MeOH}}{dx} \approx \frac{1}{c_{t,l}} \frac{dc_l^{MeOH}}{dx} \tag{3.19}$$

The validity of this approximation is further addressed in Appendix C. Substituting (3.18) and (3.19) into (3.16) yields the following relationship:

$$\frac{dc_l^{MeOH}}{dx} = \frac{c_l^{MeOH} N_l^{H_2O} - \left(c_{t,l} - c_l^{MeOH}\right) N_l^{MeOH}}{c_{t,l} D_{eff,l}^{MeoH,H_2O}} \tag{3.20}$$

In this simplification, the liquid phase concentration relationship $c_{t,l} = c_l^{MeOH} + c_l^{H_2O}$ has been used. Equation (3.20) can be rewritten for the liquid MeOH flux:

$$N_l^{MeOH} = \frac{c_l^{MeOH} N^{H_2O} - c_{t,l} D_{eff,l}^{MeoH,H_2O} \dfrac{dc_l^{MeOH}}{dx}}{\left(c_{t,l} - c_l^{MeOH}\right)} \tag{3.21}$$

Note here that equation (3.3) has been used to change the nomenclature for H_2O flux.

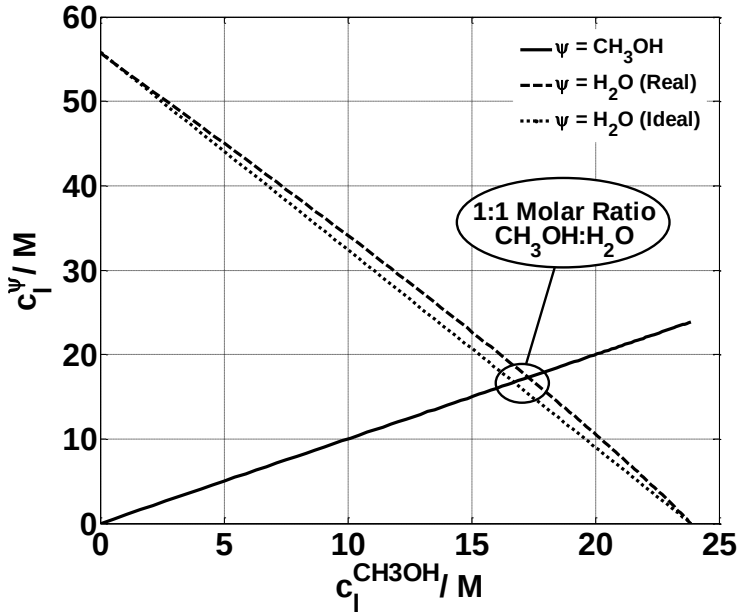

Figure 3.2. Liquid methanol and water concentrations for ideal and real binary liquid solution. Real solution data adopted from [78]; T = 25°C in this plot.

In the vapor-phase, MeOH, H_2O and CO_2 are all present, and equation (3.14) can be used for MeOH as

$$\frac{dX_g^{MeOH}}{dx} = \frac{X_g^{MeOH} N_g^{H_2O} - X_g^{H_2O} N_g^{MeOH}}{c_{t,g} D_{eff,g}^{MeOH,H_2O}} + \frac{X_g^{MeOH} N_g^{CO_2} - X_g^{CO_2} N_g^{MeOH}}{c_{t,g} D_{eff,g}^{MeOH,CO_2}} \tag{3.22}$$

In the fuel cell environment, the pressure remains close enough to ambient to treat all gases and vapors as ideal (i.e. the operating pressure remains far below the critical point pressures of all species present). This being the case, the binary diffusivity values can be used for the gas phase species. Using the relationship $X_g^i = c_g^i / c_{t,g}$ and the fact that for a constant temperature and pressure $c_{t,g}$ remains constant, equation (3.22) can be re-written in terms of the MeOH gas-phase molar concentration:

$$\frac{dc_g^{MeOH}}{dx} = \frac{c_g^{MeOH} N_g^{H_2O} - c_g^{H_2O} N_g^{MeOH}}{c_{t,g} D_{eff,g}^{MeOH,H_2O}} + \frac{c_g^{MeOH} N_g^{CO_2} - c_g^{CO_2} N_g^{MeOH}}{c_{t,g} D_{eff,g}^{MeOH,CO_2}} \tag{3.23}$$

A form of Henry's law suitable for this application which relates the equilibrium gas and liquid phase concentrations of MeOH, is given by

$$k_H = \frac{c_l^{MeOH}}{c_g^{MeOH}} \tag{3.24}$$

The Henry constant, k_H, can be calculated via the following Arrhenius-type relationship:

$$k_H = k_H^o RT e^{\left[-\frac{\Delta_{soln}H}{R}\left(\frac{1}{T}-\frac{1}{T_{ref}}\right)\right]} \tag{3.25}$$

where R = universal gas constant = 8.314 J mol^{-1} K^{-1}

T_{ref} = 298.15 K = reference temperature

$\Delta_{soln}H$ = -35,000 J mol^{-1}

k_H^o = 1.5791 mol J^{-1}

Figure 3.3 compares c_g^{MeOH} as predicted by equations (3.24) and (3.25) with experimental data given by McGlashan, et al. [78]. This figure shows that using (3.25) to relate the gas and liquid phase methanol concentrations yields no appreciable error until we reach $c_l^{MeOH} > 20$ M. Further, because we have a two-species liquid solution in the DMFC anode (CH_3OH and H_2O), the gas-phase saturated H_2O concentration is also a function of the liquid-phase CH_3OH concentration, c_l^{MeOH}. Physically, this is because the gas-phase H_2O equilibrium concentration (saturated concentration) depends on the concentration of the CH_3OH/H_2O liquid mixture, just as the gas-phase equilibrium CH_3OH concentration does. In this work we simply use an empirical correlation $c_g^{MeOH} = f(c_l^{MeOH}, T)$, given by equation (3.26), which we fit to the data given by McGlashan, et al. [78]; a plot of this correlation is given in figure 3.4.

$$c_{sat}^{H_2O} = a_4\left(c_l^{MeOH}\right)^4 + a_3\left(c_l^{MeOH}\right)^3 + a_2\left(c_l^{MeOH}\right)^2 + a_0 \tag{3.26}$$

where c_l^{MeOH} has units of M

Here, the a_4, a_3, etc. coefficients are a function of temperature:

$$a_4 = b_{42}T^2 + b_{41}T + b_{40} \tag{3.27}$$

$b_{42} = -3.320\text{x}10^{-8}$

$b_{41} = 1.941\text{x}10^{-5}$

$b_{40} = -2.842\ \text{x}10^{-3}$

$$a_3 = b_{32}T^2 + b_{31}T + b_{30} \tag{3.28}$$

$b_{32} = 1.060\text{x}10^{-6}$

$b_{31} = -6.105\ \text{x}10^{-4}$

$b_{30} = 8.791\ \text{x}10^{-2}$

$$a_2 = b_{22}T^2 + b_{21}T + b_{20} \tag{3.29}$$

$b_{22} = -1.194 \times 10^{-5}$

$b_{21} = 6.739 \times 10^{-3}$

$b_{20} = -9.493 \times 10^{-1}$

$$a_0 = c_{sat,pure}^{H_2O}(T) \tag{3.30}$$

where $c^{H2O}_{sat,pure}$ = saturated water concentration for pure H_2O liquid

As mentioned previously, the gas-phase H_2O flux is assumed to be negligible. Eliminating the $N_g^{H_2O}$ term in (3.22), substituting in (3.24), and rearranging for N_g^{MeOH} yields the following:

$$N_g^{MeOH} = \frac{c_l^{MeOH} N^{CO_2} - c_{t,g} D_{g,eff}^{MeOH,CO_2} \dfrac{dc_l^{MeOH}}{dx}}{k_H \left[c_{sat}^{H_2O} \left(\dfrac{D_g^{MeOH,CO_2}}{D_g^{MeOH,H_2O}} \right) + c_g^{CO_2} \right]} \tag{3.31}$$

Note here that the equilibrium gas-phase H_2O molar concentration has been explicitly inserted into the equation for $c_g^{H_2O}$, and that equation (3.6) has been used to change the CO_2 flux nomenclature. Also, the "effective" part of the diffusivities has been dropped in the ratio of diffusivities in the denominator: as per equation (3.15a), the "effective" part of the diffusivities cancel, yielding the ratio of the binary diffusivities.

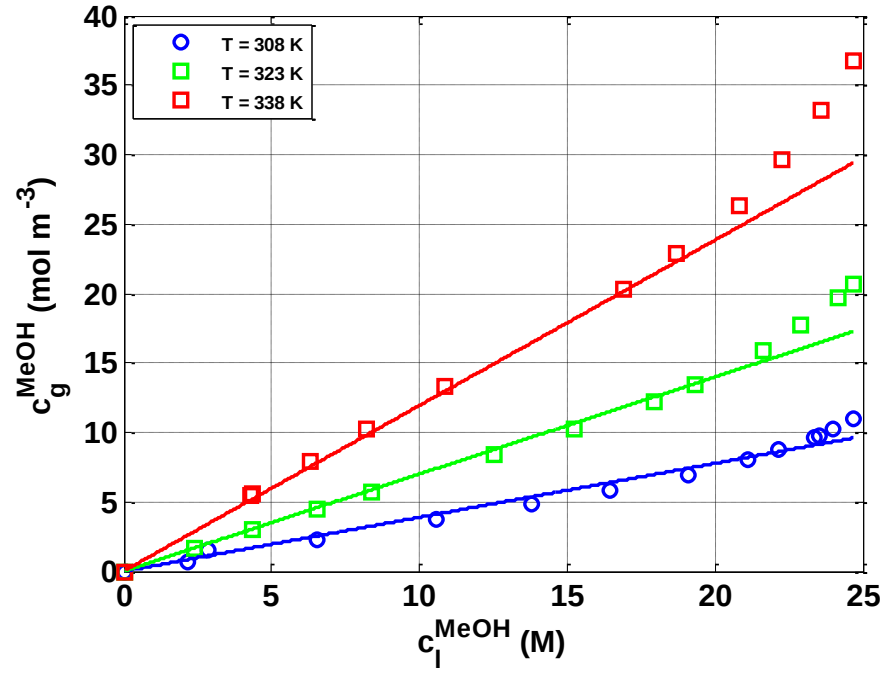

Figure 3.3. Equilibrium c_g^{MeOH} vs. c_l^{MeOH} relationship, as given by equations (3.24) and (3.25) (solid lines) and experimental data (symbols) [78].

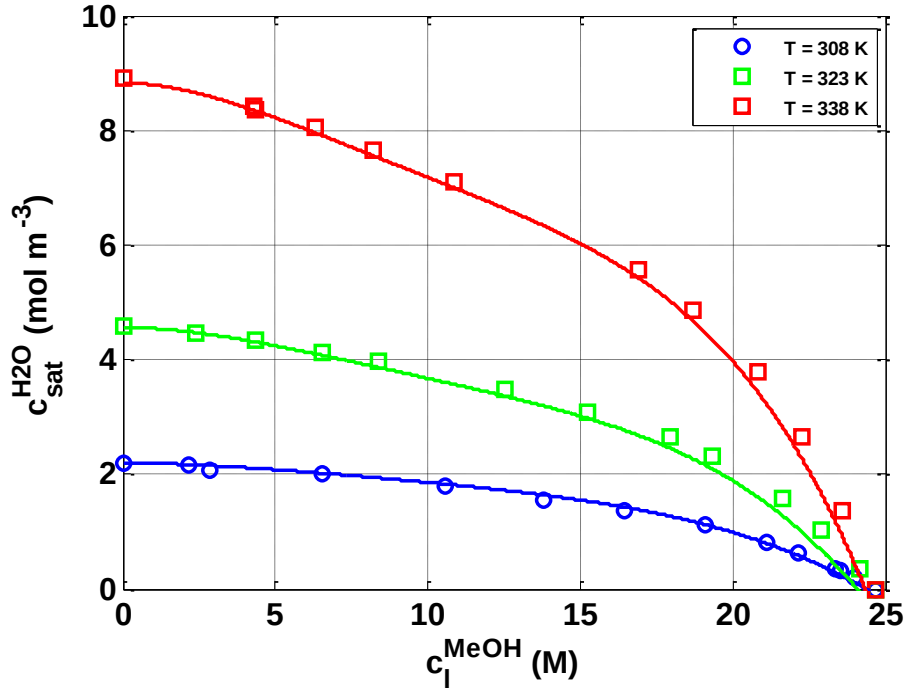

Figure 3.4. Equilibrium c_{sat}^{H2O} vs. c_l^{MeOH} relationship, as given by equation (3.26) (solid lines) and experimental data (symbols) [78].

Inserting equations (3.21) and (3.31) into (3.2) yields an expression for the total flux of MeOH:

$$\frac{c_l^{MeOH} N^{H_2O} - c_{t,l} D_{eff,l}^{MeoH,H_2O} \frac{dc_l^{MeOH}}{dx}}{\left(c_{t,l} - c_l^{MeOH}\right)} + \frac{c_l^{MeOH} N^{CO_2} - c_{t,g} D_{g,eff}^{MeOH,CO_2} \frac{dc_l^{MeOH}}{dx}}{k_H \left[c_{sat}^{H_2O} \left(\frac{D_g^{MeOH,CO_2}}{D_g^{MeOH,H_2O}} \right) + c_g^{CO_2} \right]} = N^{MeOH}(x) \qquad (3.32)$$

The total MeOH flux on the right-hand side is known for the given current density via the equation given in table 3.1, and the total H_2O and CO_2 fluxes on the left-hand side are likewise given in table 3.1. In the two-phase region of the anode, equation (3.32) is solved for the liquid MeOH concentration. The corresponding total liquid and gas-phase MeOH concentrations are calculated via equations (3.17) and (3.24), respectively. The gas-phase H_2O concentration is determined by equation (3.26). The total gas-phase concentration is known from the ideal gas law:

$$c_{t,g} = \frac{p_g}{RT} \qquad (3.33)$$

where p_g = gas-phase pressure

R = universal gas constant

T = temperature

Finally, the CO_2 gas concentration is calculated by

$$c_g^{CO_2} = c_{t,g} - c_g^{H_2O} - c_g^{MeOH} \qquad (3.34)$$

where $c_g^{H_2O} = c_{sat}^{H_2O}$ in the two-phase region

If there is a single-phase region present on the anode side of the cell, equation (3.22) holds, but we can no longer approximate $N_g^{H_2O}$ as negligible; the entire H_2O species flux must occur in the gas phase, as given by equation (3.5). Inserting (3.4),

(3.5), and (3.6) into (3.22) and rearranging for N^{MeOH}, the following expression is derived:

$$\frac{c_g^{MeOH} N^{CO_2} + \left(\frac{D_g^{MeOH,CO_2}}{D_g^{MeOH,H_2O}} \right) c_g^{MeOH} N^{H_2O} - c_{t,g} D_{g,eff}^{MeOH,CO_2} \frac{dc_g^{MeOH}}{dx}}{c_g^{H_2O} \left(\frac{D_g^{MeOH,CO_2}}{D_g^{MeOH,H_2O}} \right) + c_g^{CO_2}} = N^{MeOH}(x) \tag{3.35}$$

The total MeOH flux on the right-hand is still given by the expression in table 3.1 for a given current density, and the total H_2O and CO_2 fluxes on the left-hand side are also given in table 3.1. Equation (3.35) is solved in a single-phase region on the anode side for c_g^{MeOH}. Because the gas-phase H_2O concentration is unknown in the single-phase anode region, a SM transport equation must be used to solve for $c_g^{H_2O}$. The same approach as for equation (3.35) is used, and the resulting equation is given by

$$\frac{c_g^{H_2O} \left[N^{CO_2} + \left(\frac{D_g^{H_2O,CO_2}}{D_g^{H_2O,MeOH}} \right) N^{MeOH} \right] - c_{t,g} D_{g,eff}^{H_2O,CO_2} \frac{dc_g^{H_2O}}{dx}}{c_g^{MeOH} \left(\frac{D_g^{H_2O,CO_2}}{D_g^{H_2O,MeOH}} \right) + c_g^{CO_2}} = N^{H_2O}(x) \tag{3.36}$$

The fluxes here are once again given in table 3.1, and equation (3.36) is solved in the single-phase region in the anode for $c_g^{H_2O}$. With c_g^{MeOH} and $c_g^{H_2O}$ known, $c_g^{CO_2}$ is then determined via equation (3.34).

On the cathode side of the cell, two-phase conditions are present, and the H_2O gas-phase concentration is assumed to be at its saturated value. For the O_2 transport on the cathode side, we use Fick's Law:

$$-D_{g,eff}^{O_2} \frac{dc_g^{O_2}}{dx} = N^{O_2}(x) \tag{3.37}$$

Note that Wang and Wang [79] showed that in the cathode, the Peclet number is less than ~ 0.1, meaning that the convective transport in the gas phase is small compared to the diffusion transport. Thus, to a good approximation, the total flux of O_2 can be equated to the diffusion flux. Further, as described by references [80] and [76], even though we have multi-component diffusion on the cathode side (primarily O_2, N_2, and H_2O), because we are dealing with ideal gases, and because $D_g^{O2,N2} \sim D_g^{O2,H2O} \sim D_g^{H2O,N2}$, to a good approximation, we can use Fick's Law to model the O_2 diffusion.

Due to the methanol cross-over from the anode side of the cell, the methanol transport must be solved in the cathode catalyst layer. Equation (3.21), derived for the anode side liquid-phase MeOH flux, can also directly be used in the cathode catalyst layer, where MeOH and H_2O are simultaneously present. Noting the MeOH is only present in trace amounts in the cathode catalyst layer, like the O_2 transport, using Fick's Law, the gas-phase MeOH flux can be written as

$$-D_{g,eff}^{MeOH} \frac{dc_g^{MeOH}}{dx} = N_g^{MeOH} \tag{3.38}$$

Summing the gas and liquid fluxes (3.21) and (3.38) via equation (3.2) for the two-phase cathode catalyst layer, the following equation is obtained:

$$\frac{c_l^{MeOH} N^{H_2O} - c_{t,l} D_{l,eff}^{MeOH,H_2O} \frac{dc_l^{MeOH}}{dx}}{c_{t,l} - c_l^{MeOH}} - D_{g,eff}^{MeOH} \frac{dc_g^{MeOH}}{dx} = N^{MeOH}(x) \tag{3.39}$$

Once again making use of Henry's Law (3.24), equation (3.39) can be rewritten as

$$\frac{c_l^{MeOH} N^{H_2O} - c_{t,l} D_{l,eff}^{MeOH,H_2O} \frac{dc_l^{MeOH}}{dx}}{c_{t,l} - c_l^{MeOH}} - \frac{D_{g,eff}^{MeOH}}{k_H} \frac{dc_l^{MeOH}}{dx} = N^{MeOH}(x) \tag{3.40}$$

Here, the MeOH and H_2O fluxes are those for the cathode side, as given in table 3.1. Equation (3.40) is solved in the cathode catalyst layer for liquid MeOH concentration. Just as on the anode side, after c_l^{MeOH} is calculated, c_g^{MeOH} and $c_{t,l}$ are found via equations (3.24) and (3.17) respectively.

3.5 Liquid flow

As described in the previous chapter, the liquid flow in the porous media is modeled using equation (2.19). On the anode side where both H_2O and MeOH liquid exist, the liquid phase molar flux, $\overrightarrow{N_l}$, is due to both species. In this two-phase region, the H_2O flux is assumed to be entirely in the liquid phase, as given by equation (3.3), and the liquid MeOH flux must be calculated via (3.21). This leads to the 1D form of equation (2.19) as

$$\frac{\rho_l K k_{rl}}{M_l \mu_l} \frac{dp_c}{ds} \frac{ds}{dx} = N^{H_2O}(x) + N_l^{MeOH}(x) = N_l(x) \tag{3.41}$$

Equation (3.41) is also valid on the cathode side of the cell, but as given in table 3.1, the liquid MeOH flux is zero outside of the cathode catalyst layer region with MeOH present. We solve equation (3.41) numerically for the liquid saturation in x; as described in appendix B, we first transform this equation to enhance numerical efficiency and robustness. Note that at the interface between two porous layers, the capillary pressure is continuous, and the saturation jump is calculated via equation (2.20b), as discussed in the previous chapter.

3.6 Electrochemistry model

The average cell current density is an input to our model, and the cell voltage is calculated by subtracting the anode, cathode, ohmic, and contact resistance overpotentials from the open circuit potential, as given in equation (1.21). The anode overpotential, η_a, is calculated based on tafel kinetics, as given in equation (3.42). We assume a uniform reaction rate for the methanol oxidation reaction (MOR) across the anode catalyst layer, and therefore the anode electrochemistry model is not coupled with the species transport equations in the anode catalyst layer.

$$\eta_a = \frac{RT}{\alpha_a F} \ln\left(\frac{i}{i_o^{MOR}}\right) \tag{3.42}$$

where i_o^{MOR} = superficial exchange current density for MOR (A m^{-2})

α_a = anodic charge transfer coefficient

The average superficial exchange current density in the anode catalyst layer, i_o^{MOR}, is calculated with the following expression:

$$i_o^{MOR} = \frac{\omega_a A_{m,a}}{\delta_{aCL}} \int_{aCL} \tilde{i}_{o,ref}^{MOR} \left(\frac{c^{CH_3OH}}{c_{thresh}^{CH_3OH}}\right)^n \exp\left[\left(\frac{E_{a,a}}{R}\right)\left(\frac{1}{T_{ref}^{MOR}} - \frac{1}{T}\right)\right] dx \tag{3.43}$$

where ω_a = anode catalyst loading (mg cm^{-2})

$A_{m,a}$ = mass specific reaction area (m^2 kg^{-1})

$\tilde{i}_{o,ref}^{MOR}$ = intrinsic (per reaction surface area) reference exchange current density (A m^{-2})

c_{thresh}^{MeOH} = threshold concentration for changing order of MOR kinetics (M)

$E_{a,a}$ = activation energy of MOR (J mol^{-1})

It is clear from equation (3.43) that the effects of the changing methanol concentration over the thickness of the anode catalyst layer on the MOR kinetics is accounted for in this model. Approximating the volumetric MOR current density (i.e. methanol oxidation reaction rate) across the anode catalyst layer as uniform for our species transport equations while calculating our average superficial exchange current density via (3.43) allows us to capture the effects of low methanol concentration on cell voltage, while keeping our species transport and anode electrochemistry models decoupled. The MOR has zeroth-order dependence (n = 0) on CH_3OH concentration for c^{CH3OH} greater than the threshold concentration of c^{CH3OH}_{thresh} = 0.1 M and first-order dependence (n = 1) for $c^{CH3OH} < c^{CH3OH}_{thresh}$ [81].

The ohmic overpotential is calculated by breaking it into four regions: anode catalyst layer, anode half of the membrane, cathode half of the membrane, and cathode catalyst layer. The idea behind this approach is twofold: one, by breaking the calculation up into four regions, we can more accurately capture the local moisture condition on the ionomer conductivity, and two, we can capture the effects of the effective ionic conductivity in the anode and cathode catalyst layers, due to the porous nature of the electrodes. The expression used to calculate the ohmic overpotential is given by equation (3.44):

$$\eta_{\Omega} = \left\{ \frac{\delta_{aCL}}{\kappa^{H^+}\Big|_{\lambda_{aCL}} \left[\varepsilon_{aCL}^{ion}\right]^{2.1}} \right\} \frac{i}{2} + \left\{ \frac{\delta_{Mem}/2}{\kappa^{H^+}\Big|_{\lambda_{aCL}}} \right\} i + \left\{ \frac{\delta_{Mem}/2}{\kappa^{H^+}\Big|_{\lambda_{cCL}}} \right\} i + \left\{ \frac{\delta_{cCL}}{\kappa^{H^+}\Big|_{\lambda_{cCL}} \left[\varepsilon_{cCL}^{ion}\right]^{2.1}} \right\} \frac{i}{2} \qquad (3.44)$$

where κ^{H+} = inoic conductivity (S m^{-1} or Ω^{-1} m^{-1})

It is evident from eq. (3.44) that the portions of the ohmic overpotential in the anode catalyst layer and anode half of the membrane are based on the water content calculated

from the conditions on the anode side of the membrane. Similarly, the ohmic overpotential in the cathode half of the membrane and in the cathode catalyst layer are based on the conditions on the cathode side of the membrane. A discussion of how we calculate λ_{aCL} and λ_{cCL} can be found in section 3.3. In the electrodes we assume the average current carried by the H^+ ions in the electrodes to be half of the entire current. The ionic conductivity is calculated with the following equation, which is a combination of the Sone correlation [82] for RH < 1 and the Springer correlation [83] for RH > 1.

$$\kappa^{H^+} = \kappa^{H^+}_{303K} \exp\left[1268\left(\frac{1}{303} - \frac{1}{T}\right)\right] \tag{3.45}$$

where κ^{H+}_{303K}= inoic conductivity at T = 303 K (S m^{-1} or Ω^{-1} m^{-1})

$$\kappa^{H^+}_{303K} = \begin{cases} (11.8)RH^3 - (11.6)RH^2 + (6.72)RH \; - 0.801 \; \left(S/m\right) & for\ RH < 1 \\ (0.5139)\lambda - 0.326 \qquad\qquad\qquad\qquad\quad \left(S/m\right) & for\ RH > 1 \end{cases} \tag{3.46}$$

In expressions (3.45) and (3.46) that the temperature, T, is in Kelvin and the RH is a fraction (RH = 0 - 1) rather than a percentage. It should be noted that later in chapter 7, where we show results for various ($\kappa^{H+}/\kappa^{H+}_{bl}$), we are using the same correlations (3.45) and (3.46) (and hence the same functional dependence on wetness and temperature), and simply dividing or multiplying by the given proportionality constant.

In reference to equation (1.21), the contact overpotential is calculated by

$$\eta_{cont} = iR_{cont} \tag{3.47}$$

where R_{cont} = contact resistance (Ω m^2)

In this work we assume a contact resistance, R_{cont}, of 3.0×10^{-6} Ω m^2. All other pertinent parameters and constants used in the cell voltage sub-model are listed in table 3.2.

Table 3.2. Parameters and constants used in cell voltage sub-model.

Parameter	Value
ω_a/ mg cm^{-2}	4.0
ω_c/ mg cm^{-2}	2.0
α_a	0.701 [b]
$\tilde{i}_{o,ref}^{MOR}$ / A m^{-2}	3.55x10^{-4} [b]
T_{ref}^{MOR} / K	353 [b]
$E_{a,a}$/ J mol^{-1}	60x10^{3} [b]
$A_{m,a}$/ m^2 kg^{-1}	60x10^{3}

[b]Taken or calculated from the data given in ref. [84].

Due to the crossover of methanol from anode to cathode, in the cathode catalyst layer, there are simultaneous methanol oxidation, oxygen reduction, and chemical reactions which occur. The MOR effectively leads to an additional ORR current, due to the H^+ and e^- produced; this leads to a mixed potential in the cathode catalyst layer, and ultimately a lower cell voltage. In order to model this cathode mixed potential, we implement the model developed by Liu and Wang [44].

As presented by Liu and Wang [44], the oxygen reduction kinetics in the cathode (corresponding to the ORR (1.1b)) is modeled using a tafel equation:

$$j_{cathode}^{ORR} = j_{ref}^{ORR} \frac{c_g^{O_2}}{c_{g,ref}^{O_2}} (1-s) \exp\left[\frac{\alpha_c F}{RT}\eta_c\right] \tag{3.48}$$

where $j_{cathode}^{ORR}$ = ORR volumetric current density (A m^{-3})

j_{ref}^{ORR} = reference volumetric ORR current density (A m^{-3})

$c_{g,ref}^{O_2}$ = reference O_2 gas-phase concentration (mol m^{-3})

α_c = cathodic transfer coefficient for the ORR

The MOR is assumed to follow the following multi-step reaction mechanism, initially proposed in references [85] and [45]:

$$CH_3OH \underset{k_1'}{\overset{k_1}{\rightleftharpoons}} CH_3OH_{ads} \tag{3.49a}$$

$$CH_3OH_{ads} \xrightarrow{k_2} CO_{ads} + 4H_{ads} \tag{3.49b}$$

$$H_2O \underset{k_3'}{\overset{k_3}{\rightleftharpoons}} OH_{ads} + H_{ads} \tag{3.49c}$$

$$CO_{ads} + OH_{ads} \xrightarrow{k_4} CO_2 + H_{ads} \tag{3.49d}$$

$$H_{ads} \xrightarrow{k_5} H^+ + e^- \tag{3.49e}$$

The species rate equations can be written at steady-state to obtain the following:

$$j_{cathode}^{MOR} = 6aFKk_4 \exp\left[\frac{(1-\beta_4)FV_{cath}}{RT}\right]\theta_{CO}\theta_{OH} \tag{3.50}$$

where a = specific reaction area (m^{-1}); reaction surface area divided by physical volume in the CL

θ_{CO} = surface coverage of CO_{ads} on catalyst surface

θ_{OH} = surface coverage of OH_{ads} on catalyst surface

V_{cath} = cathode potential

$$\theta_{CO} = b\frac{k_2 \exp\left[\frac{\alpha_2 FV_{cath}}{RT}\right]}{k_4 \exp\left[\frac{(1-\beta_4)FV_{cath}}{RT}\right]} \tag{3.51}$$

$$\theta_{OH} = \frac{k_1 c^{MeOH}\left(1-\theta_{CO}\right)}{b\left\{k_1' + k_2 \exp\left[\frac{\alpha_2 FV_{cath}}{RT}\right] + k_1 c^{MeOH}\right\} + k_1 c^{MeOH}} \tag{3.52}$$

$$b = \frac{k_3' \exp\left[-\frac{\beta_3 FV_{cath}}{RT}\right]}{\frac{\left\{k_1' + k_2 \exp\left[\frac{\alpha_2 FV_{cath}}{RT}\right]\right\}k_3 \exp\left[\frac{(1-\beta_3)FV_{cath}}{RT}\right]}{k_1 c^{MeOH}} + k_2 \exp\left[\frac{\alpha_2 FV_{cath}}{RT}\right]} \tag{3.53}$$

Note in equations (3.50) through (3.53) (and also in equation (3.54)), k, β, etc. are kinetic rate parameters, and their values are listed in table A.6. The key assumptions in obtaining equations (3.50) through (3.53) are that (a) H_{ads} produced by (3.49b), (3.49c) and (3.49d) is immediately oxidized by (3.49e) for $V_{cath} > 0.3V$ (which is the case under any realistic operating DMFC conditions), so the surface coverage of H_{ads} is assumed to be zero, and (b) the rate determining step is (3.49d), which explains the appearance of θ_{OH} and θ_{CO} in equation (3.50). Liu and Wang [44] further made the assumption that reaction rates of MOR and ORR determined by (3.50) and (3.48) are unaffected by the fact that both MOR and ORR occur simultaneously in the same electrode; we also use this assumption in our implementation of this model. Finally, reference [44] also describes a purely chemical reaction of CH_3OH with O_2; this purely chemical reaction, represented by equation (1.1c), gives crossed-over CH_3OH an alternative reaction path, which has no affect on the cathode potential. The rate for this chemical reaction is given by

$$r_{chem} = aK_r \left[c_g^{MeOH}\right]^{\beta} \left[c_g^{O_2}\right]^{\gamma} \tag{3.54}$$

where r_{chem} = volumetric chemical reaction rate in cCL (mol m^{-3} s^{-1})

It is important to note that because the MOR and ORR are electrochemical reactions, the cathode potential, V_{cath}, plays a strong role in determining the ORR and MOR reaction rates (see equations (3.50) and (3.48)). In electrochemistry, the cathode potential is defined as the electrode phase potential minus the electrolyte phase potential within the given electrode (in this case the cathode catalyst layer) [86]. The ORR cathode overpotential is related to the cathode potential in the following manner:

$$-\eta_c = V_{cath} - U_o^{ORR} \tag{3.55}$$

where U_o^{ORR} = standard ORR equilibrium potential (1.23 V)

Note here that the negative sign on the left hand side essentially defines η_c as positive, and is therefore consistent with the use of η_c in equaion (1.21), and a positive value of $j^{ORR}_{cathode}$ for a cathodic current, as given in reaciton (1.1b).

Figure 3.5 shows the CO and OH surface coverages and figure 3.6 shows the product of $\theta_{CO}\theta_{OH}$ and corresponding MOR reaction rate, all versus cathode potential, for MeOH concentrations of 0.25, 0.5, 0.75, and 1M. It is evident from figures 3.5 and 3.6 that a changing cathode potential, V_{cath}, will strongly effect the rate at which the crossed-over methanol is oxidized, i.e. the value of $j^{MOR}_{cathode}$ in equation (3.50).

The total ORR rate depends on both the H^+ crossing the membrane from the anode and H^+ produced by MOR in the cathode, by crossed-over CH_3OH:

$$j_{cathode}^{ORR} = j_{cathode}^{MOR} + j_{cathode}^{ORR,H^+,Mem} \tag{3.56}$$

where $j_{cathode}^{ORR,H^+,Mem}$ = ORR current in cCL due to H^+ crossing membrane from anode (A m^{-3})

We assume in this work that the H^+ that crosses the membrane reacts uniformly in the cathode catalyst layer. Based on this assumption, from the conservation of H^+ in the cathode catalyst layer, we get

$$j_{cathode}^{ORR,H^+,Mem} = \frac{i}{\delta_{cCL}} \tag{3.57}$$

Substituting this expression into (3.56), gives the following relationship:

$$j_{cathode}^{ORR} = j_{cathode}^{MOR} + \frac{i}{\delta_{cCL}} \tag{3.58}$$

Note further, that the average cell current density, i, is an input to our DMFC model.

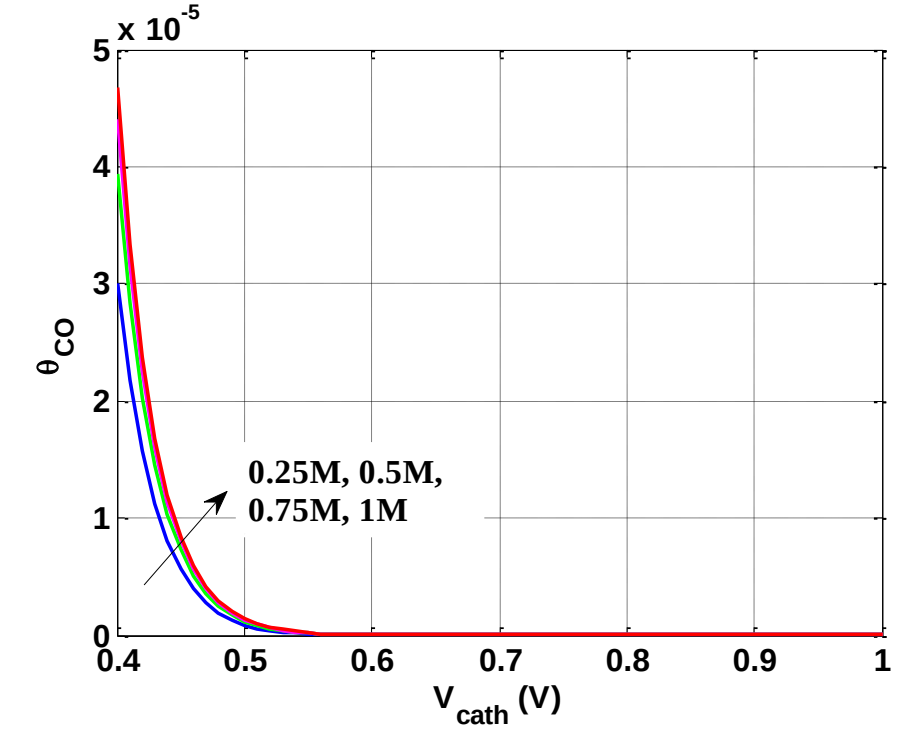

(a)

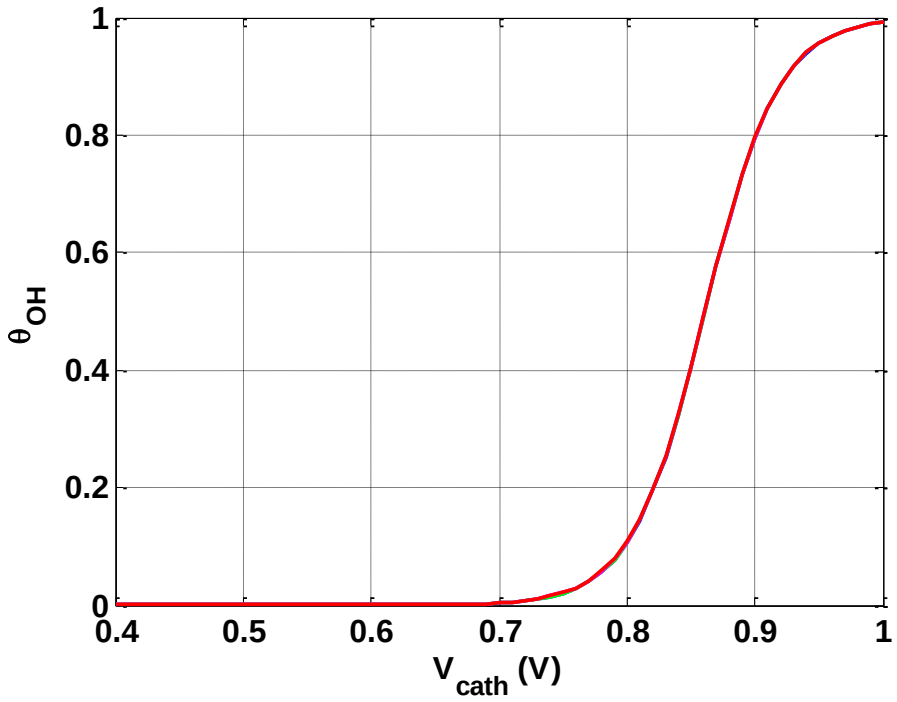

(b)

Figure 3.5. Surface coverages of (a) CO_{ads} and (b) OH_{ads} for the mixed potential model at MeOH concentrations 0.25, 0.5, 0.75, and 1M; note in (b) all concentrations essentially give the same curve.

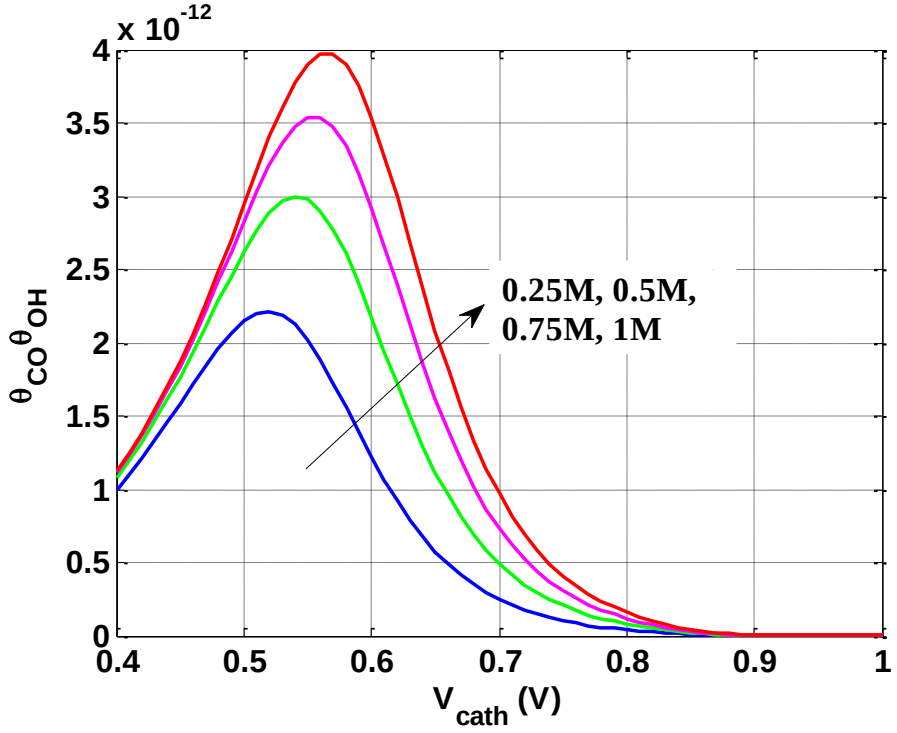

(a)

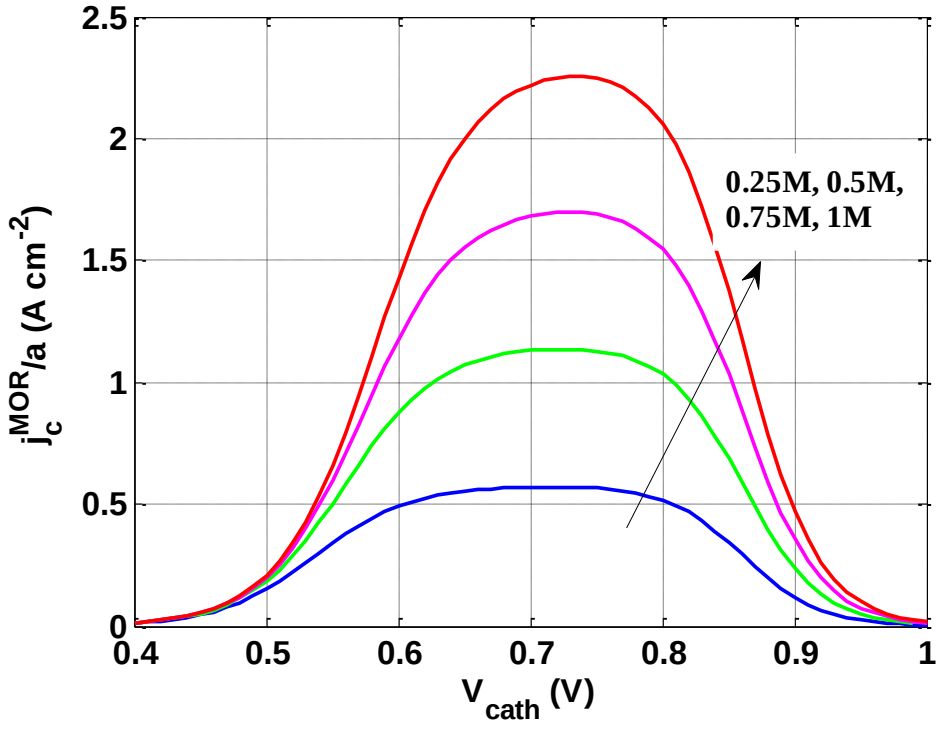

(b)

Figure 3.6. (a) $\theta^{CO}\theta^{OH}$ and (b) j_c^{MOR}/a for the mixed potential model at MeOH concentrations 0.25, 0.5, 0.75, and 1M.

Because $j^{ORR}_{cathode}$ and $j^{MOR}_{cathode}$ both depend on V_{cath}, ultimately what happens is the cathode potential (and corresponding η_c) is determined by an equilibrium value that satisfies equation (3.58). This equilibrium cathode potential is given schematically in figure 3.7 for three cases. Case I is an ideal open circuit (i = 0), where MCO = 0, $\eta_c = 0$, $V_{cath} = U_o^{ORR}$, $j_c^{MOR} = 0$, and $j_c^{ORR} = 0$. Case II is a depiction of real open circuit condition (i = 0), with MCO > 0, $\eta_c > 0$, $V_{cath} < U_o^{ORR}$, $j_c^{MOR} > 0$, and $j_c^{ORR} > 0$. Case III depicts real conditions at operating current (i > 0), with MCO > 0, $\eta_c > 0$, $V_{cath} < U_o^{ORR}$, $j_c^{MOR} > 0$, and $j_c^{ORR} > 0$. We should further point out that in case II, $j^{ORR}_{cathode} = j^{MOR}_{cathode}$ because i = 0 (open circuit), and in case III, $j^{ORR}_{cathode} > j^{MOR}_{cathode}$ because i > 0 (operating current). Physically, we see from figure 3.6b that when $V_{cath} \sim 0.65 - 0.8V$, the kinetics for MOR are better than at other cathode potentials. Therefore, in this range of V_{cath}, the introduction of any further MeOH significantly increases $j^{MOR}_{cathode}$, increases $j^{ORR}_{cathode}$ via equation (3.58), and ultimately leads to a higher η_c when the new equilibrium V_{cath} is reached.

The point should be made that we could simply make the approximation that all crossed-over MeOH reacts uniformly in the cathode catalyst layer, leading to

$$j^{MOR}_{cathode} = \frac{i_x}{\delta_{cCL}} = \frac{N^{MeOH}_{Mem} 6F}{\delta_{cCL}} \tag{3.59}$$

In fact, this is a common assumption in the literature. However, in using the mixed potential model just described, we calculate $j^{MOR}_{cathode}$ and $j^{ORR}_{cathode}$ based on the actual V_{cath} and species concentrations in the cathode catalyst layer. Using our approach yields $j^{MOR}_{cathode}$ which is potentially significantly greater than given by equation (3.59), and allows us to more accurately predict the cell voltage. However, because our approach leads to MOR reaction rates which are higher than required to react all crossed-over

MeOH uniformly in the cathode catalyst layer, this also means that there will be a region of the cathode catalyst layer with MeOH present ($x_{Mem/cCL} < x < x_o^{MeOH}$) and a region without MeOH present ($x_o^{MeOH} < x < x_{cCL/cMPL}$).

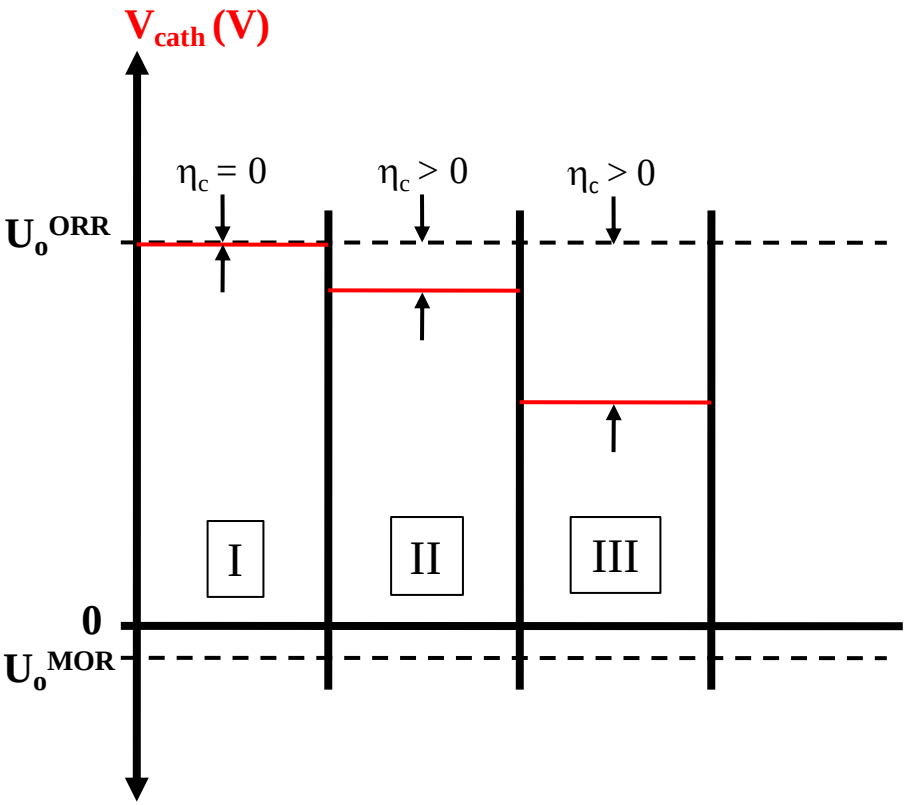

Figure 3.7. Depiction of cathode mixed potential due to MeOH crossover. I: ideal open circuit (i = 0), with MCO = 0, $\eta_c = 0$, $V_{cath} = U_o^{ORR}$, $j_c^{MOR} = 0$, $j_c^{ORR} = 0$; II: real open circuit (i = 0), with MCO > 0, $\eta_c > 0$, $V_{cath} < U_o^{ORR}$, $j_c^{MOR} > 0$, $j_c^{ORR} > 0$; III: real conditions at operating current (i > 0), with MCO > 0, $\eta_c > 0$, $V_{cath} < U_o^{ORR}$, $j_c^{MOR} > 0$, $j_c^{ORR} > 0$.

The species flux terms in the cathode catalyst layer follow directly from the species conservation given by equation (3.7), and the results are given in table 3.1. In our implementation, $\overline{j_{cathode}^{MOR}}$ and $\overline{j_{cathode}^{ORR}}$, and $\overline{r_{chem}}$ are *defined* as their average values in the *region of the cathode catalyst layer where MeOH exists* ($x_{Mem/cCL} < x < x_o^{MeOH}$). Therefore, based on these definitions, in the region ($x_o^{MeOH} < x < x_{cCL/cMPL}$) where there is

no MOR or chemical reaction, the actual ORR current is equal to $\overline{j_{cathode}^{ORR}} - \overline{j_{cathode}^{MOR}}$, which is physically the rate of H^+ reacting in the cCL which have crossed the membrane. As given in table 3.1, the methanol flux in the cCL is straightforward: in the region $x < x_o^{MeOH}$, methanol is consumed by both MOR and the purely chemical reaction, and for $x > x_o^{MeOH}$, there is no methanol, so $N^{MeOH} = 0$. Also in table 3.1, for the flux of H_2O in the region $x < x_o^{MeOH}$, water is consumed by MOR and produced by ORR and the chemical reaction. For the H_2O flux in the region $x > x_o^{MeOH}$, water is produced only by ORR. Finally, in the region $x < x_o^{MeOH}$, O_2 is consumed by both purely chemical reaction and ORR, and in the region $x > x_o^{MeOH}$, O_2 is consumed by ORR.

Our average reaction rates in the region $x < x_o^{MeOH}$, $\overline{j_{cathode}^{MOR}}$ and $\overline{j_{cathode}^{ORR}}$, and $\overline{r_{chem}}$, are based on the average species concentrations in this region, as calculated by equations (3.48), (3.50), and (3.54). The reason that we take the approach of average reaction rates and two regions within the cCL is simple: by doing this we avoid having to solve an additional differential equation for proton transport in the membrane and catalyst layers. Our approach is certainly suitable for our level of modeling, and this approach reduces the complexity and improves the speed of our code. With the implementation of the mixed potential model, the transport equations and electrochemistry become coupled: the reaction rates depend on the species concentrations, and the source terms (species fluxes) for transport listed in table 3.1 depend on the reaction rates. The way we handle this coupling is described in section 3.8.

3.7 Boundary conditions

The MeOH and O_2 concentration boundary conditions (at the backing layer and flow channel interfaces) are estimated based on a simple 1D mass balance analysis of the flow channel:

$$c_l^{MeOH}\Big|_{x=0} = c_{l,0}^{MeOH}\left[1 - \frac{1}{2\xi_a \dfrac{i_{ref,a}}{i}}\right] \tag{3.60}$$

where $c_{l,0}^{MeOH}$ = liquid MeOH concentration at the inlet of the anode flow channel

$c_l^{MeOH}\Big|_{x=0}$ = liquid MeOH concentration at the anode BL/flow channel interface

ξ_a = anode stoichiometry at $i_{ref,a}$

i = current density (A m^{-2})

$i_{ref,a}$ = reference current density anode stoichiometry (A m^{-2})

$$c_g^{O_2}\Big|_{x=x_{cBL/cFC}} = c_{g,0}^{O_2}\left[1 - \frac{1}{2\xi_c \dfrac{i_{ref,c}}{i}}\right] \tag{3.61}$$

where $c_{g,0}^{O_2}$ = gas O_2 concentration at the inlet of the cathode flow channel

$c_g^{O_2}\Big|_{x=x_{cBL/cFC}}$ = gas O_2 concentration at the cathode BL and flow channel interface

ξ_c = cathode stoichiometry at $i_{ref,c}$

i = current density (A m^{-2})

$i_{ref,c}$ = reference current density cathode stoichiometry (A m^{-2})

The stoichiometry is used frequently in fuel cell terminology, and is a way of describing the flow rate of the fuel supplied to the cell. The stoichiometry is defined as the ratio of the flow rate of fuel supplied (in this case MeOH and O_2) to the stoichiometric amount required at a specified reference current density. It is evident from (3.60) and (3.61) that as the stoichiometry is increased, the boundary MeOH concentration increases, and as the current density is increased, the MeOH concentration decreases.

The anode and cathode liquid saturation boundary conditions are assumed to be

$$s\big|_{x=0} = 0.8 \tag{3.62}$$

$$s\big|_{x=x_{cBL/cFC}} = \begin{cases} 0.1 & i < i_{ref} \\ 0.1\left(\dfrac{i}{i_{ref}}\right)^{1.5} & i > i_{ref}\text{, maximum of } 0.95 \end{cases} \tag{3.63}$$

where $i_{ref} = 1000$ A m^{-2}

For the MeOH transport in the cathode catalyst layer, the concentration is assumed to be zero at $x = x_{cCL/cMPL}$ (interface between cathode catalyst layer and cathode MPL). This is a physically reasonable assumption, as it has been shown experimentally that all MeOH that crosses through the membrane is completely reacted into CO_2 (see, e.g. [87]). However, with the implementation of the cathode detailed electrochemistry model, the reaction rates of MeOH in the cathode catalyst layer are determined dynamically by the saturation levels, MeOH concentration, cathode potential, etc. In other words, we cannot assume arbitrarily that the MOR and chemical reaction rates are such that the MeOH concentration goes to zero exactly at $x = x_{cCL/cMPL}$. The code has been written to account for this phenomenon in the following manner. Based on the current iteration value for $\overline{j_{cathode}^{MOR}}$, $\overline{j_{cathode}^{ORR}}$, and $\overline{r_{chem}}$, the MeOH flux in the cathode

catalyst layer is determined using the equation given in table 3.1. At the first node where the MeOH flux is calculated as a zero value, the code sets the location of x_o^{MeOH}. Because the MeOH flux is zero for $x > x_o^{MeOH}$, the condition that $c_l^{MeOH}\Big|_{x=x_{cCL\,/\,cMPL}} = 0$ can be used directly, as the MeOH concentration will remain zero at all $x > x_o^{MeOH}$. This treatment is necessary in order to have a Dirichlet boundary condition for the MeOH concentration on the cathode side, and hence a well-posed problem.

It should also be noted that when a single(vapor)-phase region is encountered on the anode side of the cell, the boundary conditions for the water and methanol concentrations are taken from their values at the two-phase/single-phase interface. Concentrations of these species are solved for in the two-phase region, so no extra assumptions are needed.

3.8 Numerical implementation

Figure 3.8 gives the basic flow chart of the 1D simulation code. The MeOH membrane flux, H_2O membrane flux, chemical reaction rate in the cathode CL, and ORR reaction in the cathode CL all act essentially as nonlinear source terms in the species transport and liquid flow equations. In order to create a robust, well-behaved code, these terms have been decoupled from the main loop that solves the field variables (e.g. c_l^{MeOH}, s). Based on the current iteration value of $\overline{j_{cathode}^{ORR}}$, $\overline{r_{chem}}$, N_{Mem}^{H2O}, and N_{Mem}^{MeOH}, the inner-most loop solves iteratively for all of the field variables from the differential equations. Based on this solution, the value of the source term variables are calculated and compared with the guessed value from the previous iteration. As illustrated in figure 3.8, the source term variables each have their own iteration loop, leading to a nested set

of loops. A hybrid secant, bi-section method is utilized to iterate the values of the source term variables, while first-order difference methods are used for the differential equations solved for species concentrations and liquid saturation. More details can be found in Appendix B.

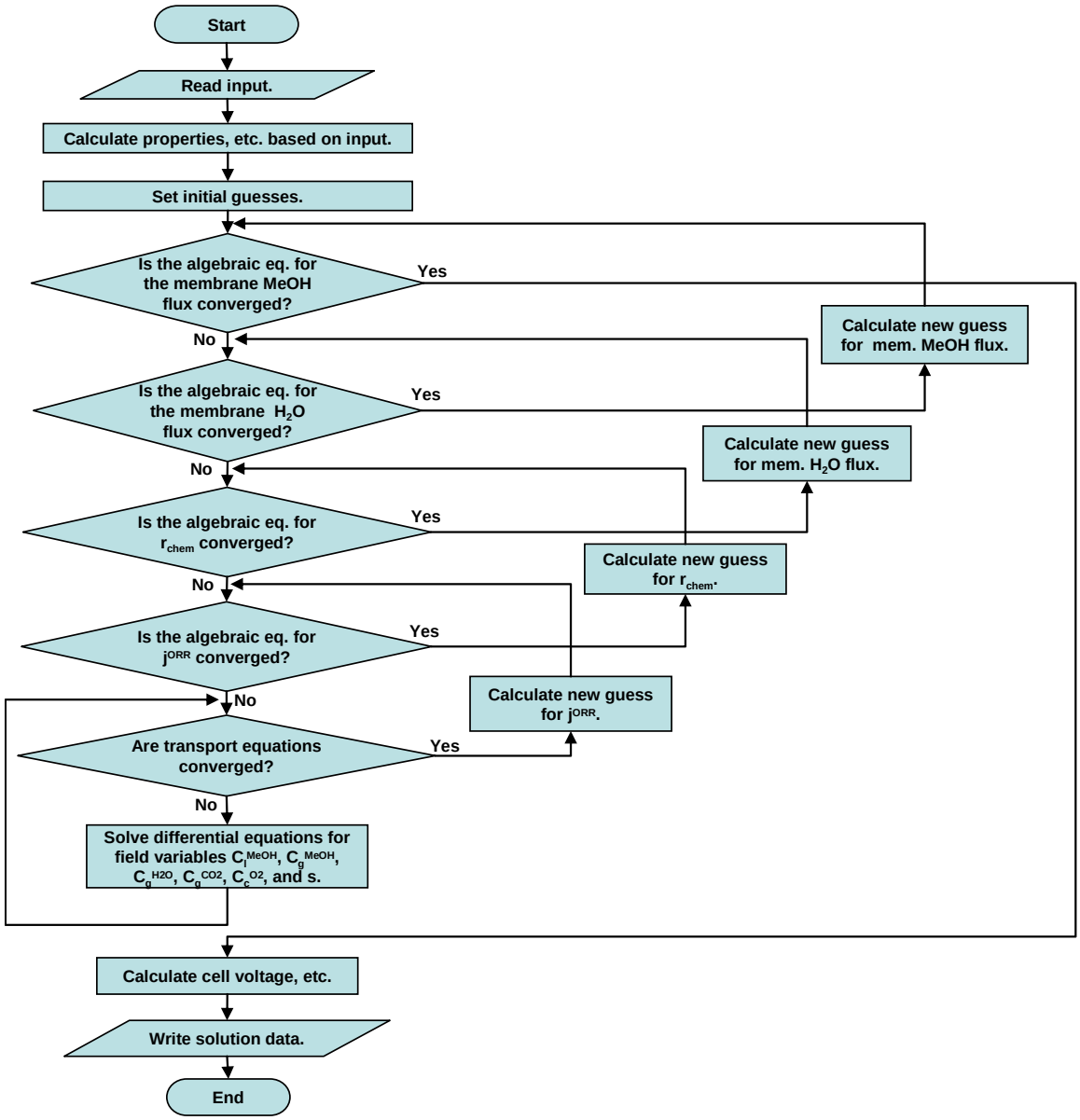

Figure 3.8. Flow chart for 1D code.

In order to ensure a converged solution, the maximum absolute relative error of each variable is compared with an error tolerance of at most 10^{-4}. Additionally, for the

source term variables the residuals of the algebraic equations are compared with the converged value to ensure that the residual is at least three orders of magnitude smaller (see Appendix B). Finally, we have carried out graphical grid independence to verify a sufficient grid size.

Chapter 4. Understanding the Importance of Fuel and Water Balance

As discussed in section 1.9, from a system standpoint, in order for us to directly use concentrated methanol fuel, proper water management -- achieving a low α -- is a critical prerequisite. This concept, based on overall CH_3OH and H_2O species balance, was nicely summarized by figure 1.9, which gives the CH_3OH fuel concentration required for complete use of CH_3OH and H_2O carried in the DMFC system, as a function of α and MCO. Our goal in this chapter is to go through a series of examples which emphasize this point in a heuristic manner, and further reveal the interplay between fuel and water management, particularly as it relates to MEA design and the physics which occur in the MEA.

On the anode side of the cell, the capillary action acts to transport the methanol-water mixture from the flow channel to the catalyst layer. The flux of a given species, β, in the liquid phase can be represented by a convective flux plus a diffusion flux:

$$\vec{N}_l^{\beta} = X_l^{\beta}\vec{N}_l + \vec{j}_l^{\beta} \qquad (4.1)$$

where N_l^{β} = mole flux of species β in the liquid phase (mol $m^{-2}s^{-1}$)

X_l^{β} = mole fraction of species β in the liquid phase

N_l = total mole flux of the liquid phase (mol $m^{-2}s^{-1}$)

j_l^{β} = mole diffusion flux of species β in the liquid phase (mol $m^{-2}s^{-1}$)

The liquid phase is a binary mixture of methanol and water, and therefore the concentration gradients must be in opposite directions of one another.

Utilizing the 1D model described in chapter 3, which fully accounts for the capillary-induced liquid flow in the porous media, figure 4.1 illustrates the liquid

methanol and H_2O concentration profiles across the anode diffusion media for MCO = 0 (the ideal situation) and α = 3.0, 2.0, and 1.0, for the cell properties given in table A.1. It is important to note in these plots that a perfectly horizontal line signifies an equivalent molar ratio of methanol to H_2O at the backing layer (BL), flow channel interface and in the anode catalyst layer (CL). These horizontal lines indicate the following equivalent ratio (under steady-state conditions):

$$\left.\frac{\begin{pmatrix} CH_3OH \text{ reacted} + \\ CH_3OH \text{ crossed over} \end{pmatrix}}{\begin{pmatrix} H_2O \text{ reacted} + \\ H_2O \text{ crossed over} \end{pmatrix}}\right|_{molar} = \left.\frac{(CH_3OH)}{(H_2O)}\right|_{\substack{molar \\ fuel\ feed}} \tag{4.2}$$

A smaller α decreases the denominator on the left-hand side of equation (4.2), and the ratio on the right-hand side increases; a larger ratio on the right-hand side indicates a higher fuel concentration. Correspondingly, in figure 4.1 we see that as α decreases, the methanol concentration to maintain this equivalency (horizontal line) increases: roughly 2 – 3 M, 4 M, and 7 M for α = 3.0, 2.0, and 1.0, respectively. Note that a methanol concentration with positive slope indicates a cell with a less than sufficient source of H_2O from the cathode (i.e. losing too much water to the cathode through the membrane), which will run short of water before methanol over time. These plots are very useful in demonstrating that even for an ideal membrane that blocks all methanol transport from the anode to cathode, developing an MEA with low (even negative) water crossover is critically important in designing a DMFC with high energy density operating on highly concentrated methanol fuel.

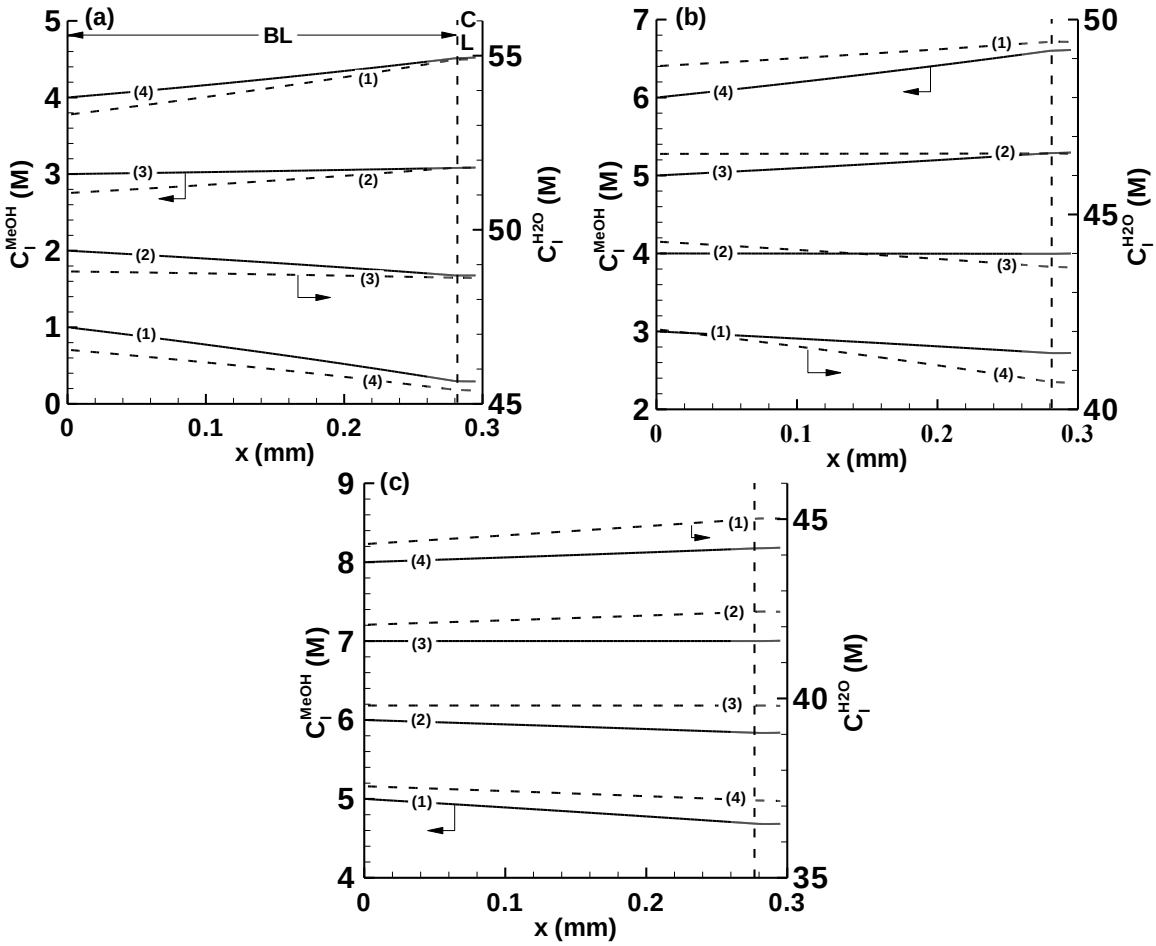

Figure 4.1. Liquid CH_3OH and H_2O concentration profiles for MCO = 0, i = 150 mA cm^{-2}, and: (a) $\alpha = 3.0$; (b) $\alpha = 2.0$, and (c) $\alpha = 1.0$. Curves (1), (2), etc. stand for the corresponding profiles for the various boundary methanol concentrations at x = 0. Note x = 0 is at the anode BL and channel interface; x = 0.295 mm is at the anode CL and membrane interface. Cell properties given in table A.1.

It is important to note in figure 4.1 that an increasing methanol concentration towards the anode CL (positive x-direction) only implies a *diffusion* flux in the binary liquid phase away from anode CL (negative x-direction). This does not imply a net transport of methanol away from the anode CL, a fact which is illustrated by looking at equation (4.1). Here we see that the capillary-induced liquid flow can facilitate a net flux of methanol towards the anode CL (positive x-direction), against a concentration gradient, when methanol concentration becomes high (large value of X_l^{CH3OH}). This is

exactly what we see in figure 4.1, and the exact same concept holds for H_2O transport through the porous media.

In any realistic membrane, there is some degree of methanol crossover. The methanol flux across the membrane is driven by EOD and diffusion, as given by equations (2.5), (2.6), and (3.11). The methanol diffusion flux across the membrane is obviously a function of the methanol concentration in the anode CL, and so too is the EOD flux due to the EOD coefficient dependence on methanol concentration. Therefore, for reasons of reducing the MCO, it is important to reduce the methanol concentration in the anode CL. As shown in figure 4.2 (as well as figure 4.1), one effective way of accomplishing this is by reducing α for a given methanol concentration. Physically, the less water lost to the cathode side of the cell, the lower the methanol concentration in the anode CL. Note that in figure 4.2, we set MCO = 0.1 to highlight this point; in reality, the MCO is dynamically a function of the methanol concentration.

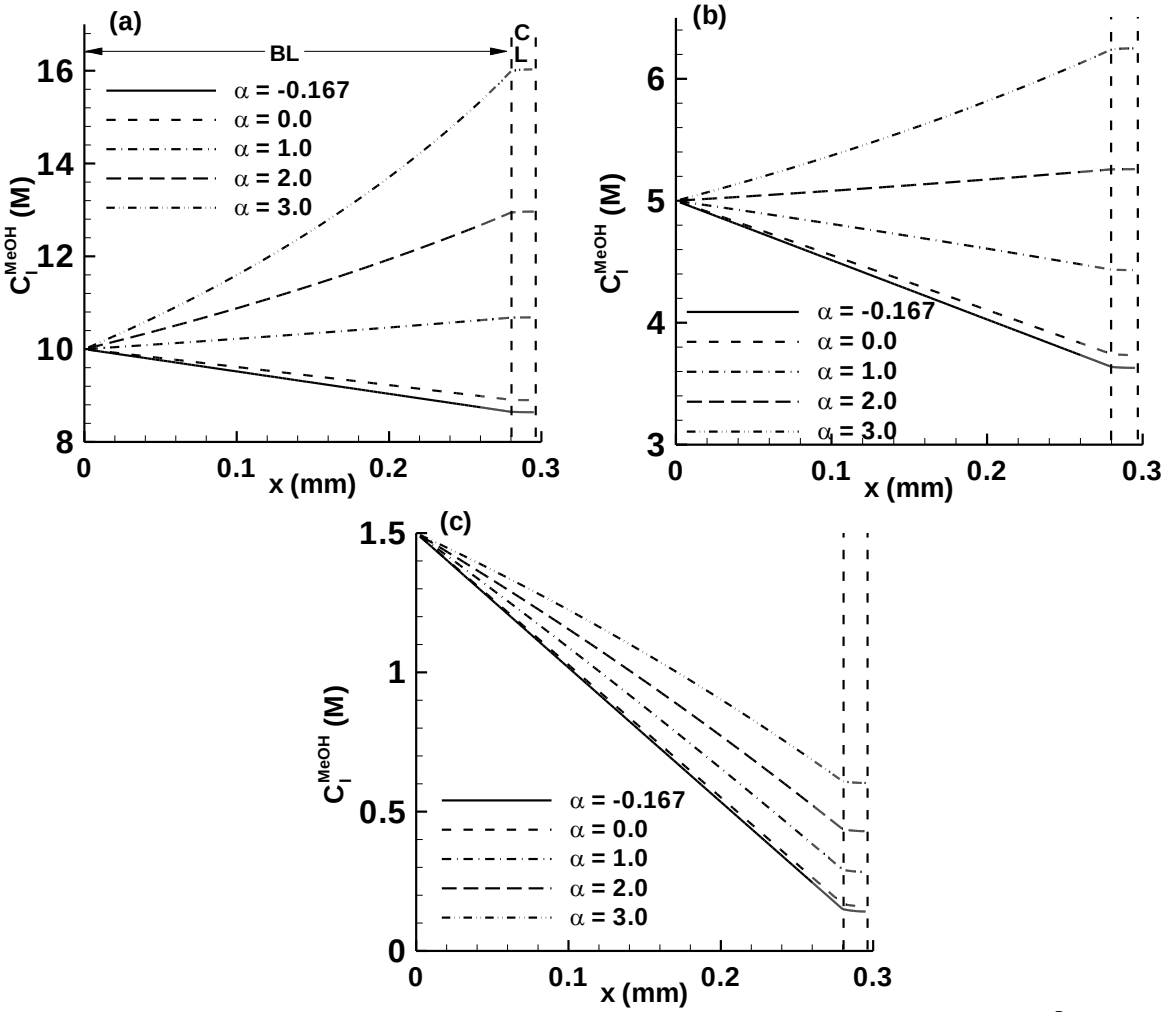

Figure 4.2. Liquid methanol concentration profiles for MCO = 0.1, i = 200 mA cm^{-2}, and α = 3.0, 2.0, 1.0, 0.0, and -1/6, for: (a) 10 M, (b) 5 M, and (c) 1.5 M boundary methanol concentrations. Note x = 0 is at the anode BL and channel interface; x = 0.295 mm is at the anode CL and membrane interface. Cell properties given in table A.1.

As an additional example of the importance of water management on using high concentration methanol fuel, we give a hypothetical cell design with the MCO determined dynamically, and membrane water crossover set to zero (α = 0.0). Figure 4.3 illustrates the liquid methanol and water concentration profiles in the anode under 10 M MeOH boundary concentration. This cell has an additional porous barrier between BL and CL with ε = 0.25, θ = 120°, δ = 250 μm and all other properties the same as given in

table A.1 for a BL. The methanol crossover ratio is simulated to be MCO = 0.13 at i = 250 mA cm^{-2} which is due in large part to the reduction of methanol concentration in the anode CL, as seen in figure 4.3. The point to take here is that if we can design an MEA that reduces $\alpha \sim 0$ while simultaneously adding a barrier to methanol and water transport in the anode, we can operate the cell at a high fuel efficiency (MCO = 0.13) while using concentrated fuel (10 M), all without external means of water recovery. Here, the barrier between the anode BL and CL provides not only a high resistance to methanol transport, but also prevents water from diffusing back from the anode CL into the fuel channel.

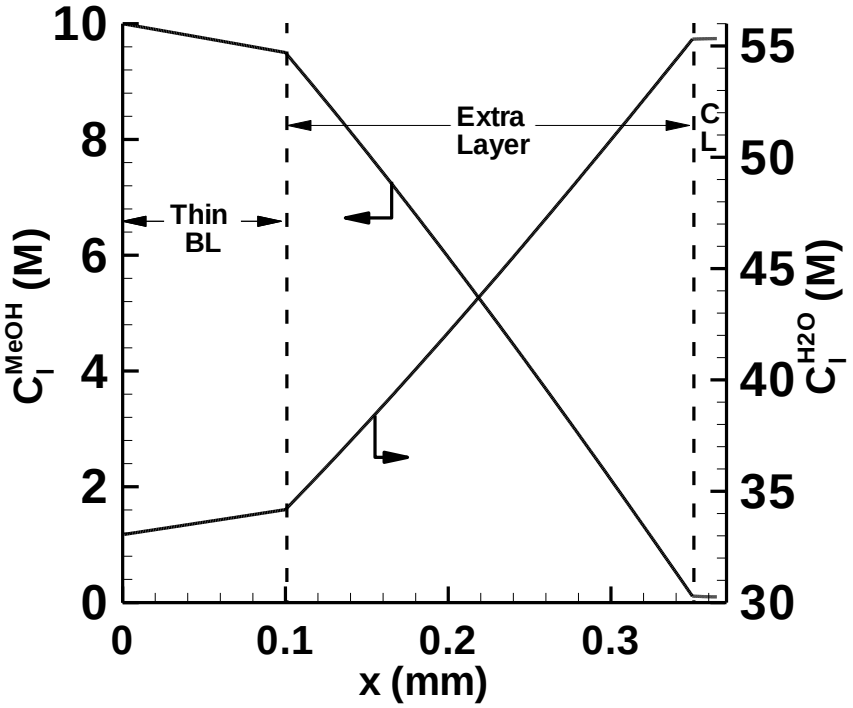

Figure 4.3. Liquid CH_3OH and H_2O anode concentration profiles for $\alpha = 0.0$, and i = 250 mA cm^{-2}. The extra layer between BL and CL has all BL properties given in table A.1 except $\varepsilon = 0.25$, $\theta = 120^o$, and $\delta = 250$ μm. Note that x = 0 is at the anode BL and channel interface.

One further example of the importance of water crossover on high concentration DMFC performance is given in figure 4.4. Here we show fuel efficiency curves for α = -

1/6, 0, 1, and 2 for (a) 5 M and (b) 3 M methanol fuel concentrations. Note that the fuel efficiency is defined as

$$\eta_f = \frac{i}{i + i_x} = 1 - MCO \tag{4.3}$$

It is evident from figure 4.4 that the fuel efficiency increases with lower α as should be expected from the previous discussions on reducing MCO via lower methanol concentration in the anode CL. It should now be unambiguous how water management plays a critical role for the use of concentrated methanol fuel in DMFCs, particularly from an MEA design and performance standpoint.

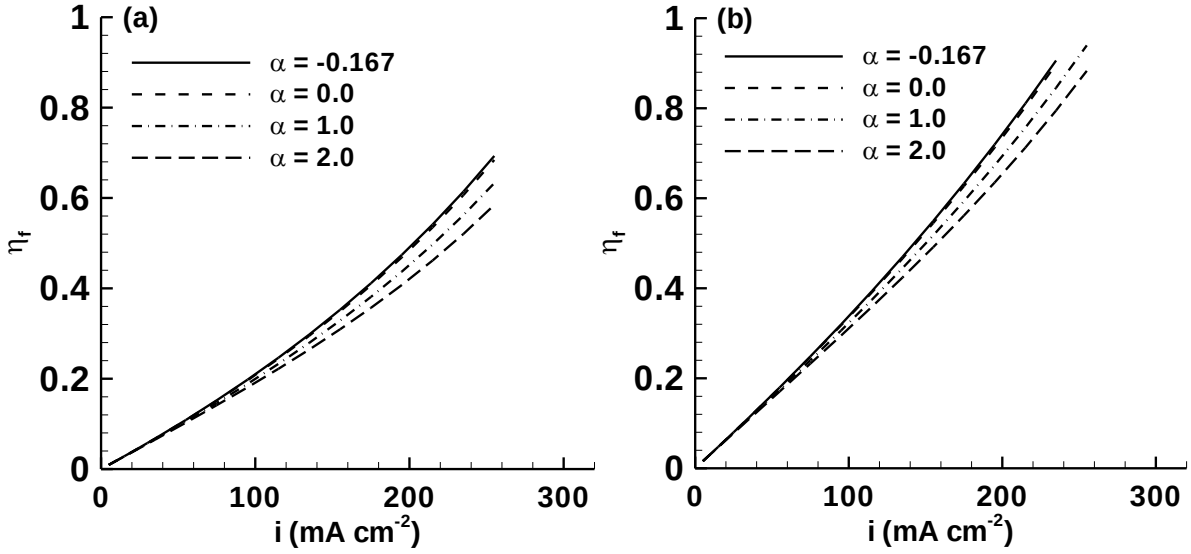

Figure 4.4. Fuel efficiency versus current density for: (a) 5 M and (b) 3 M methanol fuel concentrations; note anode and cathode stoichiometries of 1.75 @ 150 mA cm^{-2}. Cell properties given in table A.1.

We would be remiss to end this chapter without a brief discussion of the role of the membrane in water and fuel management. After all, the primary goal of fuel management is to reduce the MeOH crossing from anode catalyst layer to cathode catalyst layer, through the membrane, and the primary goal of water management is to

reduce the transport of water from the anode catalyst layer to the cathode catalyst layer, through the membrane. Tables 4.1 and 4.2 give the simulated membrane thickness and H_2O membrane diffusivity effects on α for an MEA design with hydrophobic anode and cathode MPLs. It is seen that a thinner membrane and membrane with greater H_2O diffusivity actually reduce water loss to the cathode. Table 4.1 shows that α = 0.293 for a membrane thickness of 50 μm (roughly Nafion® 112) and α = 0.695 for a thickness of 175 μm (roughly Nafion® 117) from simulated results; table 4.2 illustrates that a membrane H_2O diffusivity of one order of magnitude greater reduces α to 0.05, while an order of magnitude lower increases α to 0.878. Note that a lower water crossover to the cathode with thinner membrane is in good qualitative agreement with the experimental findings for low-α MEAs (see table 1.2), but goes against classic thinking developed for traditional MEA designs. Therefore, an ideal membrane, as a component in a low-α MEA, will have low methanol permeability, low methanol EOD, and high proton conductivity, but high water diffusivity. Further, we should note that a thin membrane, low-α MEA can be designed to ensure low MCO (~ 0.1 – 0.2) at a given operating current density.

Table 4.1. α versus membrane thickness at 200 mA cm^{-2} with anode and cathode MPLs; anode and cathode stoichiometries of 1.75 @ 150 mA cm^{-2} with 3 M fuel. Cell properties given in table A.1.

δ_{Mem} / μm	α
50	0.293
100	0.527
150	0.654
175	0.695

Table 4.2. α versus membrane H_2O diffusivity at 200 mA cm^{-2} with anode and cathode MPLs; anode and cathode stoichiometries of 1.75 @ 150 mA cm^{-2} with 3 M fuel; D_o^{H2O} is the baseline value as given in table A.5. Cell properties given in table A.1.

$\mathbf{D_{Mem}^{H2O}}$	**α**
$D_o^{H2O}x10^{-1}$	0.878
D_o^{H2O}	0293
$D_o^{H2O}x10^{1}$	0.050

Chapter 5. Role of Hydrophobic Anode MPL in Reducing Water Crossover

The traditional MEA for DMFCs has a BL and CL on each side of the membrane. However, with the advent of low-α MEA technology, it has become common to use a hydrophobic MPL between the cathode BL and CL, in effort to reduce the water crossover [55,56,57, 58,59,63,64,66]. As mentioned in Chapter 1, Liu [61,62] and Park *et al.* [65] have recently further demonstrated experimentally that the inclusion of a hydrophobic anode MPL further significantly lowers α.

Our primary goal in this chapter is to develop a theoretical explanation of the observed water crossover reduction with the inclusion of a hydrophobic anode MPL. Further, based on the developed theory, we will determine parametrically the properties which make a more effective hydrophobic anode MPL, in terms of water crossover reduction. Finally, we briefly discuss the effects of the hydrophobic cathode MPL, why an MEA with both hydrophobic anode and cathode MPLs is most effective, and specifically, how the anode and cathode MPLs work together in an MEA to reduce water crossover.

5.1 Theoretical explanation of water crossover reduction with hydrophobic anode MPL

Table A.2 gives the baseline DMFC parameters used for the results presented in figures 5.1 through 5.10. Figure 5.1(a) illustrates the net water transport coefficient versus cell current density, and figure 5.1(b) gives the EOD, diffusion, and hydraulic-

permeation components of α both for the baseline cell with and without the aMPL. Note that the α components are simply the H_2O membrane flux components given in eq. (2.1) times (F/i) (e.g. $\alpha_{EOD} = n_d^{H2O}$). The effectiveness of the hydrophobic aMPL in reducing α is clear from these plots; without the aMPL present, α is ~ 2.0 - 2.2, but is reduced to 0.25 – 0.4 with the aMPL in the operating current density range of 150 – 200 mA cm^{-2}. Figure 5.1(b) clearly shows that the MEA with aMPL has significantly lower EOD and significantly greater back diffusion from cathode to anode. The near-zero value of α_{HP} is in part due to the fact that we are simulating a cell with the same CL and MPL properties on each side of the membrane, thereby making it difficult to generate a large gradient of liquid pressure across the membrane. The liquid saturation profiles given in figure 5.2 for various current densities help to explain physically how the hydrophobic aMPL causes this considerable reduction in α. At each of the three current densities, the liquid saturation level in the aCL is lower with the hydrophobic aMPL present than without. This reduction in aCL saturation acts to both reduce the EOD coefficient and increase the difference in water content across the membrane, thereby increasing back diffusion from cathode to anode.

The lower liquid saturation level in the aCL is caused by the hydrophobic nature of the aMPL in the following manner. The saturation level in the aMPL is far lower than in the aBL due to the continuous capillary saturation condition at their interface, and subsequent saturation jump. At a lower saturation level, the liquid-phase relative permeability is much lower. As evidenced by equation (3.41), for a given liquid flux, a significantly lower k_{rl} leads to a greater gradient in liquid saturation, ds/dx, and a significantly larger drop in saturation over the aMPL thickness, when compared with an

equivalent length aBL section. This large drop in liquid saturation over the thickness of the aMPL ultimately leads to a significantly different capillary pressure, p_c, at the aCL interface, as compared with only aBL present. As per equations (2.20a) and (2.20b), this different capillary pressure leads to a reduced saturation level in the aCL. It is therefore the saturation jump at the aBL/aMPL interface coupled with the low liquid-phase permeability at low saturation (in the aMPL) that lead to the low aCL saturation, and the reduction in α as described. Put simply, the hydrophobic nature of the anode MPL acts as an inhibitor to the liquid flow from anode flow channel to anode CL, and this ultimately leads to a dryer aCL. This dryer aCL effectively acts to increase back diffusion of H_2O from the cCL, reduce the EOD of H_2O, ultimately leading to a lower α.

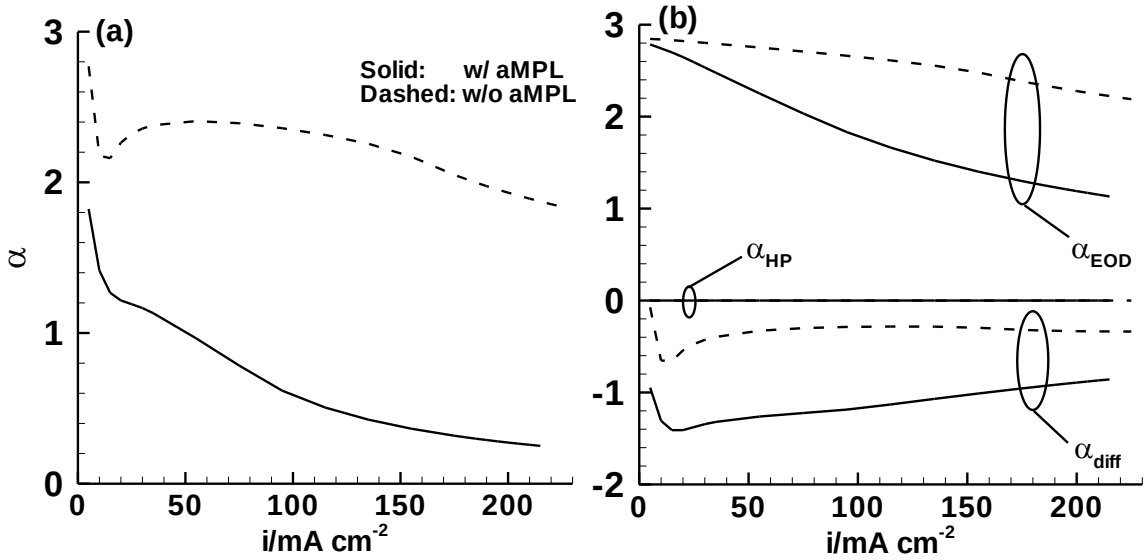

Figure 5.1. (a) Net water transport coefficient (α) and (b) electro-osmotic drag (EOD), diffusion (diff), and hydraulic pressure (HP) α components vs. cell current density with and without hydrophobic anode micro-porous layer (aMPL). Cell properties and simulation parameters given in table A.2.

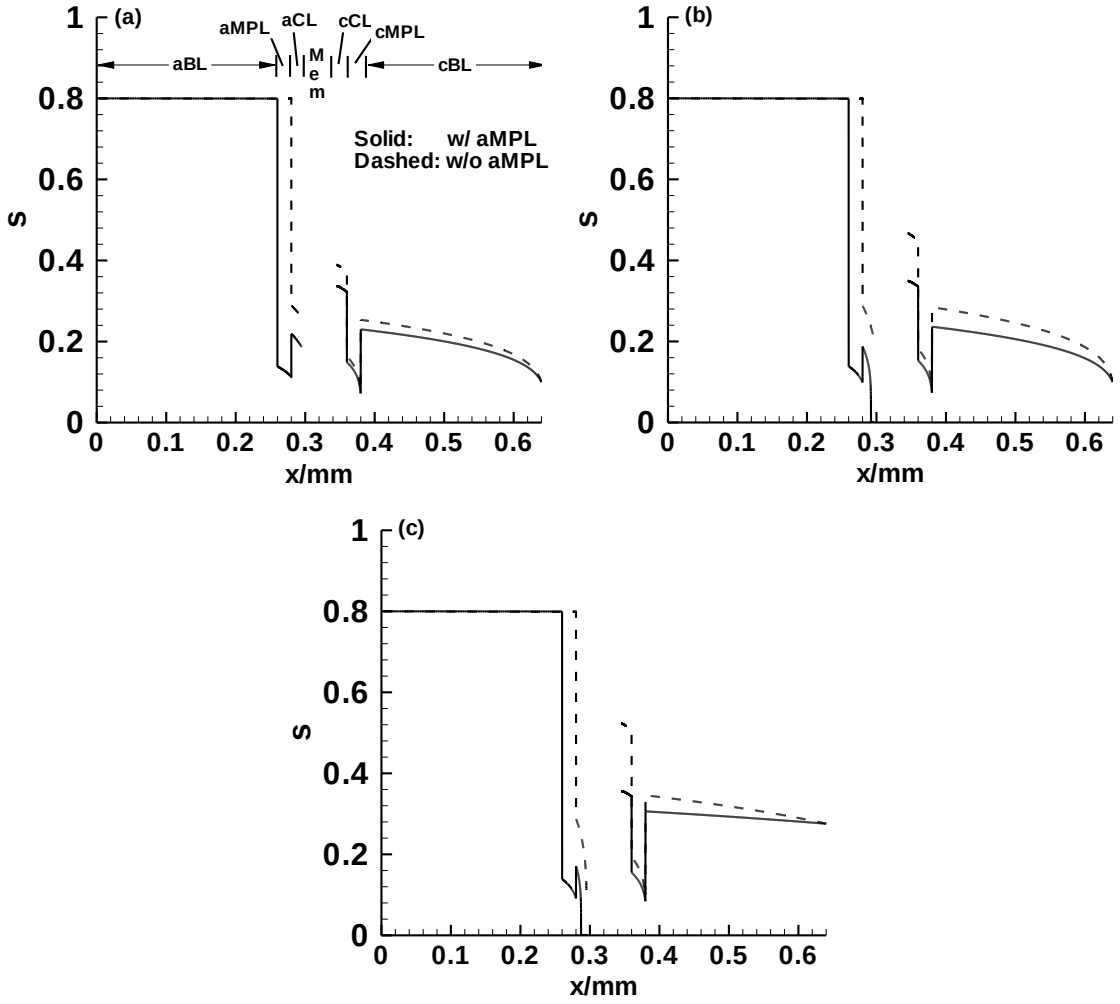

Figure 5.2. Saturation profiles with and without hydrophobic anode micro-porous layer (aMPL); (a) i = 50 mA cm^{-2}, (b) i = 100 mA cm^{-2}, (c) i = 150 mA cm^{-2}. Cell properties and simulation parameters given in table A.2.

From figure 5.3 we see that in addition to reducing the water crossover, a hydrophobic aMPL also slightly reduces the methanol crossover to the cathode. At any given current density, it is evident from figure 5.3 that the MCO is lower with hydrophobic aMPL present, i.e. the fuel efficiency is higher. This is a direct consequence of the dilution effect a lower α has on the methanol concentration in the aCL as discussed in chapter 4. Figure 5.4 further illustrates this point, showing the methanol and H_2O liquid concentration profiles in the anode with and without hydrophobic aMPL at i = 150

mA cm^{-2}. Here we see that with the hydrophobic aMPL present, the methanol concentration is less than, and the H_2O concentration is greater than their corresponding values without the aMPL. From equations (2.6) and (3.11) we see that the EOD and diffusion components of MeOH crossover are both increasing functions of the methanol concentration in the aCL, and hence it is clear that the dilution effect causes a lower MCO.

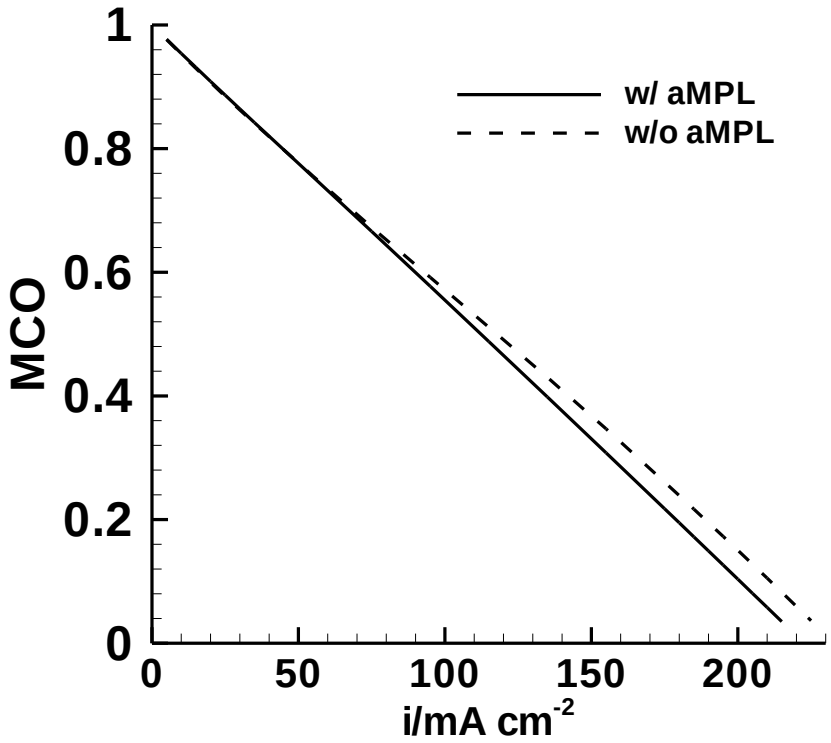

Figure 5.3. Methanol crossover ratio (MCO) vs. cell current density with and without anode micro-porous layer (aMPL). Cell properties and simulation parameters given in table A.2.

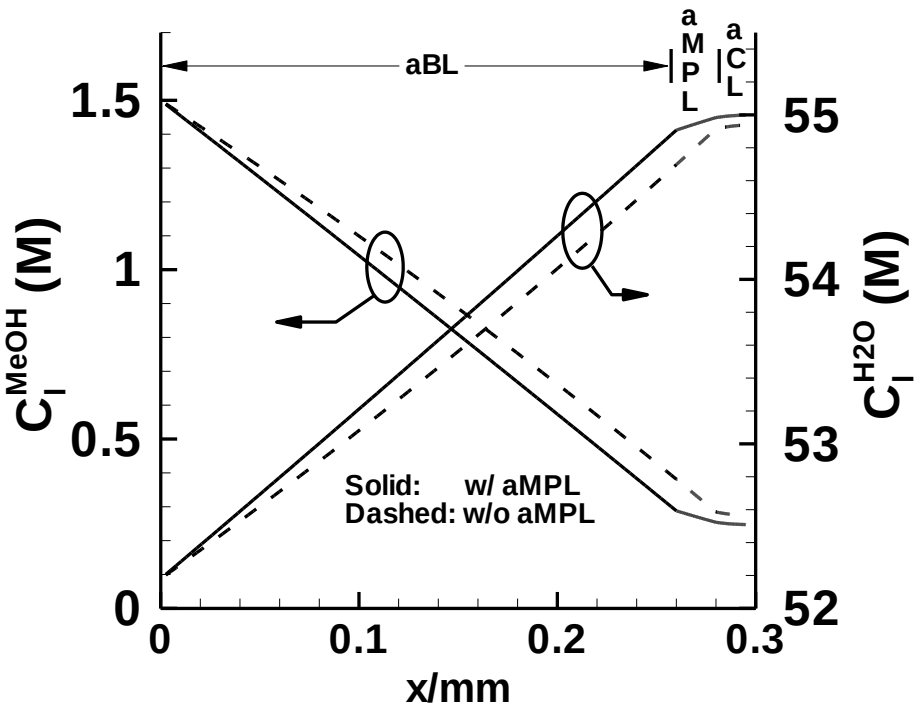

Figure 5.4. Liquid CH_3OH and H_2O anode concentration profiles with and without hydrophobic anode micro-porous layer (aMPL) at i = 150 mA cm^{-2}. Cell properties and simulation parameters given in table A.2.

5.2 Parametric study – effect of anode MPL properties

Contact angle

Figure 5.5 shows the α versus current density curves for a cell with the baseline parameters given in table A.2, except with varying aMPL contact angle. It is evident that a higher contact angle (i.e. more hydrophobic to methanol-water solutions) yields a lower water crossover, with α ranging from ~ 1.3 - 1.6 for $\theta_{aMPL} = 110^o$ to ~ 0.1 – 0.2 for $\theta_{aMPL} = 125^o$ in the current density range of i = 150 – 200 mA cm^{-2}. Figure 5.6 illustrates that the greater hydrophobicity acts to increase the saturation jump at the aBL/aMPL interface, thereby reducing the saturation level in the aMPL. As described in section 5.1, this lower aMPL saturation level ultimately acts to reduce the liquid saturation level in the aCL, thereby reducing α. Summarized physically, a greater anode MPL

hydrophobicity creates a greater resistance to liquid flow, a drier anode catalyst layer, and ultimately a lower α, by pulling in more water from the cathode catalyst layer via back diffusion, and reducing the EOD of water. With regards to figure 5.6, it is worth mentioning that the changing saturation profile on the cathode side of the membrane, caused by changing anode MPL contact angle, occurs simply due to a new equilibrium membrane water flux being reached with different anode MPL properties. Obviously, different anode MPL properties have no direct influence on anything that happens on the cathode side of the membrane.

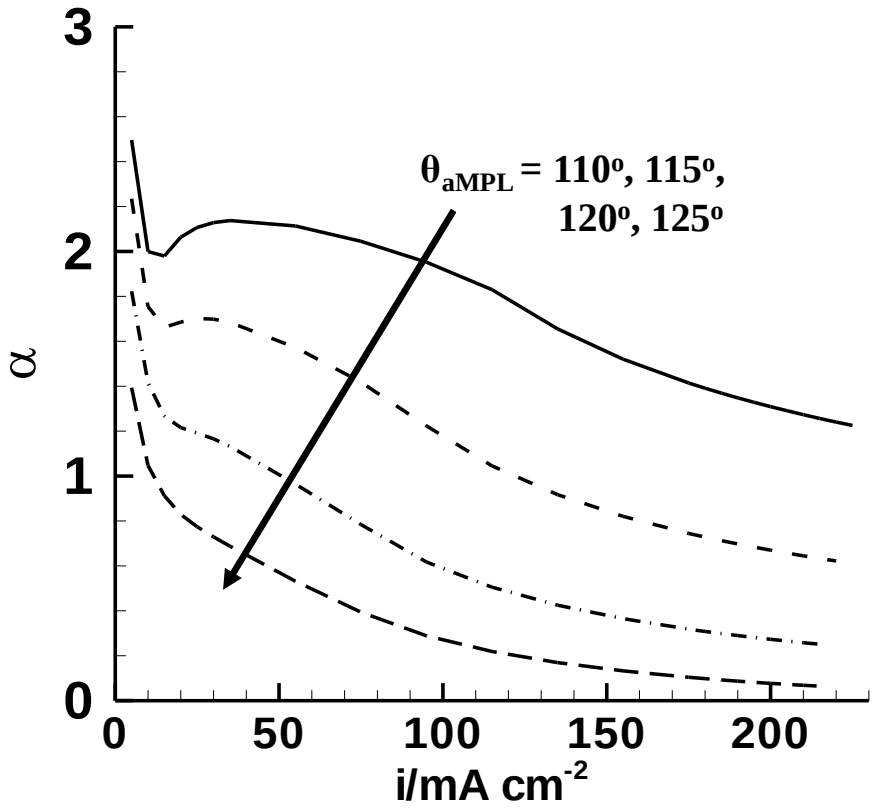

Figure 5.5. Net water transport coefficient (α) vs. cell current density for anode micro-porous layer (aMPL) contact angles θ_{aMPL} = 110°, 115°, 120°, and 125°. Cell properties and simulation parameters given in table A.2.

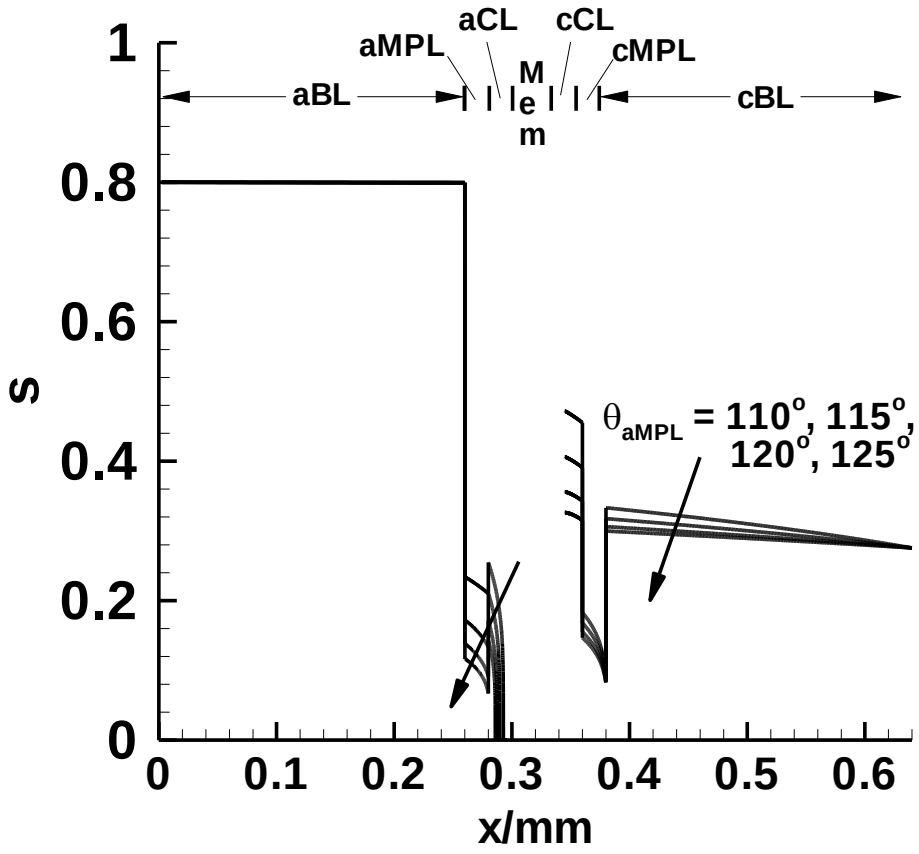

Figure 5.6. Liquid saturation profiles for anode micro-porous layer (aMPL) contact angles θ_{aMPL} = 110°, 115°, 120°, and 125°; i = 150 mA cm^{-2}. Cell properties and simulation parameters given in table A.2.

Permeability

Figure 5.7 shows the α versus current density profile for baseline cell parameters, given in table A.2, except for variable aMPL permeability. This plot shows that a lower anode MPL permeability leads to a reduction in α, which is seen to be ~ 1 - 1.25 for a permeability 50% greater than the baseline value, and 0.025 - 0.04 for a permeability 25% below the baseline value in the range i = 150 – 200 mA cm^{-2}. Figure 5.8 shows that a lower aMPL permeability increases the saturation jump at the anode MPL and backing layer interface, thereby reducing the saturation level in the aMPL, leading to a greater resistance to liquid flow. A lower aMPL permeability also directly leads to a greater

resistance to liquid flow, giving a greater saturation gradient in the aMPL. Both of these effects lead to a lower saturation in the aMPL at the aCL interface, and ultimately a reduction in the aCL saturation and lower α, as described in section 5.1.

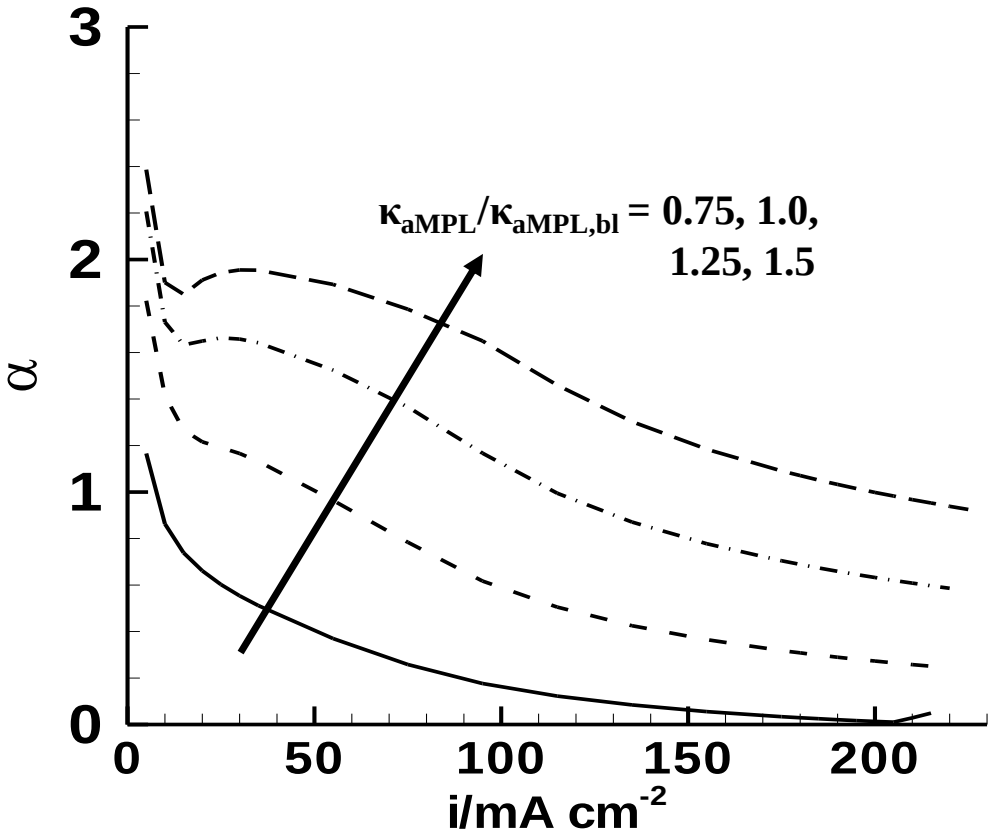

Figure 5.7. Net water transport coefficient (α) vs. cell current density for normalized anode micro-porous layer (aMPL) permeabilities of 0.75, 1.0, 1.25, and 1.5 with respect to the baseline value of 2.0×10^{-15} m^2. Cell properties and simulation parameters given in table A.2.

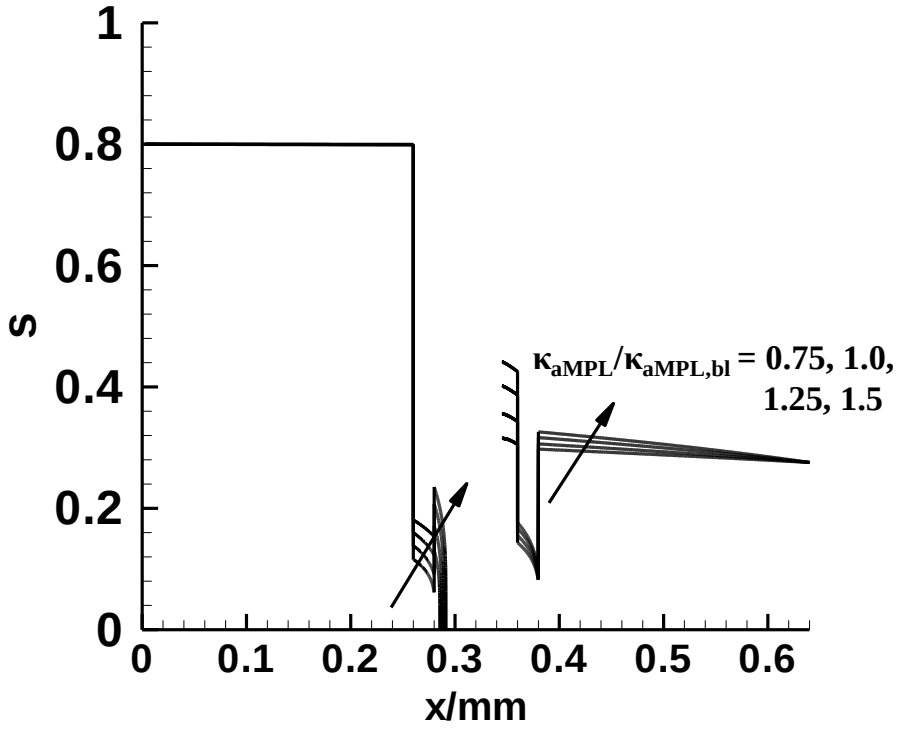

Figure 5.8. Liquid saturation profiles for normalized anode micro-porous layer (aMPL) permeabilities of 0.75, 1.0, 1.25, and 1.5 with respect to the baseline value of 2.0×10^{-15} m^2; i = 150 mA cm^{-2}. Cell properties and simulation parameters given in table A.2.

Thickness

Finally, figures 5.9 and 5.10 show the α versus current density and saturation profile plots for MEAs with baseline parameters given in table A.2, but with different aMPL thicknesses. From figure 5.9 we see that a thicker aMPL acts to reduce α, being ~ 0.4 - 0.52 for an aMPL thickness of 25% below the baseline value, and ~ 0.12 - 0.2 for an aMPL thickness 50% above the baseline value, again for i = 150 – 200 mA cm^{-2}. As shown in figure 5.10, the aMPL thickness obviously does not affect the saturation jump at the aBL/aMPL interface, but it does reduce the saturation level in the aCL simply due to the fact that it creates a longer distance over which the liquid must be transported, i.e. a greater resistance to liquid flow.

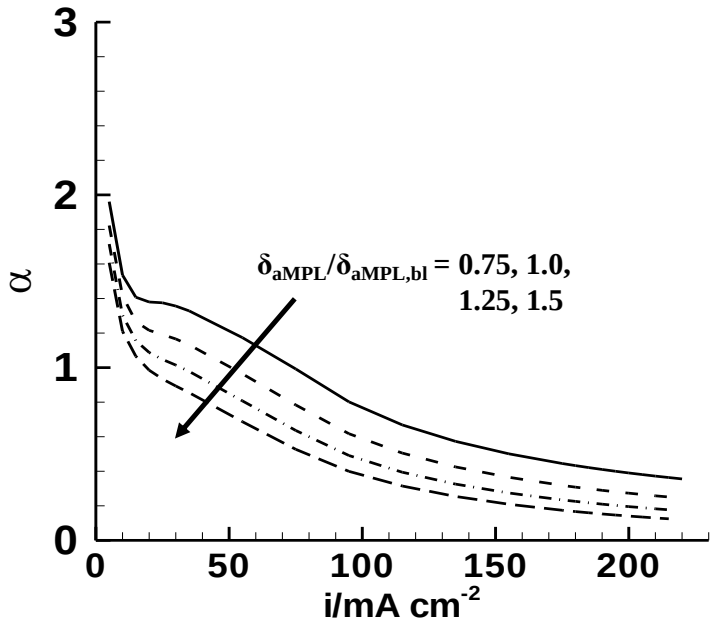

Figure 5.9. Net water transport coefficient (α) vs. cell current density for normalized anode micro-porous layer (aMPL) thicknesses of 0.75, 1.0, 1.25, and 1.5 with respect to a baseline thickness of δ_{aMPL} = 20μm. Cell properties and simulation parameters given in table A.2.

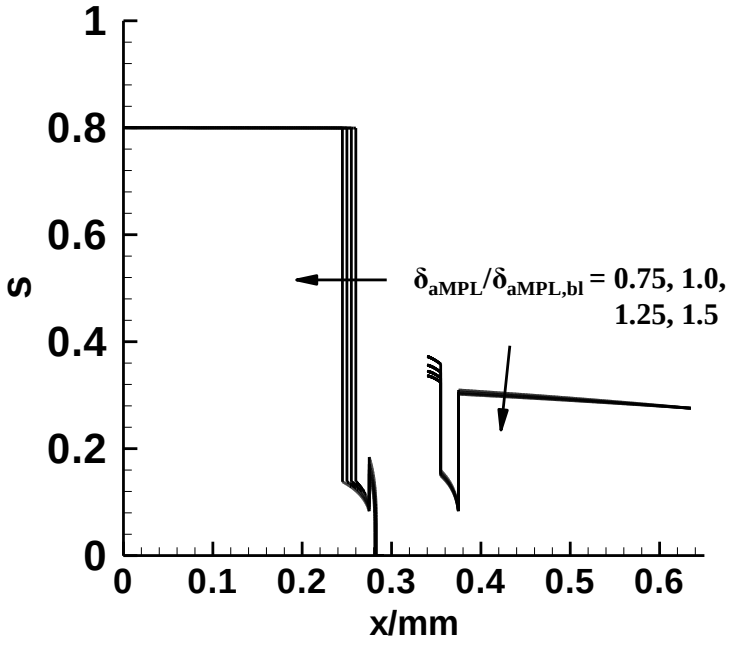

Figure 5.10. Liquid saturation profiles for normalized anode micro-porous layer (aMPL) thicknesses of 0.75, 1.0, 1.25, and 1.5 with respect to a baseline thickness of δ_{aMPL} = 20μm; i = 150 mA cm^{-2}; note that curves for 1.0, 1.25, and 1.5 have been shifted to align the membrane for all thicknesses. Cell properties and simulation parameters given in table A.2.

5.3 Anode and cathode MPL combination

Before concluding this chapter, we should briefly discuss how hydrophobic anode and cathode MPLs work together to most effectively reduce α. Note that all results presented thus far in this chapter are for MEAs with both anode and cathode MPLs.

Table 5.1 shows the simulated α and MCO values for four different MPL combinations at a typical operating current density of 200 mA cm^{-2} for the cell given in table A.1: no MPLs, cathode MPL only, anode MPL only, and anode and cathode MPLs. It is seen that the incorporation of a hydrophobic cathode MPL slightly reduces α (1.97 without MPLs to 1.52 with cathode MPL at 200 mA cm^{-2}), but the use of a hydrophobic anode MPL reduces α more drastically (1.97 without MPLs to 0.544 with anode MPL at 200 mA cm^{-2}). The use of both anode and cathode hydrophobic MPLs lowers α the greatest (1.97 without MPLs to 0.293 with both MPLs at 200 mA cm^{-2}). Further, note that the incorporation of hydrophobic anode and cathode MPLs also slightly reduces the MCO (on the order of 10%). These simulated results for MPL effects on both α and MCO are in qualitative agreement with experimental observations and the theory presented by several researchers [57,58,61,62,63,64,65].

Table 5.1. α and MCO values for four MPL combinations at 200 mA cm^{-2}; anode and cathode stoichiometries of 1.75 @ 150 mA cm^{-2} with 3 M fuel. Cell properties given in table A.1.

	α	**MCO**
No MPLs	1.97	0.345
Cathode MPL	1.52	0.327
Anode MPL	0.544	0.305
Two MPLs	0.293	0.294

The theory of how hydrophobic anode and cathode MPLs act together to reduce water crossover is elucidated by analyzing the liquid saturation profiles given in figure 5.11. In figure 5.11a, we see that the cathode MPL acts to increase the liquid saturation level in the cathode CL, thereby increasing the back diffusion of H_2O into the aCL. The hydrophobic cathode MPL leads to a higher liquid pressure at the cathode MPL/CL interface, and because the liquid pressure is uniform across the interface, a corresponding higher liquid saturation level in the cathode CL. Physically, there is a source of H_2O in the cathode CL, and this product water is trying to move to the cathode flow channel (positive x-direction). The hydrophobic nature of the cathode MPL helps to inhibit the flow of liquid water out of the cathode CL, which leads to the higher saturation in the cathode CL.

The effects of a hydrophobic aMPL alone on saturation profile are given in figure 5.11b; the combined effects of aMPL and cMPL on saturation profile are given in figure 5.11c. The physical explanation of why an aMPL is effective in reducing water crossover was already given in section 5.1. As noted in table 5.1, the inclusion of both aMPL and cMPL reduces α the most. This should come as no great surprise, due to the fact that an anode MPL and cathode MPL individually reduce α, and as illustrated in figure 5.11c, inclusion of two MPLs creates simultaneously a drier anode CL and a wetter cathode CL, leading to the greatest back-diffusion of H_2O, a reduced EOD of H_2O, and lowest α. We should mention that the presence of back diffusion of H_2O from cathode to anode - which is most significant with both anode and cathode MPLs present - is precisely the reason that a thin membrane is generally a necessity in low-α MEAs; the thinner the membrane, the greater the flux of H_2O back diffusion.

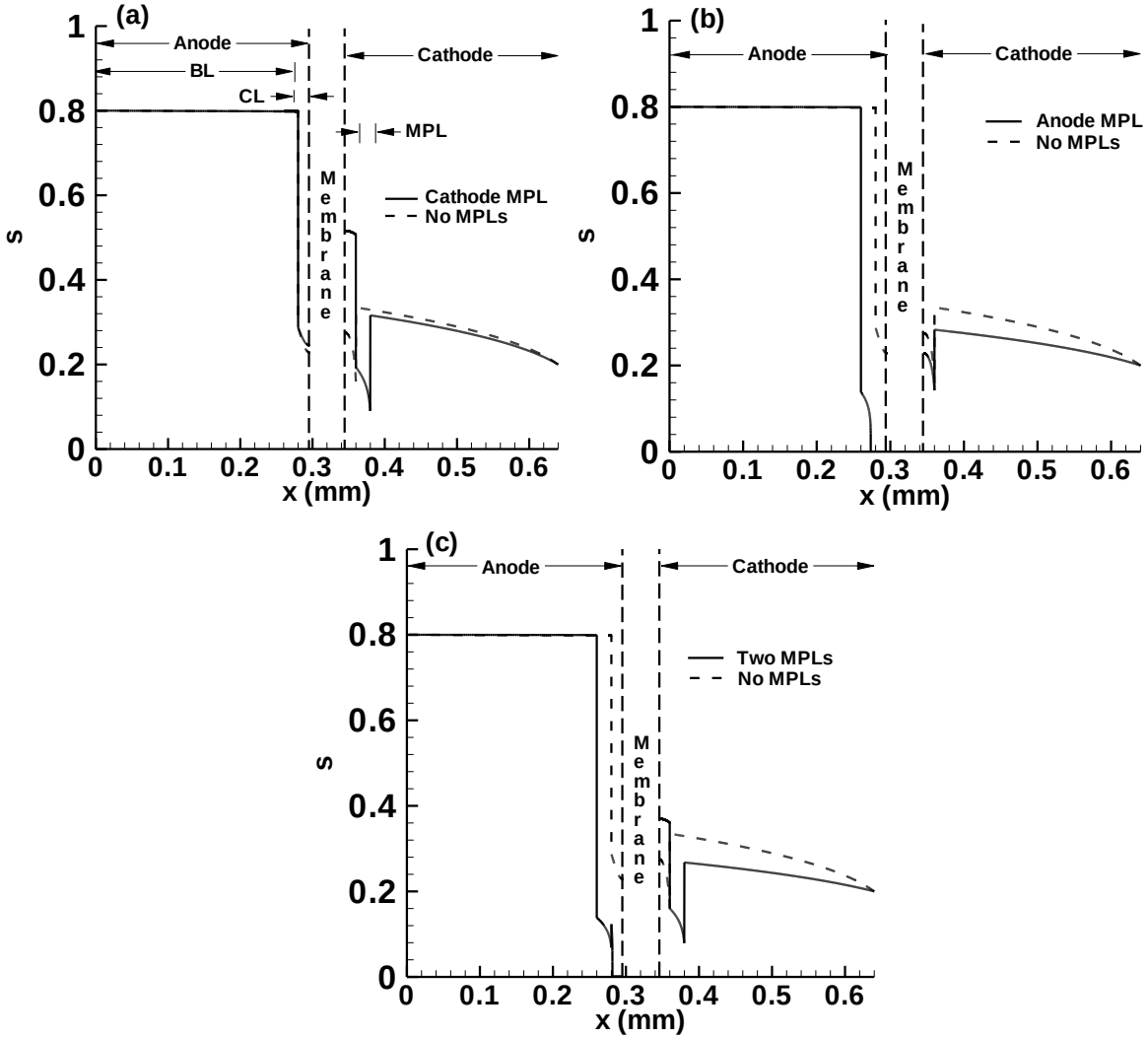

Figure 5.11. Liquid saturation profiles at i = 200 mA cm^{-2} for: (a) cathode MPL, (b) anode MPL, and (c) anode and cahtode MPLs. Note all hydrophobic MPLs with assumed properties given in Table A.1; anode and cathode stoichiometries of 1.75 @ 150 mA cm^{-2} with 3 M fuel; x = 0 is at the anode BL and channel interface.

Chapter 6. MEA Design and Theory for High Concentration Methanol Fuel Cells

In the previous chapter, we used fairly low concentration fuel and centered our efforts on reducing water crossover by the incorporation of a hydrophobic anode MPL. Because achieving a low α value is a critical prerequisite for using highly concentrated fuel, to date, the low-α literature has likewise generally centered on ways to first reduce α, while only using methanol fuel of about 2-3 M concentration. This is typically done in order to avoid additional complications associated with the use of highly concentrated fuel -- namely a high rate of methanol crossover and poor performance. In this chapter we extend the low-α MEA concept and present a novel MEA design with hydrophobic aMPL and additional anode transport barrier (aTB) between anode backing layer and aMPL. The primary role of the aMPL in this design is to minimize the amount of water that crosses through the membrane to the cathode; the primary role of the aTB is to act as an obstruction to methanol and water diffusion between the flow channel and the aCL. As such, the aMPL and aTB work in concert with one another to yield an MEA that realizes low α and low MCO while using concentrated methanol fuel.

In this chapter, our novel MEA design is described in detail, but more importantly, the physics of how such a design is successful is elucidated. Further, we perform a parametric study to investigate what aTB properties make a more effective aTB. Finally, to tie this work in with our overall goal of increasing the DMFC system energy density, we introduce a design method for determining the most efficient fuel concentration to carry in the system fuel tank for a high concentration methanol fuel cell (HC-MFC), based on the MEA to be used.

6.1 Roles of aTB and aMPL

Figure 6.1 illustrates the liquid methanol and H_2O concentration profiles at 175 mA cm^{-2} for the baseline cell given in table A.3, and the same cell without the aTB present. Here we see that in the anode transport barrier (0.26 mm < x < 0.52 mm) there is a large gradient in both liquid CH_3OH and H_2O concentrations. This implies that the anode transport barrier poses an obstruction to methanol diffusion from the flow channel towards the aCL and H_2O back-diffusion in the opposite direction. Thus, the aTB facilitates a water-rich aCL, thereby allowing us to use concentrated methanol fuel while still realizing a low MCO (i.e. high fuel efficiency). This point is illustrated in Figure 6.2, which shows the simulated MCO versus current density for the baseline cell and the same cell without the aTB; here, using 10 M fuel, we see that, roughly, MCO < 0.3 for i > 150 mA cm^{-2} with aTB present. Noting that the methanol EOD coefficient, n_d^{MeOH}, is an increasing function of methanol concentration, we see from equating equations (2.5), (2.6), and (3.11) that a lower aCL methanol concentration reduces both diffusion and EOD components of the methanol crossover.

As pointed out in chapter 4, due to the capillary-induced liquid flow in the porous media, there is a net transport of liquid from the anode flow channel towards the aCL; therefore the concentration gradients, as observed in figure 6.1, only imply the effect of the aTB on diffusive transport. Further, as illustrated in Figure 3.2, due to the binary nature of the CH_3OH/H_2O mixture, if the concentration of CH_3OH goes down, the concentration of H_2O must necessarily go up. This, of course means that any layer that acts as a barrier to methanol diffusion towards the aCL necessarily also acts as a barrier to H_2O diffusion towards the channel.

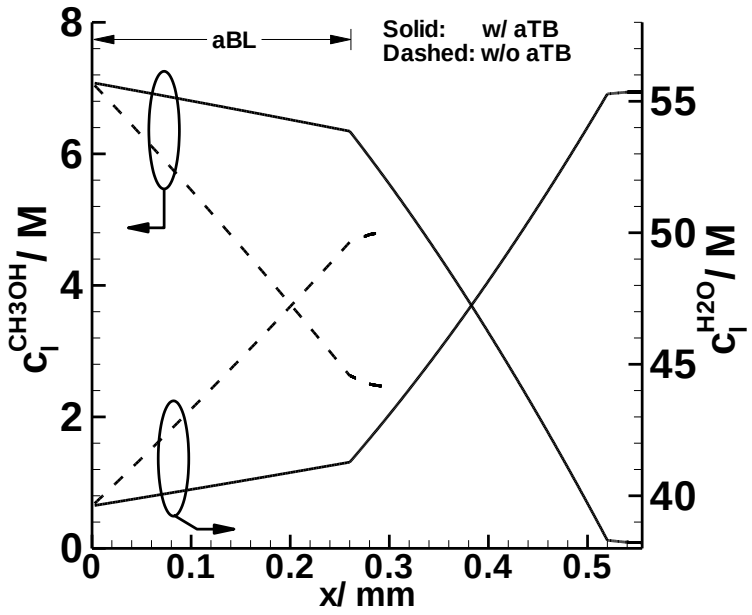

Figure 6.1. Liquid CH_3OH and H_2O concentration profiles with and without aTB; aMPL present. Note that without aTB present, the aMPL is at (0.26 mm < x < 0.28 mm) and the aCL is at (0.28 mm < x < 0.295 mm); i = 175 mA cm^{-2}; cell properties and simulation parameters given in table A.3.

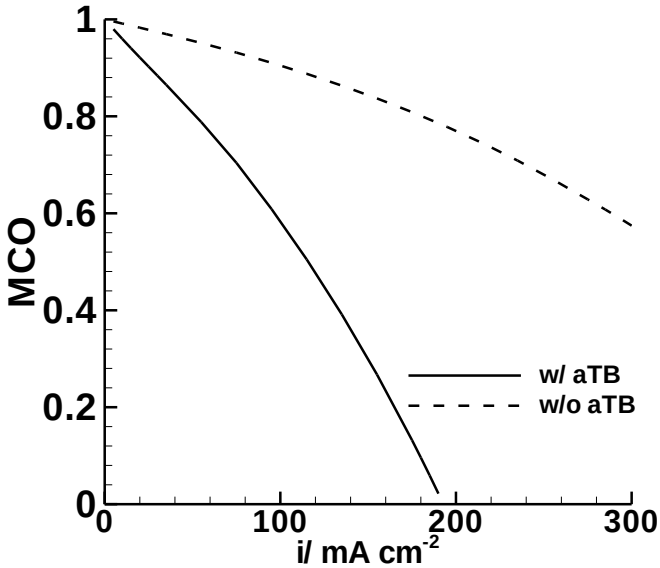

Figure 6.2. MCO vs. current density with and without aTB; aMPL present; cell properties and simulation parameters given in table A.3.

The liquid saturation profile for the baseline cell given in table A.3, at an operating current density of 175 mA cm^{-2}, is shown in figure 6.3. Note the high liquid saturation of s ~ 0.85 in the aTB region, as compared with s ~ 0.8 in the aBL. As we will

elucidate further in the next section, properties that create this high liquid saturation level coupled with a low porosity ($\varepsilon = 0.25$, as listed in table A.3) are what make the aTB an effective obstruction to diffusion. As illustrated by equations (3.15a) and (3.15b), a low porosity directly reduces the effective diffusivity in both the liquid and gas phases. A higher liquid saturation level increases the liquid phase effective diffusivity and decreases the gas phase effective diffusivity. Because species transport can take place in either the liquid or gas phases, this shift in effective diffusivities essentially increases the resistance to diffusion transport in the gas phase and reduces it in the liquid phase. Seeing how the molecular diffusivity in the liquid phase is ~ 10^{-9} $m^2 s^{-1}$ compared with ~ 10^{-5} $m^2 s^{-1}$ in the gas phase, the ultimate effect of the greater liquid saturation is a greater overall resistance to transport via diffusion.

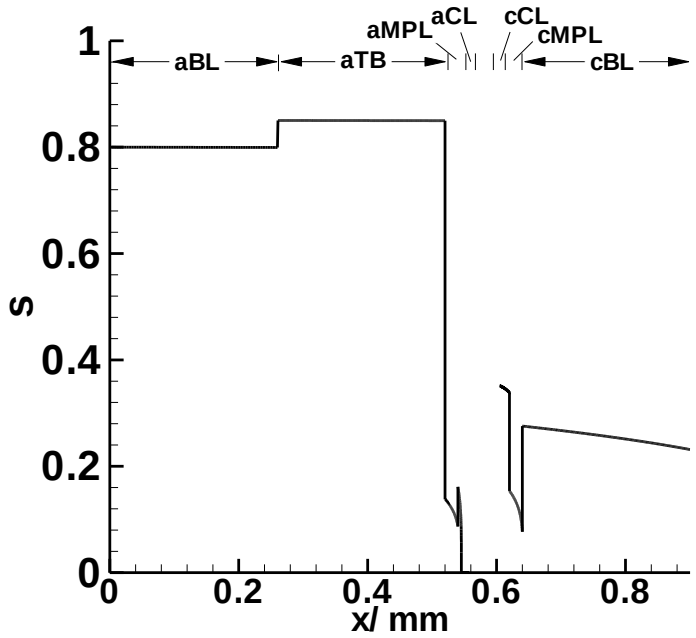

Figure 6.3. Anode and cathode liquid saturation profiles for baseline cell; i = 175 mA cm^{-2}; cell properties and simulation parameters given in table A.3.

While the aTB facilitates the use of high concentration methanol fuel by hindering CH_3OH and H_2O diffusion between the flow channel and the aCL, it does not directly

address the critical issue of membrane water transport and steady-state source of water supply into the aCL. As shown in figure 6.4, the inclusion of the aTB actually slightly *increases* α. This is most likely due to the corresponding drastic increase in MCO without the aTB, which leads greater H_2O production in the cCL and hence more back-diffusion of H_2O leading to slightly lower α. However, as we should expect from the physics revealed in the last chapter for an MEA without aTB, from figure 6.4, we see that the hydrophobic aMPL is clearly the primary reason for low α in the baseline cell with aTB (α ~ 0.35 with aMPL; α ~ 2.0 without aMPL at 175 mA cm^{-2}).

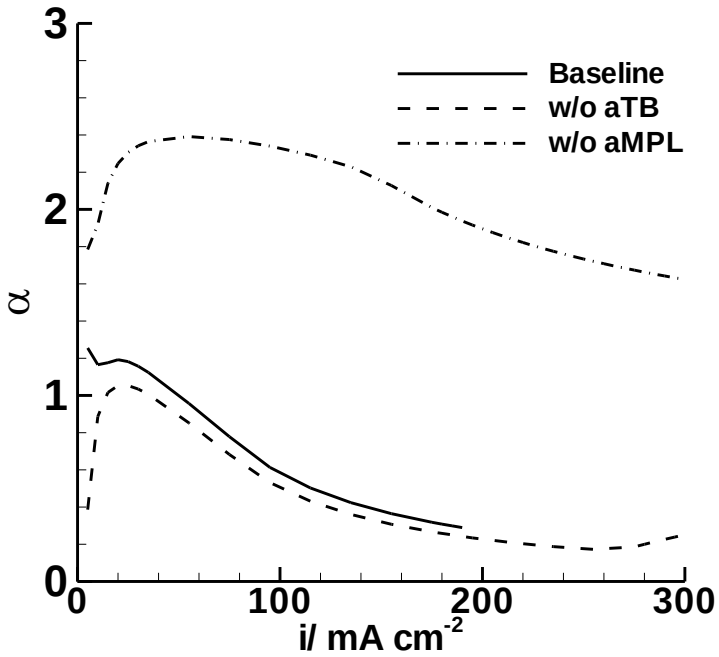

Figure 6.4. α vs. current density for baseline cell, baseline cell without aTB, and baseline cell without aMPL; cell properties and simulation parameters given in table A.3.

Analyzing figures 6.5 and 6.6, we see that in addition to simply reducing α, the aMPL also makes the aTB more effective. Figure 6.5 shows that the lower α realized by using an aMPL makes the aCL more water-rich, as the liquid H_2O concentration is higher, and the liquid methanol concentration is lower in the aCL with aMPL present. Note that without the aMPL present, the concentration profiles, particularly in the anode

transport barrier, have greater curvature. This is directly attributable to the greater α without aMPL, which physically means a greater capillary-induced liquid flow, and hence a greater transport of MeOH via convection (see equation (4.1)). Ultimately this greater convective transport of MeOH without anode MPL leads to a higher MeOH concentration in the anode CL, and as discussed previously, a higher rate of MeOH transport across the membrane by both EOD and diffusion. Figure 6.6 further highlights this point by showing that a significantly lower MCO is realized over the entire current density range with aMPL present (e.g. at i ~ 175 mA cm^{-2}, MCO ~ 0.15 with aMPL; MCO ~ 0.57 without aMPL).

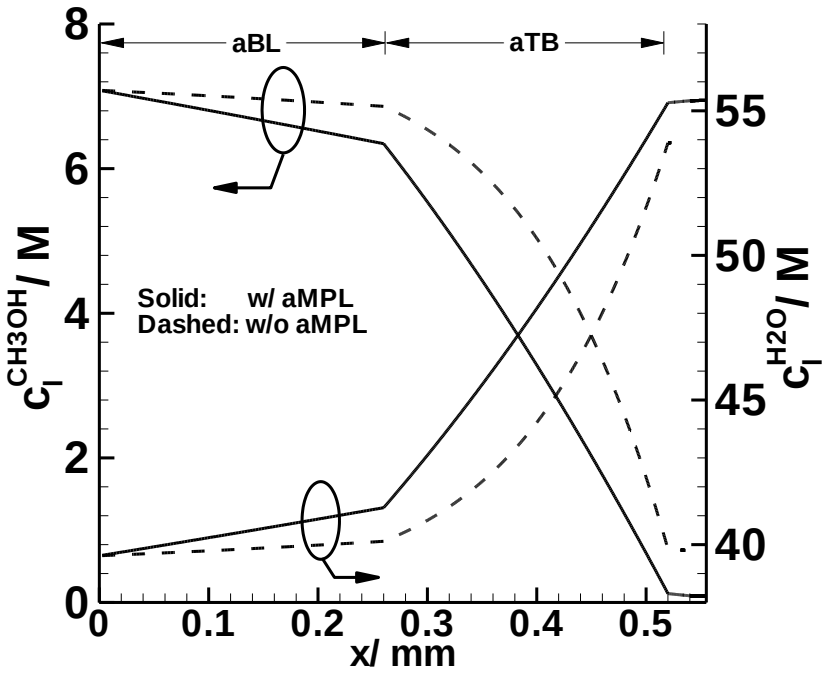

Figure 6.5. Liquid CH_3OH and H_2O concentration profiles with and without hydrophobic aMPL; aTB present; i = 175 mA cm^{-2}; cell properties and simulation parameters given in table A.3.

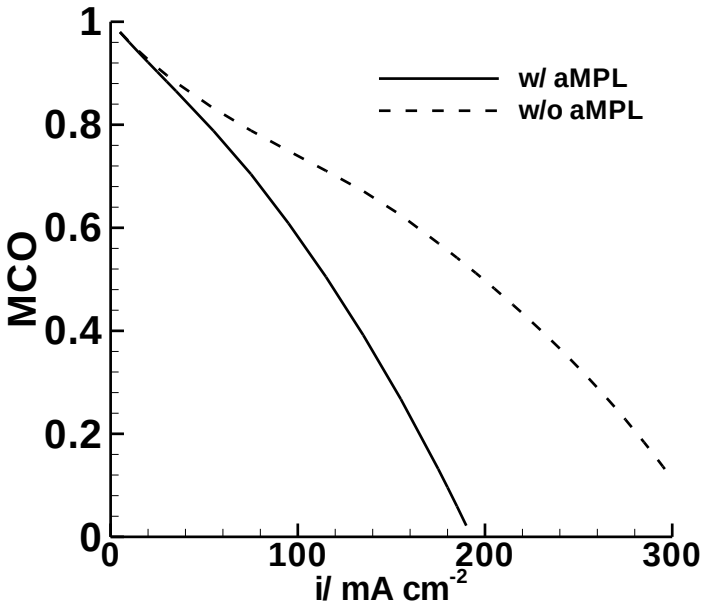

Figure 6.6. MCO vs. current density with and without hydrophobic aMPL; aTB present; cell properties and simulation parameters given in table A.3.

The underpinning concept to be take from figures 6.1 through 6.6 with regards to the direct use of concentrated methanol fuel is that the aTB and aMPL work *in conjunction* with one another. This is best summed up by the sketch given in figure 6.7, which highlights the aTB acting as a hindrance to diffusion of CH_3OH and H_2O between flow channel and aCL, while the aMPL essentially creates a source of water flowing into the aCL by reducing the amount of water crossing the membrane (low α). These two effects lead to a more water-rich aCL, and corresponding lower MCO.

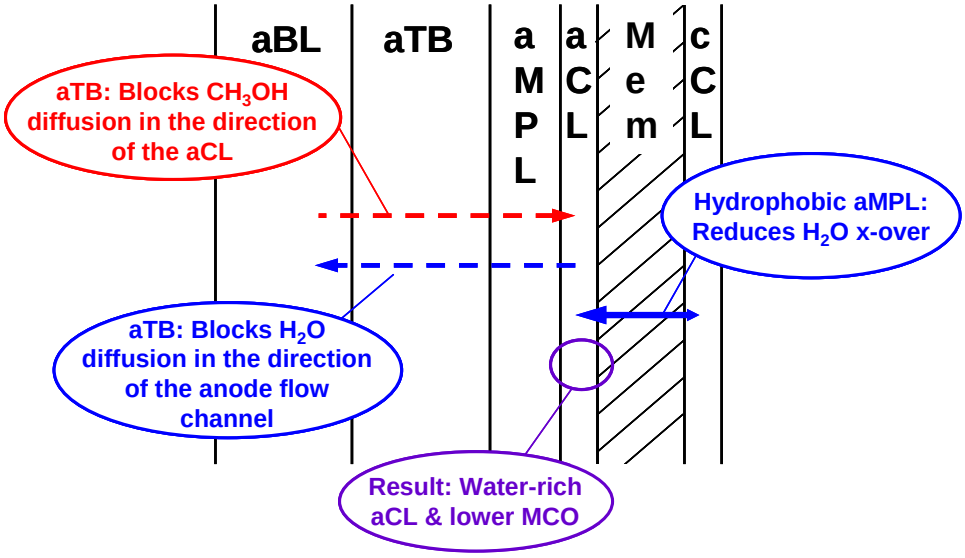

Figure 6.7. Schematic of how the aTB and aMPL work together to create water-rich aCL.

6.2 Effect of aTB properties on α and MCO

The effect of variable aTB contact angle is shown in figure 6.8. As illustrated in figure 6.8 (a), the main effect of an increasing aTB contact angle is to reduce the liquid saturation level within the aTB. However, as shown in figure 6.8 (b), this increasing hydrophobicity has a very minimal effect on α, as there is no discernable difference for various aTB contact angles at operating current density (~ 175 mA cm^{-2}). We have discussed at great length the fact that a hydrophobic aMPL reduces α. This naturally begs the question, "Why does an increasing aMPL contact angle significantly reduce α, while an increasing aTB contact angle has such little effect on α?" The answer has to do with the relatively high liquid saturation level of s ~ 0.5 in the aTB even with $\theta_{aTB} = 130^{o}$ (figure 6.8 (a)); when compared with an aMPL with the same contact angle, the aTB has higher liquid saturation level primarily due to differences in other assumed properties. With reference to equation (3.41), because the relative liquid-phase permeability, k_{rl}, is a strong increasing function of the liquid saturation, for the same flux in the liquid phase,

N_l, at lower values of s the gradient in liquid saturation will be much greater. Physically, the fact that s ~ 0.5 in the aTB with $\theta_{aTB} = 130^o$ means that there is only small resistance to liquid flow when compared with an MPL; hence, there is little drop in liquid saturation level over the aTB, correspondingly little effect on the saturation level in the aCL, and ultimately little effect on α.

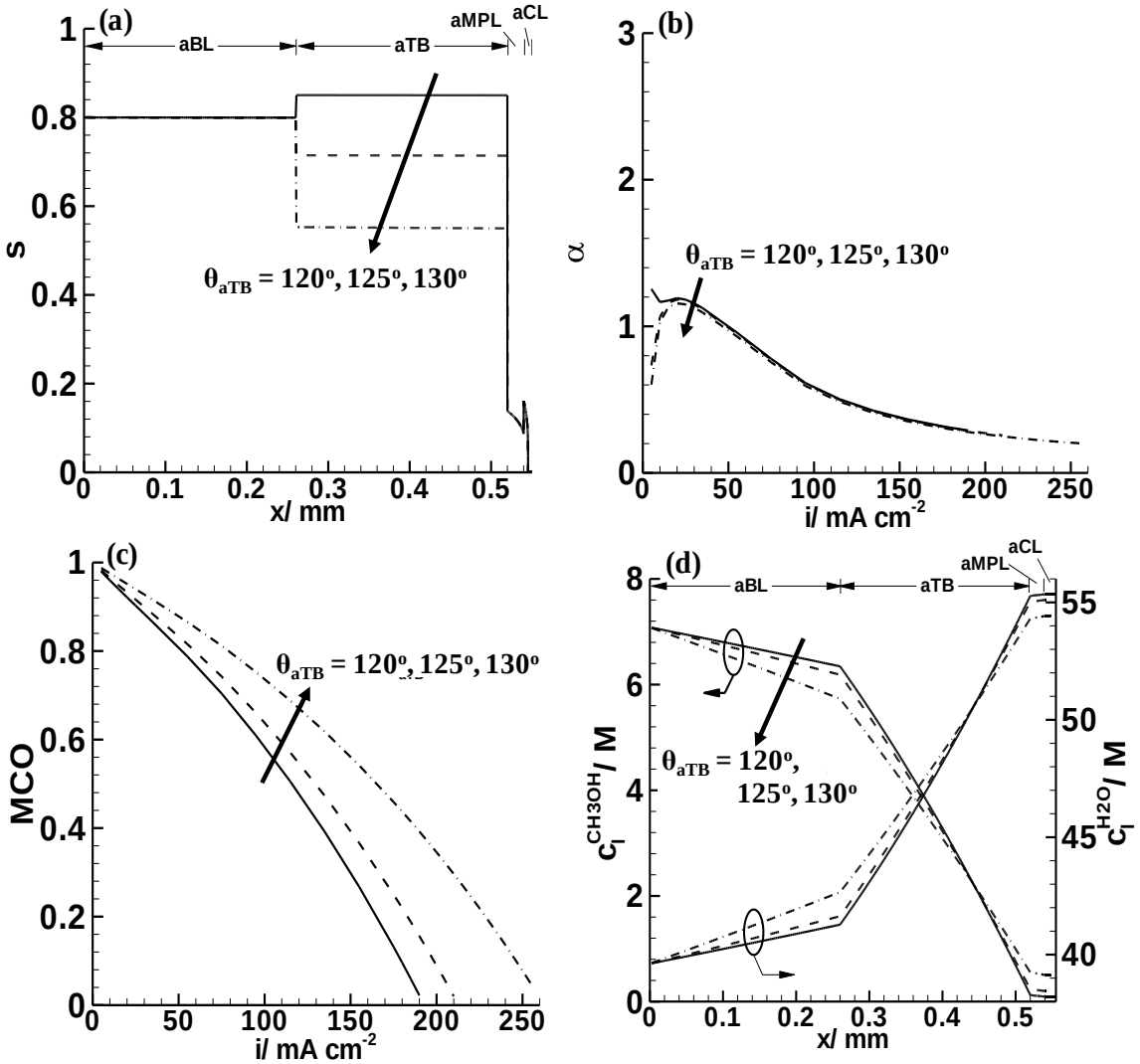

Figure 6.8. Effect of aTB contact angle: (a) anode liquid saturation profiles at i = 175 mA cm^{-2}, (b) α vs. current density, (c) MCO vs. current density, (d) liquid CH_3OH and H_2O concentration profiles at i = 175 mA cm^{-2}; cell properties and simulation parameters given in table A.3.

Figure 6.8 (c) illustrates that a higher aTB contact angle leads to a higher MCO. We see in figure 6.8(d) that this higher MCO with increasing contact angle is due to the aTB becoming a less effective barrier to methanol and H_2O diffusion. These results should come as no surprise in light of the contact angle effect on liquid saturation given in figure 6.8(a), and the physical explanation given previously of what makes an effective aTB. These results further imply that the most effective aTB may actually be hydrophilic, which would yield a layer with nearly 100% liquid saturation. Liu and Wang [62] noted that a hydrophilic aMPL (in an MEA without aTB), while causing a larger α, also reduced the limiting current density. This implies that the hydrophilic aMPL was a greater barrier to methanol diffusion toward the aCL and H_2O back-diffusion, which is exactly the goal of the aTB. The authors [62] attributed this increased transport resistance to the porosity of a hydrophilic aMPL being lower than that of a similar PTFE-treated hydrophobic aMPL as a result of the former's swelling as a consequence of its Nafion® treatment. We theorize from the results of this work, that the effectiveness of a hydrophilic anode layer (aMPL or aTB) in being a barrier to CH_3OH forward and H_2O back-diffusion is due not only to a lower porosity, but also simply to its hydrophilic nature, and corresponding high liquid saturation level.

The effect of variable aTB permeability is shown in figure 6.9. In figure 6.9 (a), we see that a larger aTB permeability leads to a higher liquid saturation level. Using the same logic as with the variable aTB contact angle, we see in figure 6.9 (b) that this greater liquid saturation level leads to a more effective barrier to methanol and H_2O diffusion, highlighted by the larger methanol and H_2O gradients in the aTB. The greater resistance of course yields the lower MCO with greater aTB permeability, as shown in

figure 6.9 (c). Finally, figure 6.9 (d) shows that a variable aTB permeability - at least in the range tested here - has little effect on α. By analyzing figure 6.9 (a) and thinking once again with reference to equation (3.41), this minimal effect on α can be attributed to the liquid saturation level remaining relatively high in the aTB.

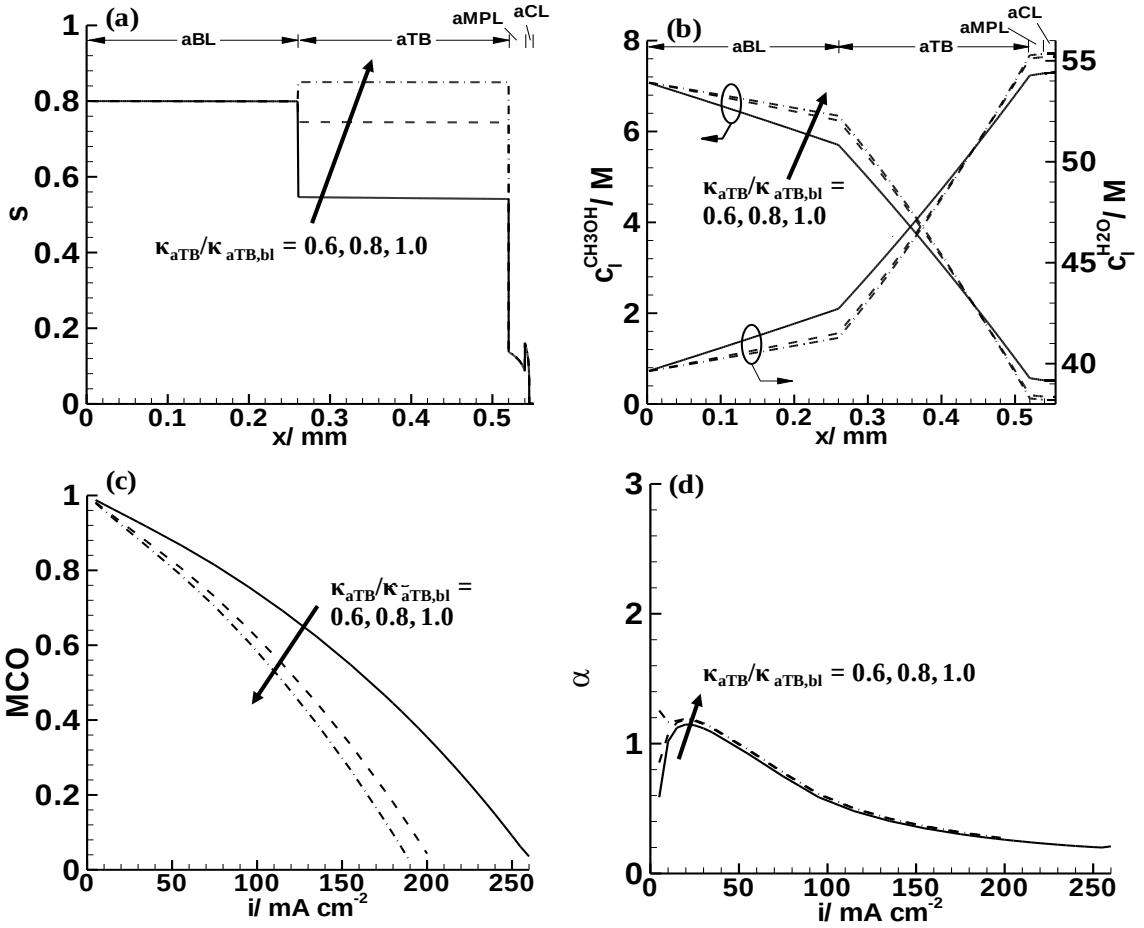

Figure 6.9. Effect of aTB permeability: (a) anode liquid saturation profiles at i = 175 mA cm^{-2}, (b) liquid CH_3OH and H_2O concentration profiles at i = 175 mA cm^{-2}, (c) MCO vs. current density, (d) α vs. current density; all permeability values normalized by the baseline value of 1.0x10^{-14}m^2; cell properties and simulation parameters given in table A.3.

Variable aTB thickness effect is illustrated in figure 6.10. It should come as no great surprise that a thicker aTB acts as a more effective barrier to methanol and H_2O diffusion, as highlighted in figure 6.10 (a). Naturally, this leads to a lower MCO with

thicker aTB, as highlighted in figure 6.10 (b). Finally, figure 6.10 (c) shows that the varying aTB thickness has no discernable effect on α. This again should be expected by analyzing the saturation level given in figure 6.3, which shows that for the aTB properties modeled (figure 6.10 has baseline cell properties, but with variable aTB thickness), the liquid saturation remains at the relatively high level of s ~ 0.85.

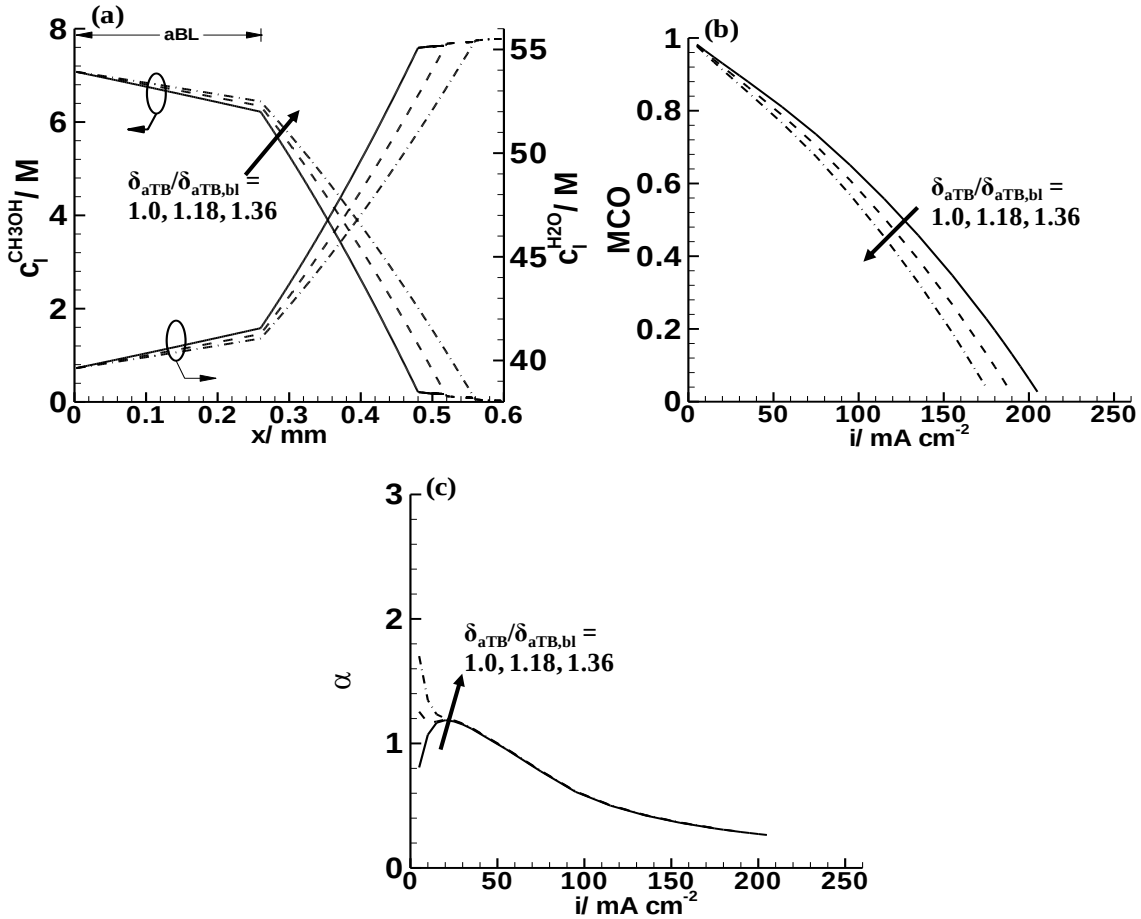

Figure 6.10. Effect of aTB thickness: (a) liquid CH_3OH and H_2O concentration profiles at i = 175 mA cm^{-2}, (b) MCO vs. current density, (c) α vs. current density; all thicknesses normalized by the baseline value of 260 μm; cell properties and simulation parameters given in table A.3.

6.3 Effect of aMPL properties on α and MCO

The parametric effect of aMPL contact angle, permeability, and thickness on α and MCO are summarized in figures 6.11 and 6.12, respectively. In figure 6.11 we see that an aMPL with greater contact angle. (i.e. more hydrophobic), smaller permeability, and greater thickness reduces α. It is further evident from figure 6.12 that these same parameters that reduce α also result in a slight reduction of MCO. As we expected, these parametric effects for the anode MPL properties are exactly as we saw in the previous chapter for an MEA without an aTB; we include figures 6.11 and 6.12 here simply to verify that the anode MPL properties have the same effects in an MEA that also includes an aTB.

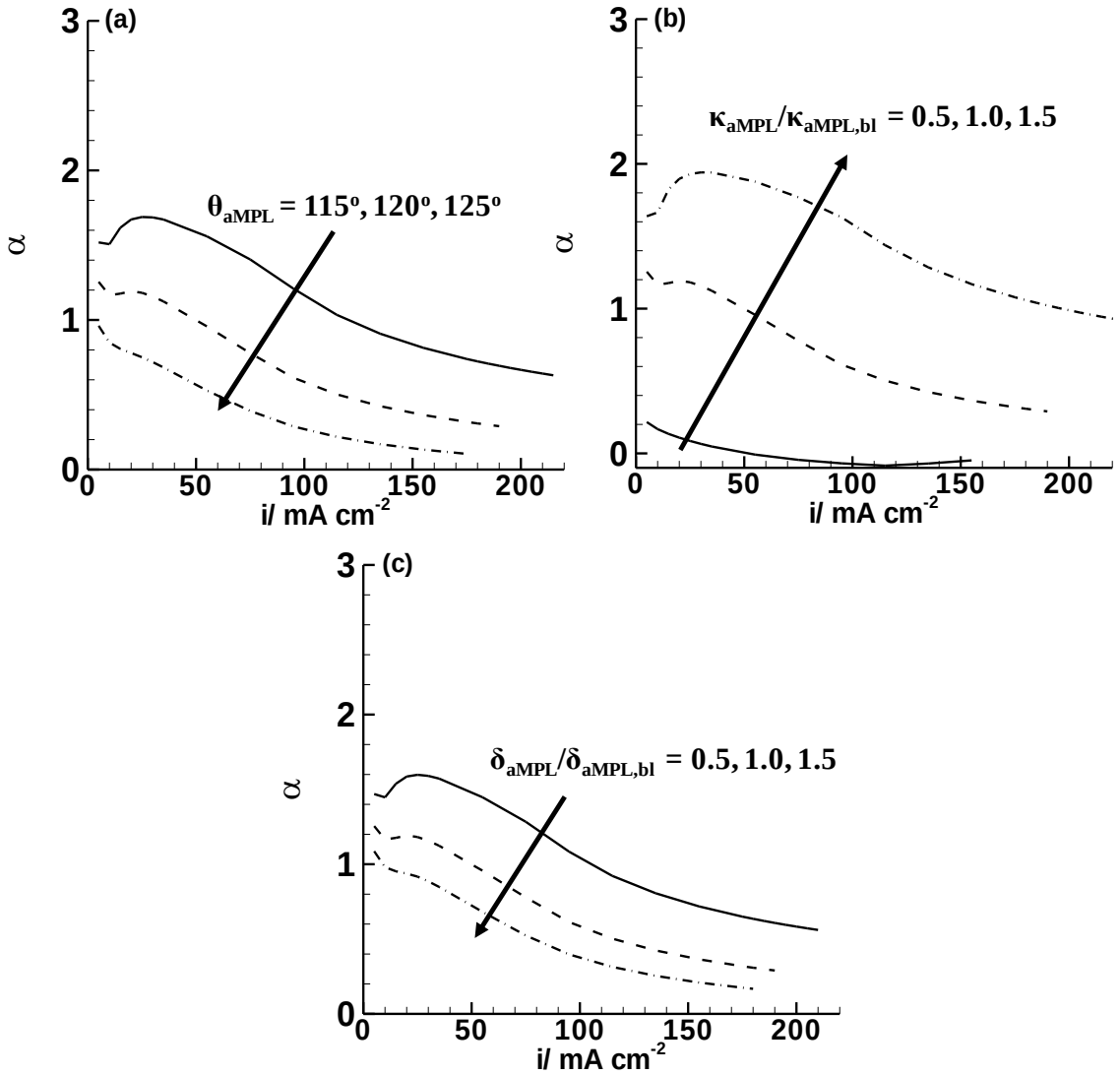

Figure 6.11. α vs. current density for various (a) aMPL contact angles, (b) aMPL permeabilities, and (c) aMPL thicknesses; cell properties and simulation parameters given in table A.3 (including baseline values used for normalization).

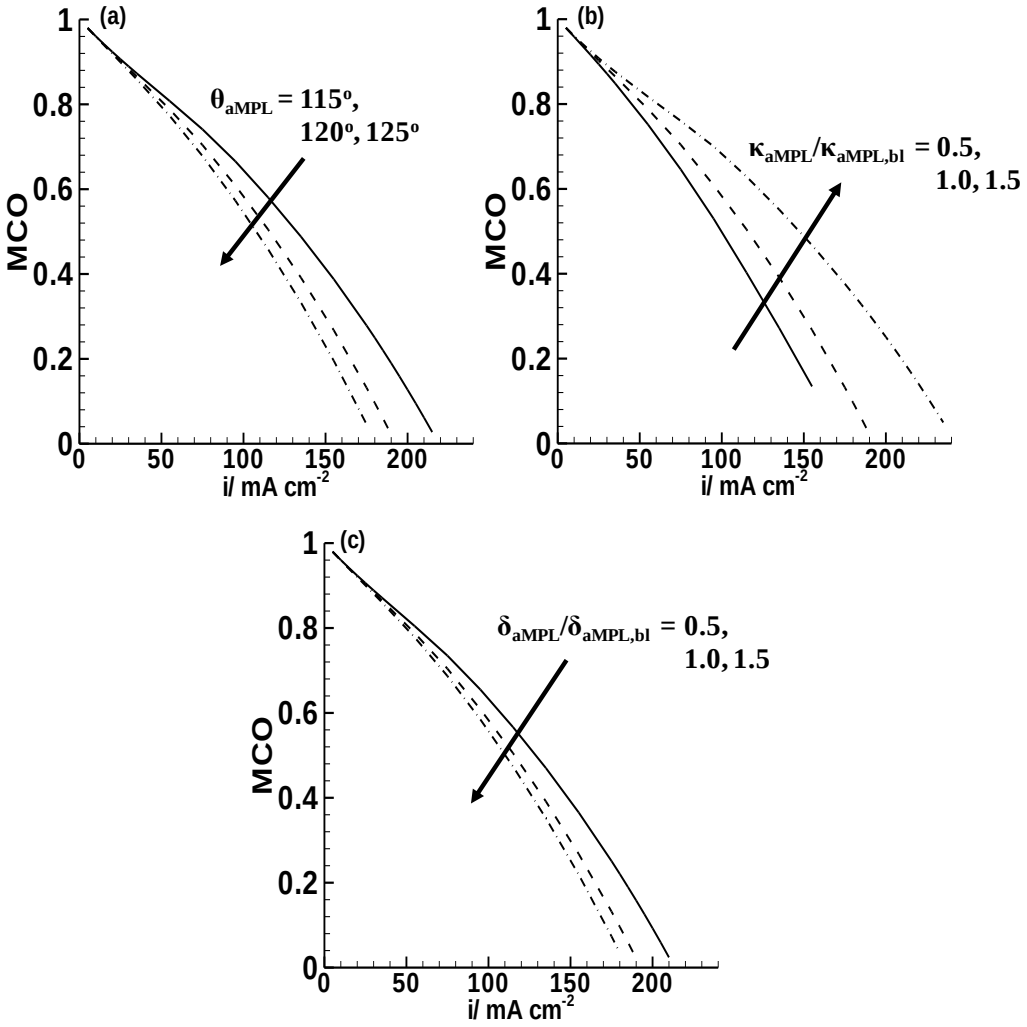

Figure 6.12.MCO vs. current density for various (a) aMPL contact angles, (b) aMPL permeabilities, and (c) aMPL thicknesses; cell properties and simulation parameters given in table A.3 (including baseline values used for normalization).

6.4 Determining most efficient fuel concentration for HC-MFC

With our aTB MEA designed for a HC-MFC, in this section we turn our attention to determining the most efficient fuel concentration to carry in the fuel tank as part of a DMFC system design; this type of procedure could be carried out by a design engineer. By "most efficient" here, we mean the most efficient use of system volume, weight, etc., as the goal is to minimize or eliminate the need to carry excess H_2O or CH_3OH in the system, all while utilizing only internal water management. We will assume that our

MEA is designed with baseline aTB, and baseline aMPL properties as given in table A.3, but with a thickness of 30 μm in effort to reduce α. A typical operating condition for a DMFC is at a current density of ~ 80-90% of the limiting current density (i.e. just before the mass transport limiting region); this operating point typically yields a reasonable tradeoff between good performance (voltage or power), and high fuel efficiency (low MCO). At this operating point, MCO is typically ~ 0.2 for a well-designed MEA, so we will use MCO = 0.2 in this example as our design point criteria.

The MCO = 0.2 curve in figure 1.9 will serve as the guide for choosing a fuel concentration which yields optimal use of our system volume, for a DMFC utilizing the prescribed MEA. This process is iterative, as we do not know what α value the simulated MEA will yield *a priori*, and because α is also a function of the fuel concentration used. However, as α is primarily determined by aMPL properties, from figure 6.11, we can hypothesize that this MEA will yield α ~ 0.2. Looking at the MCO = 0.2 curve at α ~ 0.2 in figure 1.9, we find a corresponding fuel concentration of ~ 14 M, which is the value that we will choose for our first simulation. Table 6.1 shows the results of this simulation at MCO = 0.2, listed as iteration 1. We see from this data that the actual α value corresponding to 14 M fuel is α = 0.137, meaning that our initial guess was fairly accurate. Turning our attention once again to figure 1.9, we see that α = 0.137, the optimal fuel concentration is actually closer to 14.5 M, and we therefore make a second simulation at this value. Table 6.1 illustrates that for c_o^{CH3OH} = 14.5 M, α = 0.131 for MCO = 0.2; for our purposes, this is clearly accurate enough, as the c_o^{CH3OH} = 14.5 M, α = 0.131 point essentially lies on the MCO = 0.2 curve in figure 1.9. This means that the proposed MEA design will allow us to directly use ~ 14.5 M fuel in an energy dense

DMFC system, while operating at a fuel efficiency of ~ 80%, without any external means of water recovery.

Table 6.1. Iterations for determining the most efficient fuel concentration for MEA with baseline aTB and baseline aMPL in table A.3 but with 30 μm thickness.

Iteration	**Fuel Concentration, c_o^{CH3OH} / M**	**Simulated i @ MCO = 0.2 / mA cm^{-2}**	**Simulated α @ MCO = 0.2**
1	14	201.75	0.137
2	14.5	206.75	0.131

Chapter 7. Performance-Based Figure-of-Merit for DMFC Membranes

In the membrane community, a commonly used figure of merit (FOM) for evaluating DMFC membranes is the membrane's selectivity, defined as the ratio of H^+ conductivity to methanol permeability [46,47,88,89,90,91]. The idea behind this FOM is clear: qualitatively we would like to have lower methanol permeability to reduce methanol crossover from the anode to cathode, and we would like to keep the H^+ conductivity as high as possible so as not to induce a large ohmic loss from the membrane. However, a key question remains: how appropriate is the membrane selectivity, defined by a linear relation between proton conductivity and methanol permeability, in accurately depicting overall membrane performance in a DMFC at common operating conditions?

In the traditional DMFC membrane electrode assembly [46,47,88,89,90,91], the membrane plays the critical role in methanol crossover reduction, as high concentration fuel is ideally introduced directly into the anode flow channel. However, as described in chapters 4 through 6, a burgeoning area of research pertaining to DMFCs is advanced MEA designs developed for simultaneous water and fuel management. Again, these advanced MEA designs have two goals: facile water transport from the cathode to anode, and reduction of methanol concentration in the anode catalyst layer at operating conditions in effort to reduce MCO due to both diffusion and electro-osmotic drag [48,56,57,58,59,61,62,64,65,81]. Additionally, as discussed in chapter 1, there have been many designs developed with the intent of reducing the methanol concentration prior to

its entrance into the anode diffusion media ("upstream MCO mitigation"), [49,50,51,52,53] such as fuel circulation loops and fuel/water mixing chambers. For both the advanced MEA and upstream MCO mitigation concepts, the membrane plays a less critical role in reducing MCO.

In this chapter our primary goal is to systematically study the performance of a DMFC with traditional MEA under common operating conditions and determine whether or not the traditionally used selectivity is the best indicator of performance. Our second goal is to study the performance of two nontraditional DMFCs. The first nontraditional DMFC incorporates the low-α MEA described in chapter 5, and the operating conditions specified mimic a DMFC system design with upstream MCO mitigation. The second nontraditional DMFC uses the advanced low-α MEA design described in chapter 6, which incorporates an anode transport barrier in order to help mitigate MCO. Once again, with these two nontraditional designs we determine a proper performance-based FOM and compare this FOM with the one determined for the traditional DMFC design.

In effort to develop a quantitative performance-based FOM for the membrane, we define the following generic relationship:

$$FOM \equiv \frac{\left[\kappa^{H^+} \Big/ \kappa_{bl}^{H^+} \right]^q}{\left[\mathbb{P}_{Mem}^{MeOH} \Big/ \mathbb{P}_{Mem,bl}^{MeOH} \right]} \tag{7.1}$$

where κ_{bl}^{H+} = baseline ionic conductivity (S m^{-1})

$\mathbb{P}_{Mem,bl}^{MeOH}$ = baseline membrane MeOH permeability (m^2 s^{-1})

The idea here is simple. First, note here that q = 1 gives the FOM as a non-dimensional form of selectivity. We know parametrically that greater membrane ionic conductivity

and lower membrane methanol permeability are advantageous; the goal here is to determine the proper proportionality of these two membrane properties, i.e. the value of q in equation (7.1). Note a greater value of q indicates that, relative to one another, κ^{H^+} is more important, and $\mathbb{P}_{Mem}^{MeOH}$ is less important in predicting DMFC performance.

If we plot the cell potential versus the FOM for different values of q, the value of q which yields the most accurate FOM for membrane performance will best reduce the data onto a clearly-defined trend line. This is precisely the approach that we take in the next three sub-sections for the three MEAs mentioned. For each MEA we plot the cell potential versus FOM for 30 data points generated with our DMFC model for varying values of $\left[\kappa^{H^+} \Big/ \kappa_{bl}^{H^+}\right]$ and $\left[\mathbb{P}_{Mem}^{MeOH} \Big/ \mathbb{P}_{Mem,bl}^{MeOH}\right]$. As it is physically difficult to alter a membrane's methanol permeability without simultaneously affecting its water diffusivity, we simulate two cases for each MEA type: first we change $\mathbb{P}_{Mem}^{MeOH}$ while keeping D_{Mem}^{H2O} constant, and second we change $\mathbb{P}_{Mem}^{MeOH}$ while keeping the ratio $\mathbb{P}_{Mem}^{MeOH}/D_{Mem}^{H2O}$ constant.

7.1 Traditional MEA

The relevant properties of the traditional MEA are listed in table A.4. The thick membrane (175 μm) and no MPLs are both common characteristics of a traditional MEA. Note in table A.4 that we introduce 10 M fuel into the anode flow channel. Figures 7.1 and 7.2 give plots of the cell voltage at an operating current density of 150 mA cm^{-2} versus figure of merit for (a) q = 1, (b) q = 2, (c) q = 3, and (d) q = 4. In figure 7.1 we

assume a constant D_{Mem}^{H2O} while changing $\mathbb{P}_{Mem}^{MeOH}$ for different FOM, and in figure 7.2 we keep the ratio $\mathbb{P}_{Mem}^{MeOH}/D_{Mem}^{H2O}$ constant over all values of $\mathbb{P}_{Mem}^{MeOH}$.

The deviation from trend lines at high FOM values are for the data points with the highest value of κ^{H+} and the lowest value of $\mathbb{P}_{Mem}^{MeOH}$ in our data set. This deviation can be explained by a diminishing rate of return after increasing κ^{H+} and/or decreasing $\mathbb{P}_{Mem}^{MeOH}$ past a certain level. As illustrated by equations (1.21) and (3.44), increasing membrane conductivity past the point where the ohmic overpotential is no longer a significant portion of the overall voltage loss, has very little effect on the cell voltage. Likewise, decreasing $\mathbb{P}_{Mem}^{MeOH}$ past the point where methanol diffusion across the membrane has essentially been eliminated, has very little consequence on the cell voltage. Based on this physical explanation, we assume that these three data points fall outside the range of applicability for our FOM, denote them with an open diamond in figures 7.1 and 7.2, and do not include them in our data correlation (i.e. calculation of our coefficient of determination, R^2).

We should mention that even if methanol permeation across the membrane is eliminated, there is still transport via electro-osmotic drag, and corresponding cathode performance loss. This point is emphasized by looking at equations (2.5), (2.6), and (3.11) for membrane MeOH crossover. Note in these simulations that we have assumed the methanol EOD coefficient is proportional to the methanol concentration in the anode catalyst layer, and that the EOD coefficient is unaffected by the various values of $\mathbb{P}_{Mem}^{MeOH}$ assumed for changing FOM.

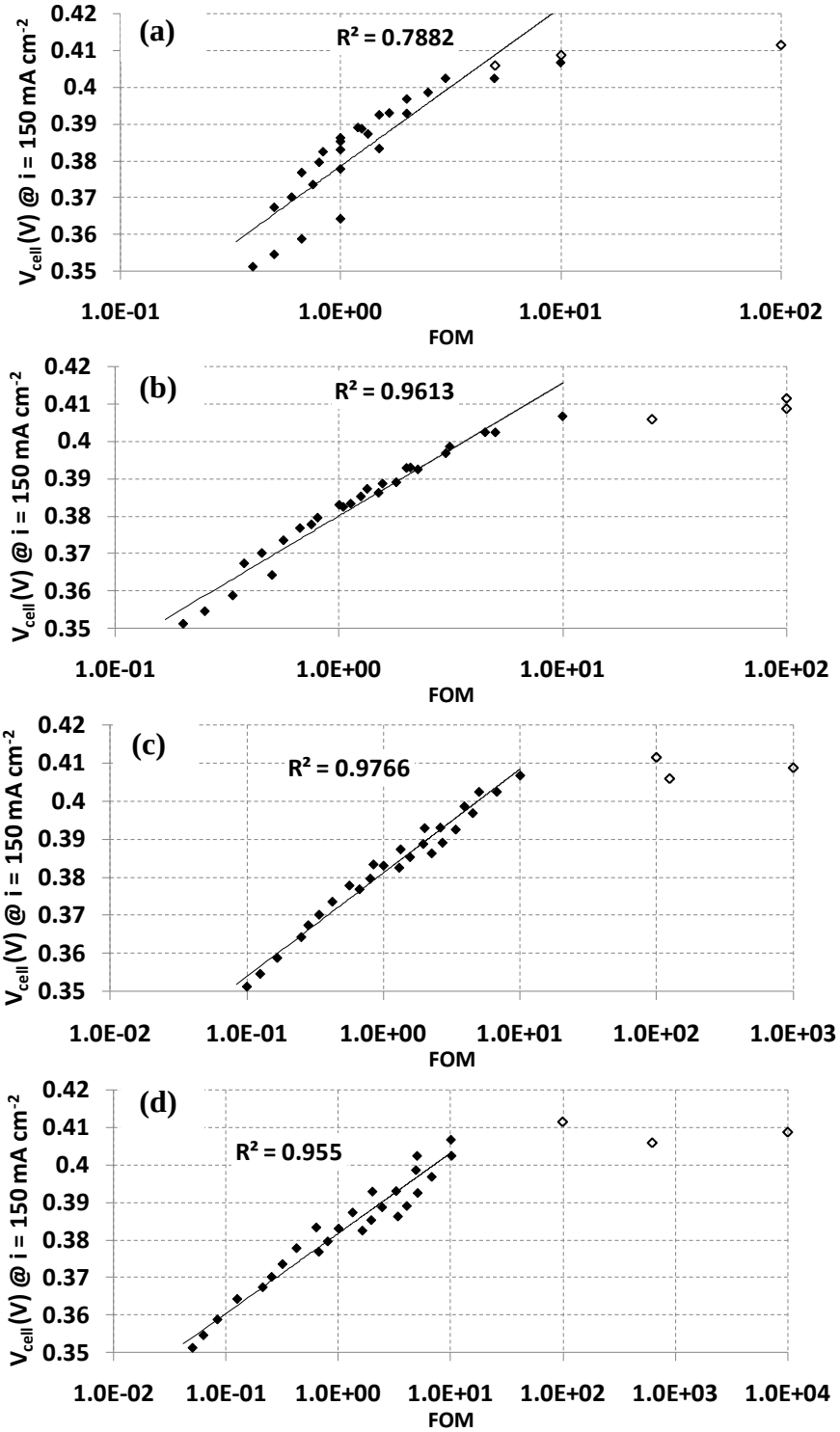

Figure 7.1. Traditional MEA; a) q = 1, b) q = 2, c) q = 3, d) q = 4; D_{Mem}^{H2O} is held constant; hollow diamonds are considered outliers; cell properties and simulation parameters given in table A.4.

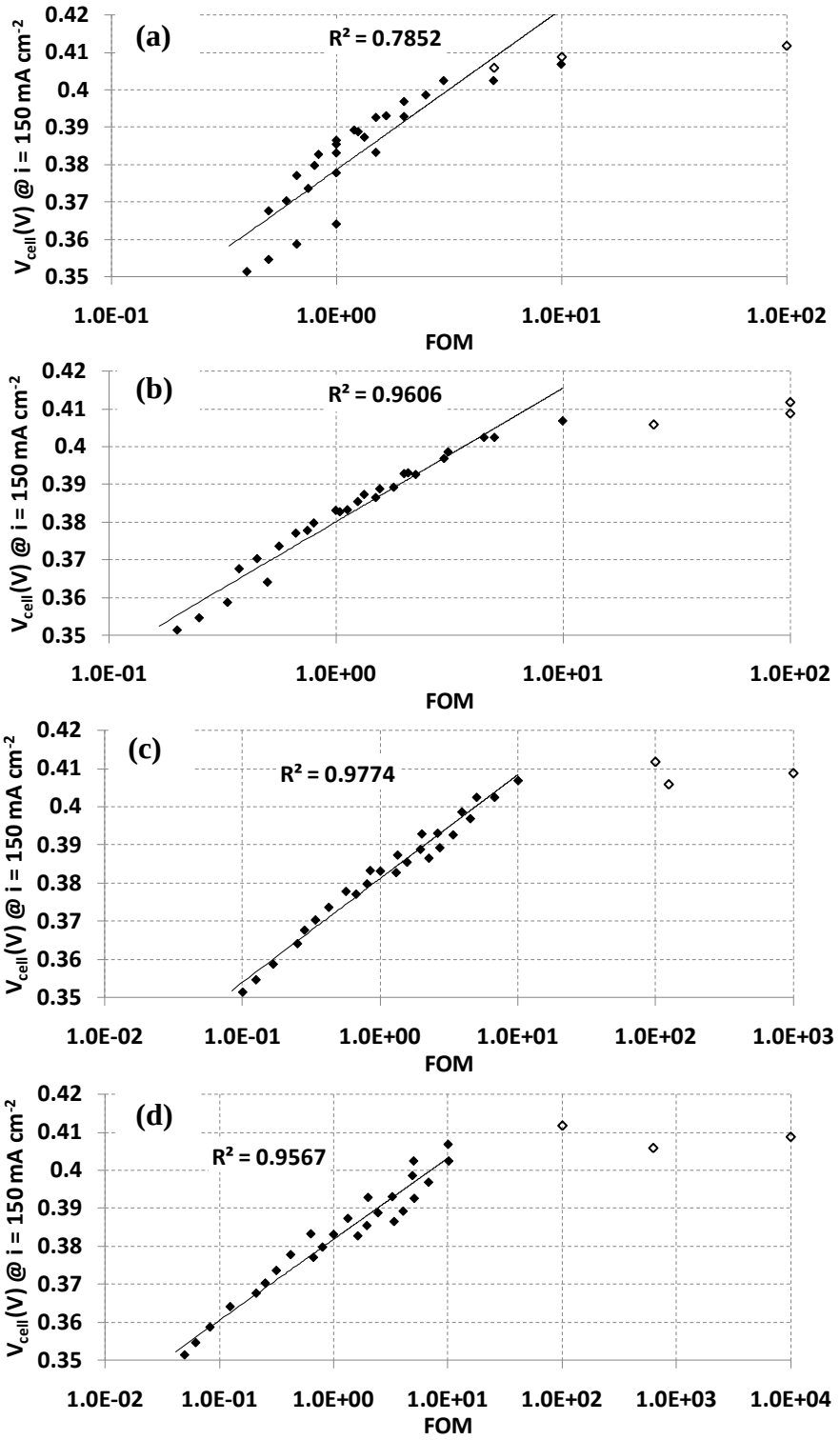

Figure 7.2. Traditional MEA; a) q = 1, b) q = 2, c) q = 3, e) q = 4; ($\mathbb{P}_{Mem}^{MeOH}$ /D_{Mem}^{H2O}) is held constant; hollow diamonds are considered outliers; cell properties and simulation parameters given in table A.4.

The most accurate performance-based FOM is given by the value of the exponent q, for which the cell potential most readily reduces along a clearly-defined trend line. This being the case, we can plot the coefficients of determination, R^2, from the cell potential versus FOM plots (figures 7.1 and 7.2) versus the value of q, and the value of q which yields the highest R^2 value will indicate the most accurate performance-based figure of merit. This is exactly the plot given in figure 7.3 for the traditional MEA, for both D_{Mem}^{H2O} held constant and $\mathbb{P}_{Mem}^{MeOH}/D_{Mem}^{H2O}$ held constant. We see from figure 7.3, that for both of these cases, an exponent of q ~ 2.75 yields the most accurate FOM.

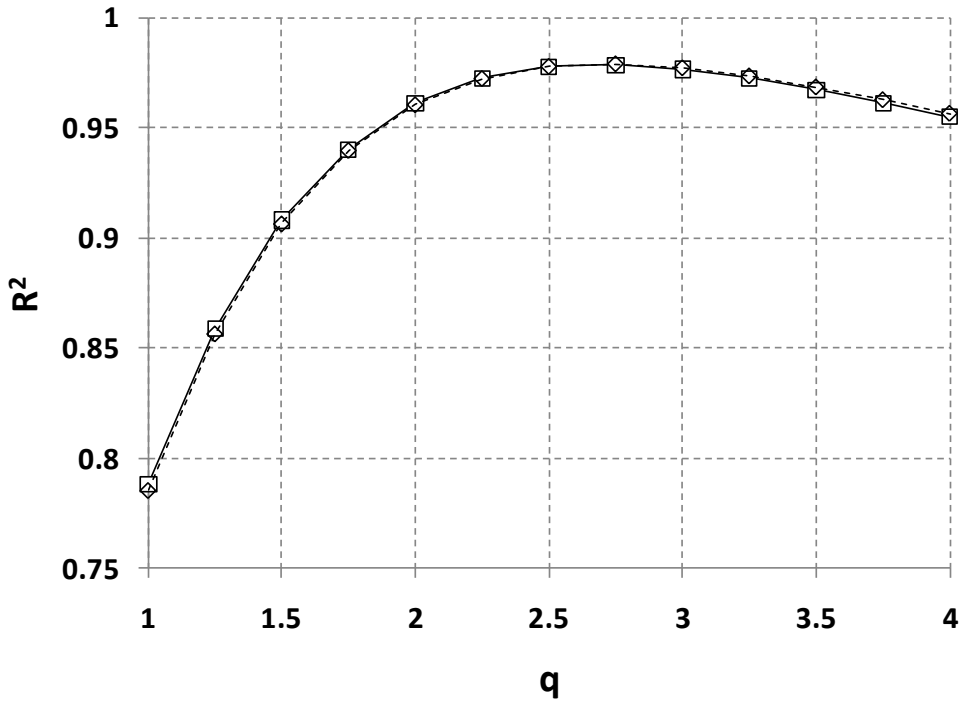

Figure 7.3. Coefficient of determination for different exponents of membrane conductivity, as per equation (7.1); traditional MEA; solid line with square is for D_{Mem}^{H2O} = constant, diamond with dashed line is for ($\mathbb{P}_{Mem}^{MeOH}/D_{Mem}^{H2O}$) = constant.

For the traditional MEA, it is not surprising that optimal value of q is essentially the same for D_{Mem}^{H2O} held constant and $\mathbb{P}_{Mem}^{MeOH}/D_{Mem}^{H2O}$ held constant. As we discussed in section 5.3, and as specifically illustrated in figure 5.11, without hydrophobic anode

and cathode micro-porous layers, there is very little back-diffusion of water from cathode to anode. Additionally, the thick membrane in the traditional MEA even further makes it difficult to create a back diffusion of water from cathode to anode. This being the case, whether we keep D_{Mem}^{H2O} constant while changing $\mathbb{P}_{Mem}^{MeOH}$ or change D_{Mem}^{H2O} proportionally with $\mathbb{P}_{Mem}^{MeOH}$ is somewhat irrelevant, because the net water flux across the membrane is nearly unaffected. This point is further highlighted by looking at table 7.1, where we show the diffusion component of α, α, and the membrane water diffusion flux as a fraction of the sum of the absolute value of the membrane water flux components, for the baseline κ^{H+}, and three values of $\mathbb{P}_{Mem}^{MeOH}$ and D_{Mem}^{H2O} (because in table 7.1 $\mathbb{P}_{Mem}^{MeOH}/D_{Mem}^{H2O}$ is held constant). Here we see that for the traditional MEA, the diffusion component of the water crossover is on the order of only 5% of the total H_2O crossover by all three mechanisms (diffusion, hydraulic permeation, and EOD); hence, the value of D_{Mem}^{H2O} has a minimal impact on membrane water crossover, and cell performance.

Table 7.1. Water crossover data for three data points for the traditional MEA with $\mathbb{P}_{Mem}^{MeOH}/D_{Mem}^{H2O}$ held constant; i = 150 mAcm^{-2}; cell properties and simulation parameters given in table A.4.

$\left[\kappa^{H^+}/\kappa_{bl}^{H^+}\right]$	$\left[\mathbb{P}_{Mem}^{MeOH}/\mathbb{P}_{Mem,bl}^{MeOH}\right]$	$\boldsymbol{\alpha_{diff}}$	$\boldsymbol{\alpha}$	$\frac{\left\|N_{diff}^{H_2O}\right\|}{\left\|N_{EOD}^{H_2O}\right\|+\left\|N_{diff}^{H_2O}\right\|+\left\|N_{HP}^{H_2O}\right\|}$
1.0	0.5	-0.059	2.136	1.34x10^{-2}
1.0	1.0	-0.1083	2.150	4.57x10^{-2}
1.0	1.5	-0.1505	2.154	6.12x10^{-2}

7.2 Low-α MEA with upstream MCO mitigation

The details of the low-α MEA are given in table A.2. Note that hydrophobic anode and cathode MPLs, along with the thin 50 μm membrane are typical low-α MEA characteristics, and are necessary particularly to obtain proper water balance. Further

note that in this simulation, we use only 2 M methanol fuel at the entrance of the anode flow channel, which mimics a DMFC design with upstream MCO mitigation.

Figures 7.4 and 7.5 show the plots of cell potential at i = 150 mA cm^{-2} versus FOM for the low-α MEA with upstream MCO mitigation for q = 1, 2, 3, and 4, and q = 1, 3, 5, and 7, respectively. Figure 7.4 is for D_{Mem}^{H2O} held constant for different values of $\mathbb{P}_{Mem}^{MeOH}$, and figure 7.5 is for $\mathbb{P}_{Mem}^{MeOH}/D_{Mem}^{H2O}$ held constant for different values of $\mathbb{P}_{Mem}^{MeOH}$. Note that -- just as was the case with the traditional MEA -- the outliers at high FOM can be attributed to a diminishing rate of return for very high κ^{H+} and low $\mathbb{P}_{Mem}^{MeOH}$ and we do not include these points, denoted with hollow diamonds, in our data correlation.

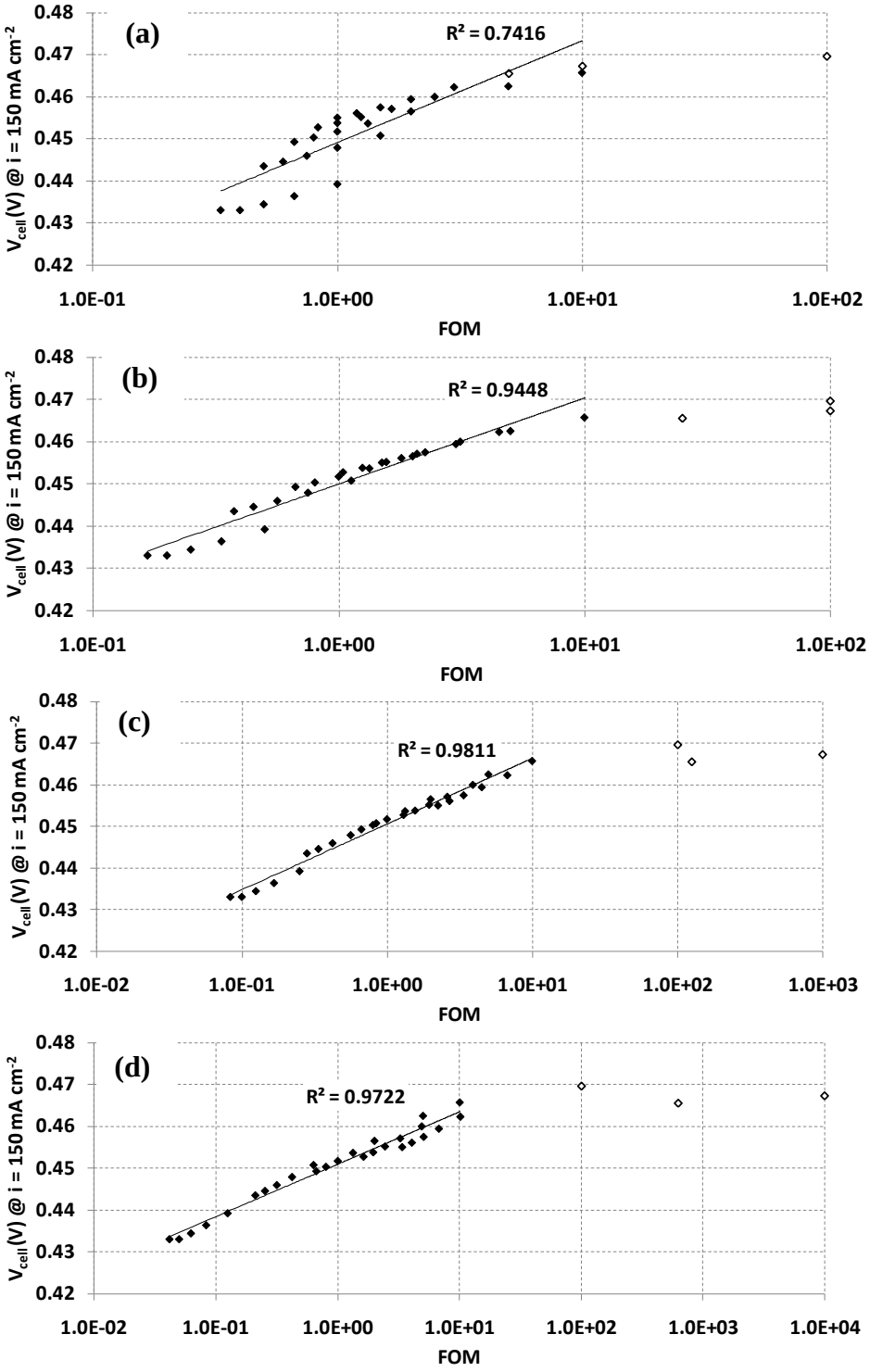

Figure 7.4. Low-α MEA with upstream MCO mitigation; a) q = 1, b) q = 2, c) q = 3, d) q = 4; D_{Mem}^{H2O} is held constant; hollow diamonds are considered outliers; cell properties and simulation parameters given in table A.2.

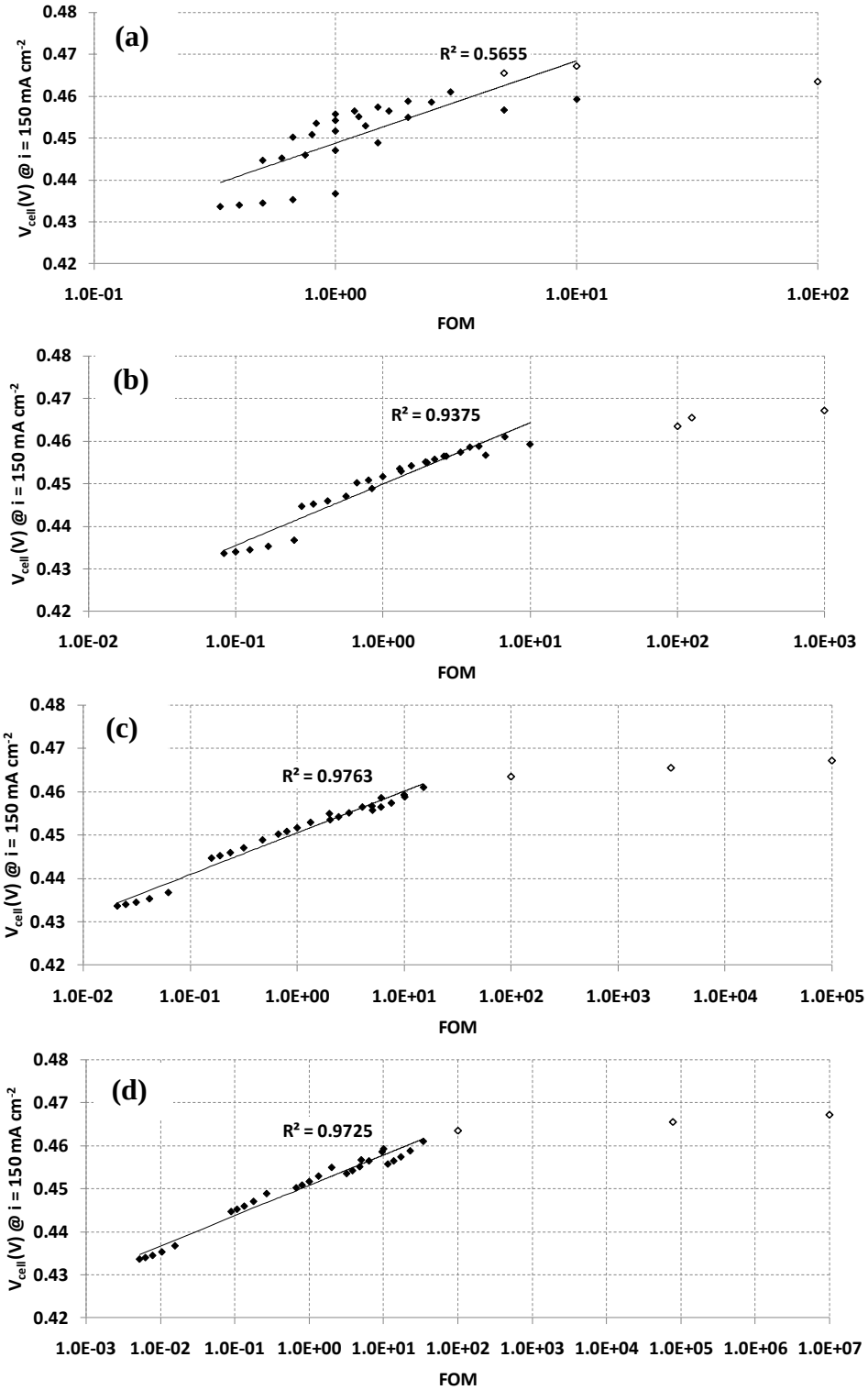

Figure 7.5. Low-α MEA with upstream MCO mitigation; a) q = 1, b) q = 3, c) q = 5, e) q = 7; ($\mathbb{P}_{Mem}^{MeOH}$ /D_{Mem}^{H2O}) is held constant; hollow diamonds are considered outliers; cell properties and simulation parameters given in table A.2.

In figure 7.6, we once again plot the coefficient of determination versus the exponent q. From this figure, we see that the optimal value of q is ~ 3 for D_{Mem}^{H2O} held constant, and ~ 5.5 for $\mathbb{P}_{Mem}^{MeOH}/D_{Mem}^{H2O}$ held constant. This difference in optimal q values indicates that for the low-α MEA with upstream MCO mitigation, the most accurate performance-based FOM depends on not only the membrane methanol permeability, but also the membrane H_2O diffusivity. Physically, the higher value of q for D_{Mem}^{H2O} changed proportionally with $\mathbb{P}_{Mem}^{MeOH}$ implies that, with regards to cell performance, a lower $\mathbb{P}_{Mem}^{MeOH}$ is critically important only if D_{Mem}^{H2O} remains high, to facilitate a back-diffusion of H_2O from cCL to aCL. The importance of low water crossover on performance can be attributed to the dilution effect of the MeOH fuel in the anode catalyst layer by lower α, as described, for example in chapter 4; essentially a lower methanol crossover yields less mixed potential in the cathode, and a corresponding higher cell voltage.

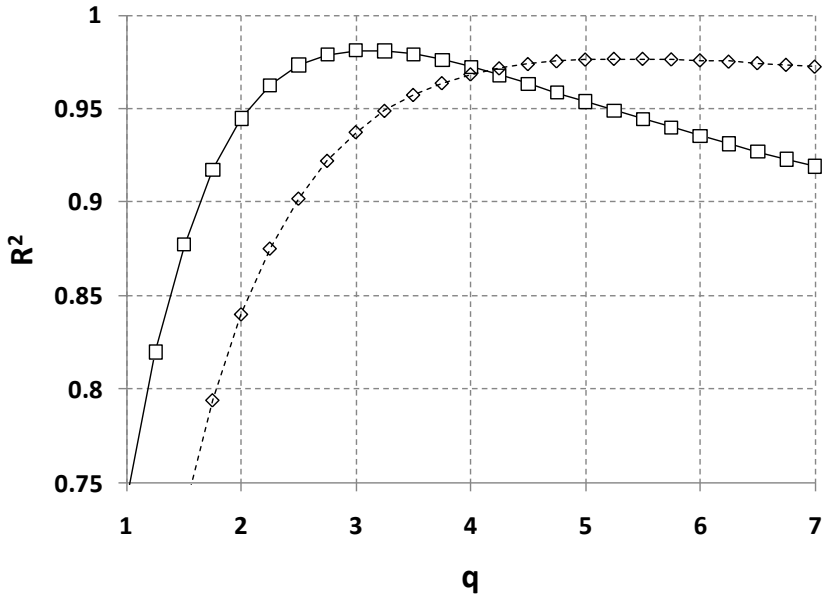

Figure 7.6. Coefficient of determination for different exponents of membrane conductivity, as per equation (7.1); low-α MEA with upstream MCO mitigation; solid line with square is for D_{Mem}^{H2O} = constant, diamond with dashed line is for ($\mathbb{P}_{Mem}^{MeOH}/D_{Mem}^{H2O}$) = constant.

To put this in another light, for the low-α MEA with upstream MCO mitigation design, if we achieve a lower $\mathbb{P}_{Mem}^{MeOH}$, at the expense of simultaneously lowering D_{Mem}^{H2O}, the reduced $\mathbb{P}_{Mem}^{MeOH}$ may not be advantageous, from an overall system design point of view. With q ~ 5.5, a lower methanol permeability will still act to increase the *performance* (cell potential) of the DMFC, as per equation (7.1). However, the effects of a lower MeOH permeability are relatively small, and when the importance of overall water balance is also considered from a system energy density perspective, the lower $\mathbb{P}_{Mem}^{MeOH}$ at the expense of lower D_{Mem}^{H2O} (and higher α) may not be advantageous.

7.3 Advanced low-α MEA with anode transport barrier

The last MEA that we investigate is an advanced low-α MEA with anode transport barrier, as described in chapter 6. The details of the aTB MEA are listed in table A.3. Plots of cell potential at i = 150 mA cm^{-2} versus FOM for this design are shown in figures 7.7 and 7.8 for (a) q = 3, (b) q = 5, (c) q = 7, and (d) q = 9; figure 7.7 is for D_{Mem}^{H2O} held constant for different values of $\mathbb{P}_{Mem}^{MeOH}$, and figure 7.8 is for $\mathbb{P}_{Mem}^{MeOH}/D_{Mem}^{H2O}$ held constant for different values of $\mathbb{P}_{Mem}^{MeOH}$. We see here that while the data still reduces to a logarithmic trend line, there is somewhat more scatter of the data, for this range of q. The outliers at high FOM are once again for the data points with the highest κ^{H+} and lowest $\mathbb{P}_{Mem}^{MeOH}$ in the data set; these outliers are not included in our data correlation, as discussed in section 7.1.

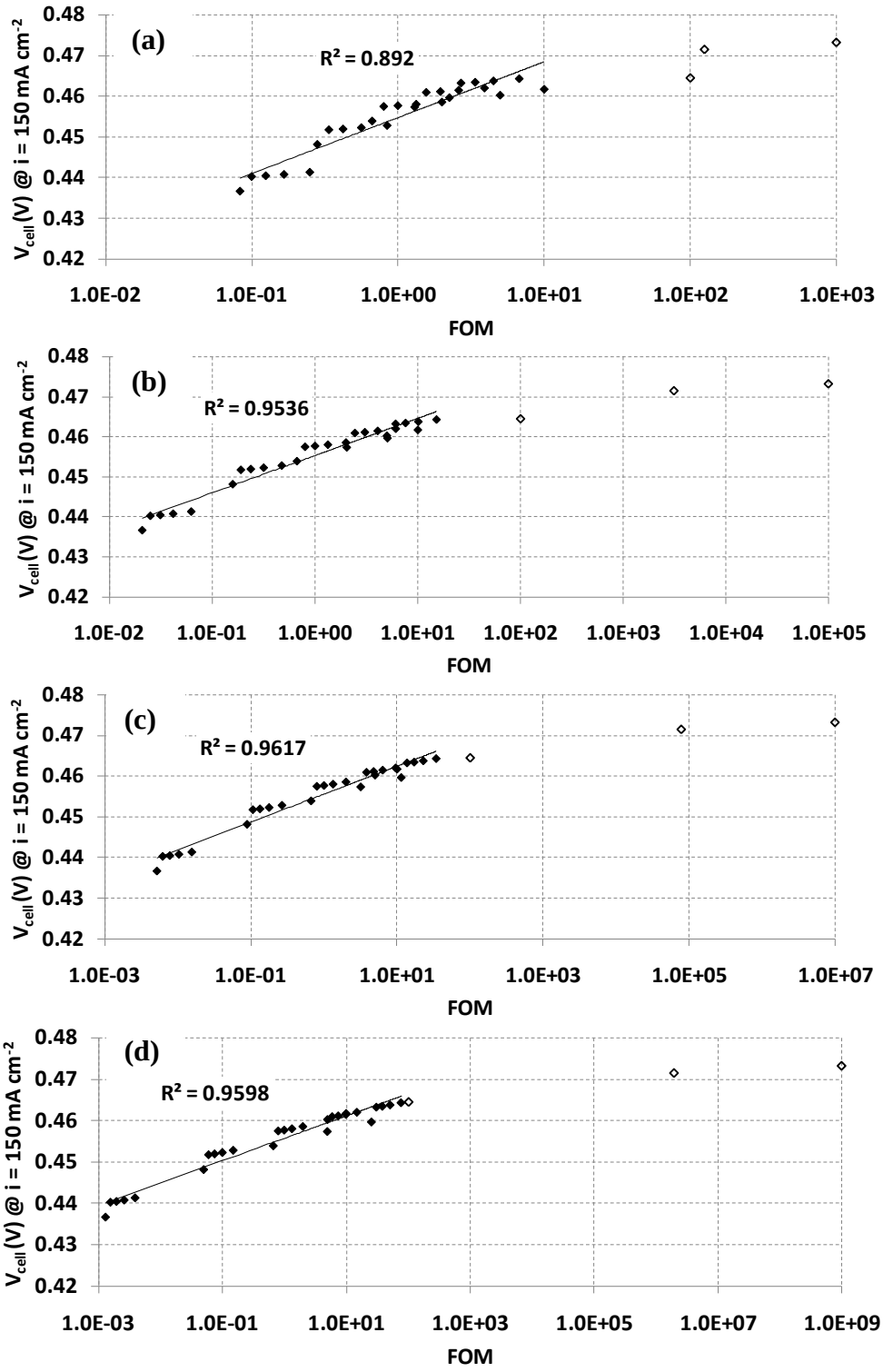

Figure 7.7. Advanced low-α MEA with anode transport barrier; a) q = 3, b) q = 5, c) q = 7, d) q = 9; D_{Mem}^{H2O} is held constant; hollow diamonds are considered outliers; cell properties and simulation parameters given in table A.3.

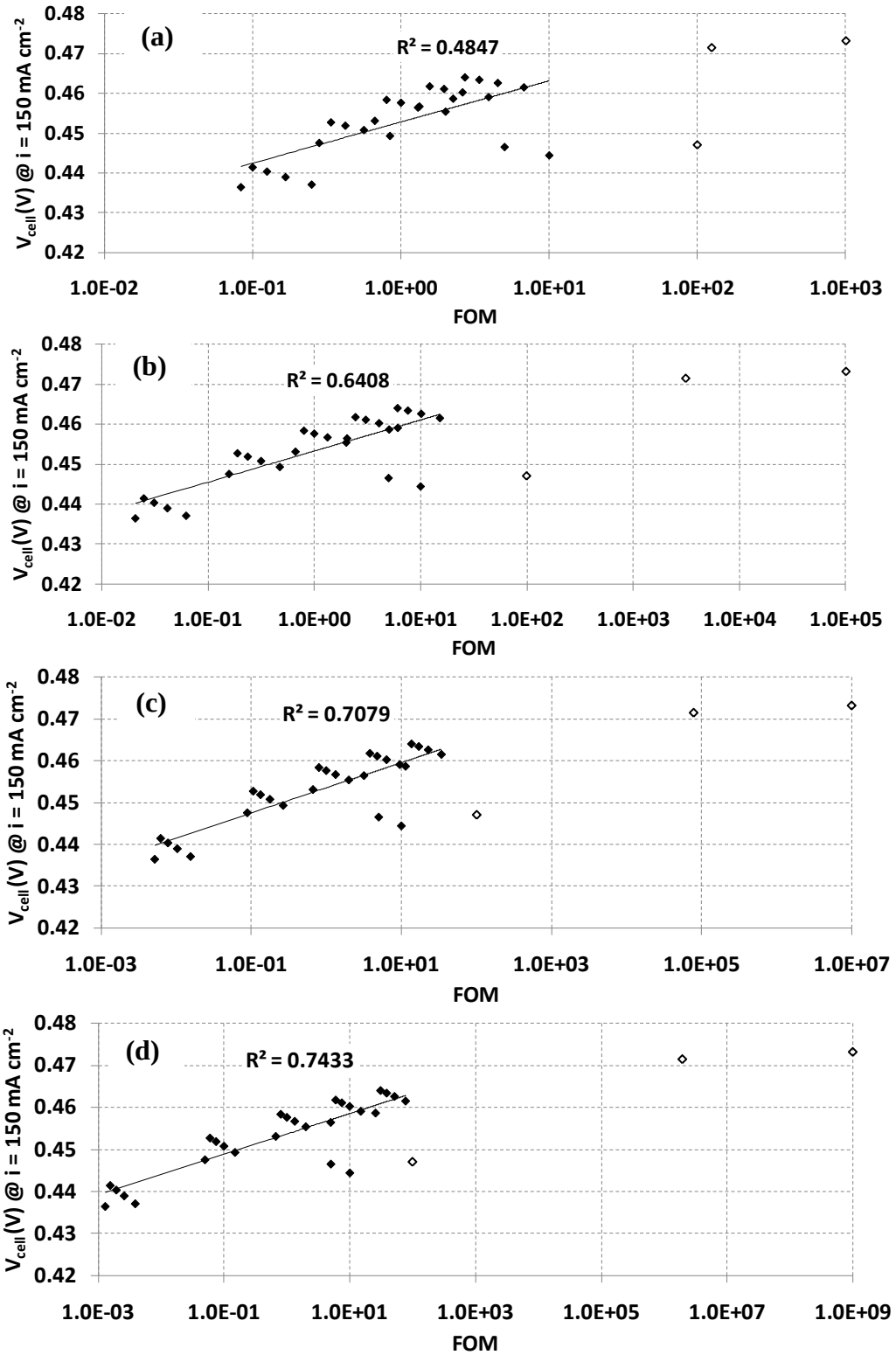

Figure 7.8. Advanced low-α MEA with anode transport barrier; a) q = 3, b) q = 5, c) q = 7, d) q = 9; ($\mathbb{P}_{Mem}^{MeOH}$ /D_{Mem}^{H2O}) is held constant; hollow diamonds are considered outliers; cell properties and simulation parameters given in table A.3.

Figure 7.9 shows the plot of R^2 versus q for the advanced low-α MEA with anode transport barrier. Here we see that for this type of MEA, q ~ 7.25 is the optimal value for D_{Mem}^{H2O} held constant, and for $\mathbb{P}_{Mem}^{MeOH}/D_{Mem}^{H2O}$ held constant, q is much greater than 9. Just as with the low-α MEA with upstream MCO mitigation, the difference in optimal q for the two assumptions of D_{Mem}^{H2O} indicates that the most accurate performance-based FOM advanced low-α MEA with anode transport barrier depends on not only the membrane methanol permeability, but also the membrane H_2O diffusivity. This should come as no surprise, in light of the conclusions reached in chapter 6 (specifically with reference to figures 6.5 and 6.6), where we showed that the aTB is far more effective in reducing MeOH crossover when α is low. In other words, the effectiveness of the anode transport barrier in reducing methanol crossover is directly tied to the success of the low-α MEA in creating a back-diffusion of water from cathode to anode.

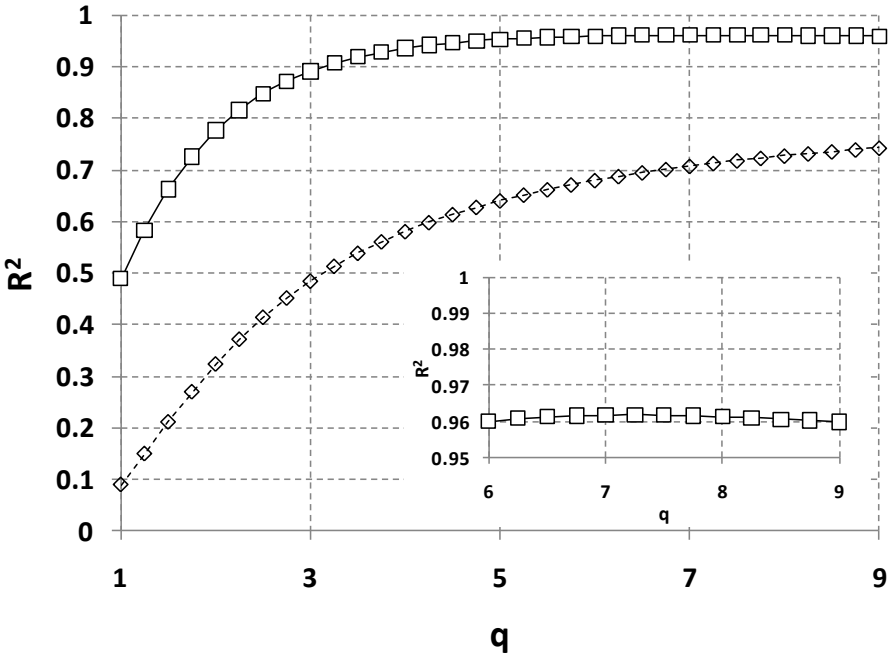

Figure 7.9. Coefficient of determination for different exponents of membrane conductivity, as per equation (7.1); advanced low-α MEA with anode transport barrier; solid line with square is for D_{Mem}^{H2O} = constant, diamond with dashed line is for ($\mathbb{P}_{Mem}^{MeOH}/D_{Mem}^{H2O}$) = constant.

7.4 Comparing traditional, low-α, and aTB MEAs

Table 7.2 gives a summary of the determined exponent values, q, that yield the most accurate performance-based FOM for each MEA design, and for both assumptions of D_{Mem}^{H2O} held constant and $\mathbb{P}_{Mem}^{MeOH}/D_{Mem}^{H2O}$ held constant. It is not surprising that the two advanced MEAs have a higher value of q when compared with the traditional MEA. Recall from equation (7.1) that a higher value of q indicates that relative to one another, the membrane conductivity plays a greater role and the membrane MeOH permeability plays a lesser role in the figure of merit, i.e. in predicting the cell performance. As discussed before, in a traditional MEA, the membrane plays a critical role in reducing the MCO. In the low-α MEA with upstream MCO mitigation, obviously, the MCO is mitigated "upstream". As we mentioned in the introduction to this chapter, the operating conditions -- namely the 2M fuel concentration entering the anode flow channel -- mimic this type of design (for example a mixing chamber which dilutes the fuel prior to its entrance to the anode flow channel); because there is a low fuel concentration at the anode backing layer and flow channel interface, the membrane plays a less critical role in reducing methanol crossover. As we saw in chapter 6, for the aTB MEA, the aTB is designed to play the critical role of reducing the methanol crossover, and hence the value of $\mathbb{P}_{Mem}^{MeOH}$ is much less important when compared with the traditional MEA.

Table 7.2. Exponents, q, for the most accurate performance-based FOM, for the three types of MEAs and for D_{Mem}^{H2O} = constant, and ($\mathbb{P}_{Mem}^{MeOH}/D_{Mem}^{H2O}$) = constant.

	Traditional MEA	**Low- MEA with upstream MCO mitigation**	**Advanced low-α MEA with anode transport barrier**
D_{Mem}^{H2O} constant	2.75	3.0	7.25
($\mathbb{P}_{Mem}^{MeOH}/D_{Mem}^{H2O}$) constant	2.75	5.5	> 9

As seen in table 7.2, the aTB MEA has a more than two-fold greater value of q than the low-α MEA with upstream MCO mitigation. This indicates that for the aTB MEA, the aTB is essentially totally responsible for reducing the methanol crossover to the cathode, while the value of the membrane permeability is nearly negligible. The lower value of q for the low-α MEA with upstream MCO mitigation indicates that the membrane still plays a role in reducing methanol crossover, particularly if D_{Mem}^{H2O} does not decrease proportional to $\mathbb{P}_{Mem}^{MeOH}$, and the back-flux of H_2O via diffusion remains large.

In figure 7.10 we plot the vi curves for the three designs analyzed in this chapter. The low-α MEA with upstream MCO mitigation and advanced low-α MEA with anode transport barrier designs are anode-limited (i.e. the MeOH concentration going to zero in the aCL is what causes the limiting current density), while the traditional MEA is cathode limited (the O_2 concentration goes to zero in the cCL, causing the limiting current density). Note that it would be fairly easy to increase the limiting current density, particularly of the traditional MEA, simply by increasing the stoichiometry; note in table A.4 that we only use a cathode stoichiometry of 1.5, based on a reference current density of 150 mA cm^{-2}.

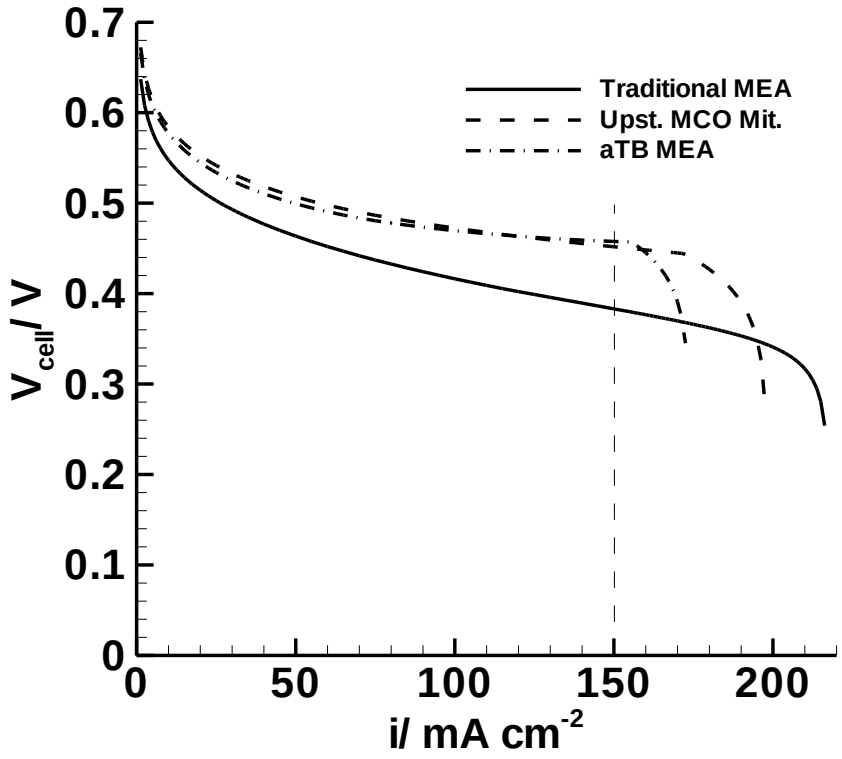

Figure 7.10. vi curves for the traditional MEA, low-α MEA with upstream MCO mitigation, and advanced low-α MEA with anode transport barrier; curves for all three cells have baseline $\mathbb{P}_{Mem}^{MeOH}$ and κ^{H^+}. The vertical dashed line corresponds with our operating current density of i_{op} = 150 mA cm^{-2}.

In contrast to PEFC when used in automotive applications, the power and current draw for DMFCs for mobile applications are typically fairly steady, i.e. the window of operating current density is fairly small. As discussed in references [92] and [93], this fact, combined with zeroth order MOR kinetics for a methanol concentration above 0.1M, allows us to design the cell whereby we operate near an anode limiting current density (i_{op}/i_{lim} ~ 0.75 - 0.9), so as to minimize the MCO and the deleterious effects of cathode mixed potential. This is precisely why we have chosen to compare the three types of cells at an operating current density of 150 mA cm^{-2}, and this is highlighted in figure 7.11, which shows the methanol crossover ratio versus the current density for all

three cell designs. Note that for the traditional MEA, we could increase the limiting current density by using a higher stoichiometry, and then use a corresponding higher operating current density, in effort to reduce MCO. However, it is highly undesirable to operate below V_{cell} ~ 0.4 V because the voltaic efficiency becomes exceedingly small (a cell potential of 0.4 V corresponds to a voltaic efficiency of ~ 33%).

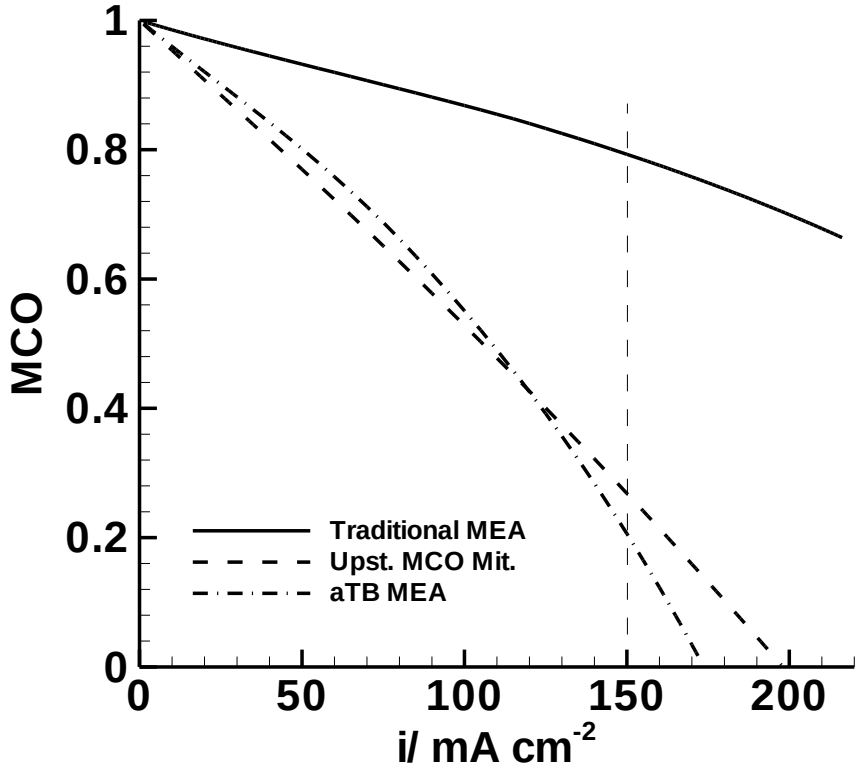

Figure 7.11. MCO curves for the traditional MEA, low-α MEA with upstream MCO mitigation, and advanced low-α MEA with anode transport barrier; curves for all three cells have baseline $\mathbb{P}_{Mem}^{MeOH}$ and κ^{H^+}. The vertical dashed line corresponds with our operating current density of i_{op} = 150 mA cm^{-2}.

We mention all of this for two reasons. First, we want to explain and justify why it is reasonable to compare the three cell design at the chosen current density of 150 mA cm^{-2}. Second, we should point out that an additional reason that the optimal q value for the aTB is more than twice that of the low-α MEA with upstream MCO mitigation, could

be that for the aTB MEA our operating current density is closer to the limiting current density. At this greater i_{op}/i_{lim}, the MeOH concentration in the aCL and corresponding MCO are already exceedingly low. Hence, the minimal importance of $\mathbb{P}_{Mem}^{MeOH}$ on performance, and the very high value of q. Again, while it is certainly reasonable to assume this operating current density, we hypothesize that if we compared the low-α MEA with upstream MCO mitigation and advanced low-α MEA with aTB at the same value of i_{op}/i_{lim}, (or engineered the aTB to yield a limiting current density the same as the low-α MEA with upstream MCO mitigation), the optimal values of q for the two cells would not be as far apart.

7.5 General conclusions

Our primary goal in this chapter was to determine whether or not the traditionally used selectivity (FOM with q = 1) is the best indicator of performance for a DMFC membrane. As summarized in table 7.2, we have shown that in fact for all three designs studied, selectivity is not the best indicator of performance. Even for the traditional MEA, for which we should expect to see the lowest value of q, the best FOM was shown to have the exponent q ~ 2.75. This indicates that for even the traditional MEA, the membrane conductivity plays a greater role, and the MeOH permeability plays a lesser role in predicting the DMFC performance, than as indicated by the selectivity. For the two advanced MEA designs, the value of q is even larger, indicating an even lesser importance of the membrane MeOH permeability in predicting performance. Therefore, we can conclude that the best performance-based figure of merit depends strongly on the type of MEA.

We also showed in this chapter that whether D_{Mem}^{H2O} remains constant for changing methanol permeability, or D_{Mem}^{H2O} changes proportionally with $\mathbb{P}_{Mem}^{MeOH}$ significantly effects the figure of merit for both the low-α MEA with upstream MCO mitigation and the advanced low-α MEA with aTB. This should come as no surprise, due to the role of the membrane in achieving low water crossover via back-diffusion of H_2O in any type of low- α MEA. This finding indicates that in future work, an inclusive FOM should also incorporate the effects of D_{Mem}^{H2O}. From the perspective of proper membrane design and selection, this finding further means that in addition to proton conductivity and MeOH permeability, the membrane's water diffusivity must *also* be considered as an important parameter, especially if the membrane is incorporated in a low- α MEA.

Chapter 8. Summary, Conclusions, and Future Work

8.1 Summary

In chapter 4, we described the fundamental coupling between water and fuel management, especially as it pertains to proper MEA design for high concentration methanol fuel cells. Specifically, we described how an MEA designed to reduce methanol crossover must also reduce water in order to be effective. These concepts expanded nicely on the discussions of fuel and water management given in chapter 1 (particularly with reference to figure 1.9), which dealt with the importance of fuel and water management from the standpoint of overall species balance, without specific regard to MEA design.

Chapter 5 gave a theoretical explanation of the recently observed water crossover reduction in an MEA with hydrophobic anode MPL. To put simply, a hydrophobic anode MPL acts as a greater barrier to capillary-induced liquid flow from the anode flow channel into the anode catalyst layer. This creates a drier anode catalyst layer, and ultimately a lower rate of water crossover to the cathode. In chapter 6, we used a hydrophobic anode MPL in conjunction with the newly proposed anode transport barrier to create a novel MEA structure that facilitates the direct and efficient use of concentrated methanol fuel. Further, in this chapter we discussed physically what makes the anode MPL and transport barrier an effective combination in simultaneously reducing water and methanol crossover. Finally, in chapter 7 we evaluated the use of the membrane selectivity as the traditional figure of merit used for evaluating DMFC membranes. Our findings show that the selectivity over-predicts the importance of methanol permeability,

and under-predicts the importance of the membrane proton conductivity, on DMFC performance (cell potential). We further showed that an inclusive membrane figure of merit must include consideration of not only membrane permeability and proton conductivity, but also the membrane water diffusivity.

8.2 Conclusions

As noted in chapter 1, all of the ideas, concepts, designs, theory, etc. presented in this dissertation have the overall and common goal of increasing the practical system energy density of DMFCs. Increasing the practical energy density is critically important in order for DMFCs to become a viable option as a mobile power source. As described at length in chapter 1, the efficient use of more highly concentrated methanol fuel by means of internal fuel and water management (essentially MEA design), greatly increases the DMFC system energy density by (1) allowing the DMFC system to carry more concentrated fuel in the fuel tank, and (2) greatly reducing or eliminating the need for extra equipment required for external fuel and water management.

As fuel and water management was the primary topic of chapters 4 through 6, the work in these chapters directly addresses increasing the practical energy density of DMFCs. As shown in chapter 7, because the membrane methanol permeability and water diffusivity play a key role in the performance of DMFC, the work therein also addresses the practical energy density of DMFCs via fuel and water management. Further, because the membrane conductivity directly affects the DMFC performance (cell voltage), the work in chapter 7 also *directly* addresses the practical energy density of DMFCs by simply helping us choose membranes which will yield better performance, i.e. be more efficient in converting the fuel in our system into useable energy.

The lasting impact of this work is first of all the theory and fundamentals developed in regards to fuel and water management within the MEA. This includes the more general theory as to the inherent coupling between fuel and water management, as presented in chapter 4, and the more specific theory given in chapter 5 as to how a hydrophobic anode MPL is effective in reducing water crossover. The concepts developed in chapters 4 and 5 were further developed in chapter 6, and have been presented for the first time in the open literature. An understanding of this theory is critically important in the development of advanced MEAs designed for proper fuel and water management, and will act as a guide for future researchers and MEA designers. In fact, in chapter 6, we directly used the theory developed, and proposed a novel MEA design with hydrophobic anode MPL and anode transport barrier. This specific MEA design also has a lasting impact, in that it directly addresses proper fuel and water balance, leading to a more energy dense DMFC. Finally, our work in chapter 7 is important because the membrane selectivity, as the traditional figure of merit for DMFC membranes, is widely used to quickly compare different membranes, and predict how effective they will be in an operating DMFC. What we have shown in chapter 7 is that using the membrane selectivity as a rule of thumb is not a very good figure of merit for indicating performance, and could lead to false conclusions when comparing different membranes. Even *more* importantly, we showed conclusively that in addition to membrane MeOH permeability and proton conductivity, the membrane designer must also consider the membrane water diffusivity as a vitally important membrane property.

8.3 Future work

The MEA described in chapter 6 with hydrophobic anode MPL and anode transport barrier was developed using the 1D, two phase model described in chapter 3. This MEA certainly fit well the concepts we developed in chapters 4 through 6, and, as mentioned in chapter 6, there is some superficial experimental evidence that suggests our MEA design will be effective in its stated goals [62]. However, further rigorous experimental testing of this concept is needed. The next step would naturally be to perform such experiments.

Also, as mentioned in chapter 7, an inclusive membrane figure of merit must incorporate the property effects of the membrane water diffusivity. To this point in time, we have yet to develop such an inclusive membrane figure of merit, and doing so is another item of future work.

Finally, an interesting study in the future would be to investigate the effects of ageing on modeling efforts, and our prediction capabilities. For example, if the membrane properties and characteristics change over time, how will this influence our results, and the conclusions we have drawn from these results? Or, if the individual layers in our MEA degrade over time, how will this alter the fuel and water balance in our MEA?

References

[1] T. Friedman, "The World is Flat," Farrar, Straus and Giroux (2006)

[2] J.R. Healey, “Test Drive: Honda’s FCX fuel-cell car ready for its close-up,” USA Today, May 18, 2007

[3] S. Gottesfeld, ‘Polymer Electrolyte and Direct Methanol Fuel Cells’ in “Encyclopedia of Electrochemistry, 5”, A.J. Bard and M. Stratmann (eds.), Wiley, Weinheim, Chapter 8.3, pp. 544-661 (2007)

[4] C.Y. Wang, Chem. Rev., 104, 4727 (2004)

[5] G. Lu and C.Y. Wang, ‘Two-phase Microfluidics, Heat and Mass Transport in Direct Methanol Fuel Cells’ in “Transport Phenomena in Fuel Cells”, B. Sunden and M. Faghri (eds.), WIT Press, Boston, Chapter 9, pp. 318-358 (2004)

[6] S.K. Kamarudin, W.R.W. Daud, S.L. Ho, and U.A. Hasran, J. Power Sources, 163, 743 (2007)

[7] S. Song, and P. Tsiakaras, Appl. Catal., B, 63, 187 (2006)

[8] L.J.Blomen and M.N. Mugerwa, "Fuel Cell Systems," Plenum Press (1993)

[9] J. Larminie and A. Dicks, "Fuel Cell Systems Explained, 2nd ed.," Wiley (2003)

[10] J. Ge, A. Higier, and H. Liu, J. Power Sources, 159, 922 (2006)

[11] M.F. Mathias, J. Diffusion media materials and characterization,', in "Handbook of Fuel Cells, 3," W. Vielstich, A. Lamm, and H.A. Gasteiger (eds.), Wiley, Chichester, West Sussex, England, Chapter 42, pp. 517-537 (2003)

[12] M. Eikerling, A. Kornyshev, and A. Kulikovsky, 'Can theory help to improve fuel cells?,' in "The Fuel Cell Review", December 2004/January 2005

[13] M.J. Moran and H.N. Shapiro, "Fundamentals of Engineering Thermodynamics, 5th ed.," Wiley (2004)

[14] R.A. Serway and R.J. Beichner, "Physics for Scientists and Engineers, 5th ed.," Saunders College Publishing (2000)

[15] R. O’Hayre, S.W. Cha, W. Colella, and F.B. Prinz, "Fuel Cell Fundamentals," Wiley (2006)

[16] C.K. Dyer, J. Power Sources, 106, 31 (2002)

[17] Y.H. Pan, Electrochem. Solid-State Lett., 9, A349 (2006)

[18] S. Davis, 'Portables Eye Micro Fuel Cells to Replace Batteries' in "Electronic Design," January 12, 2006

[19] P. Kallender, 'Hitachi, Toshiba show portable fuel cells,' in "PC World", October 6, 2004

[20] M. Williams, 'Panasonic shows laptop fuel cell,' in "PC World," January 6, 2006

[21] Toshiba press release, "Toshiba Launches Direct Methanol Fuel Cell in Japan as External Power for Mobile Electronic Devices", http://www.toshiba.com/taec/news/press_releases/2009/dmfc_09_580.jsp, October 22, 2009

[22] V.B. Oliveira, D.S. Falcao, C.M. Rangel, and A.M.F.R. Pinto, Int J Hydrogen Energ, 32, 415 (2007)

[23] K. Scott, W. Taama, and J. Cruickshank, J. Power Sources,65, 159 (1997)

[24] K. Scott, W. Tamma, and J. Cruickshank, J. Appl. Electrochem., 28, 289 (1998)

[25] K. Scott, K., P. Argyropoulos, and K. Sundmacher, J. Electroanal. Chem., 79, 169 (1999)

[26] J. Cruickshank and K. Scott, J. Power Sources, 70, 40 (1998)

[27] K. Sundmacher and K. Scott, Chem. Eng. Sci., 54, 2927 (1999)

[28] K. Sundmacher, T. Schultz, S. Zhou, K. Scott, M. Ginkel, and E.D. Gilles, Chem. Eng. Sci., 56, 333 (2001)

[29] P. Argyropoulos, K. Scott, A.K. Shukla, and C. Jackson, J. Power Sources, 123, 190 (2003)

[30] H. Dohle and K. Wippermann, J. Power Sources, 135, 152 (2004)

[31] A.A. Kulikovsky, Electrochem. Commun., 4, 939-946 (2002)

[32] A.A. Kulikovsky, Electrochem. Commun., 5, 1030 (2003)

[33] J.P. Meyers and J. Newman, J. Electrochem. Soc., 149, A710 (2002)

[34] J.P. Meyers and J. Newman, J. Electrochem. Soc., 149, A718 (2002)

[35] J.P. Meyers and J. Newman, J. Electrochem. Soc., 149, A729 (2002)

[36] T. Schultz and K. Sundmacher, J. Power Sources, 145, 435 (2005)

[37] H. Dohle, J. Divisek, and R. Jung, J. Power Sources, 86, 469 (2000)

[38] B.L. Garcia, V.A. Sethuraman, J.W. Weidner, R.E. White, and R. Dougal, J. Fuel Cell Sci. Technol., 1, 43 (2004)

[39] G. Murgia, L. Pisani, A.K. Shukla, and K. Scott, J. Electrochem. Soc., 150, A1231 (2003)

[40] A.K. Shukla, C.L. Jackson, K. Scott, and G. Murgia, J. Power Sources, 111, 43 (2002)

[41] Z.H. Wang and C.Y. Wang, J. Electrochem. Soc., 150, A508 (2003)

[42] W. Liu, C.Y. Wang, J. Electrochem. Soc., 154, B352 (2007)

[43] W. Liu and C.Y. Wang, J. Power Sources, 164, 189 (2007)

[44] F. Liu and C.Y. Wang, J. Electrochem. Soc., 154, B514 (2007)

[45] P.S. Kauranen and E. Skou, J. Electroanal. Chem., 408, 189 (1996)

[46] V. Neburchilov, J. Martin, H. Wang, and J. Zhang, J. Power Sources, 169, 221 (2007)

[47] T. Yamaguchi, F. Miyata, and S. Nakao, J. Membr. Sci., 214, 283 (2003)

[48] G.Q. Lu, C.Y. Wang, T.J. Yen, and X. Zhang, Electrochim. Acta, 49, 821 (2004)

[49] C.Y. Wang, F. Liu, Y. Sato, and E. Sakaue, "Dual-pump Anode System with Circulating Liquid for Direct Oxidation Fuel Cells", U.S. Patent Pub. No. US 2007/0087234 A1 (2007)

[50] M.A. Abdelkareem and N. Nakagawa, J. Power Sources, 162, 114 (2006)

[51] W.J. Kim, H.G. Choi, Y.K. Lee, J.D. Nam, S. M. Cho, and C.H. Chung, J. Power Sources, 157, 193 (2006)

[52] H.F. Zhang, and I.M. Hsing, J. Power Sources, 167, 450 (2007)

[53] Y.H. Chan, T.S. Zhao, R. Chen, and C. Xu, J. Power Sources, 176, 183 (2008)

[54] C.Y. Wang, G. Lu, W. Liu, F. Liu, Y. Sato, E. Sakaue, and K. Matsuoka, "Methods to Control Water Flow and Distribution in Direct Methanol Fuel Cells", U.S. Patent Pub. No. US 2006/0134487 A1 (2006)

[55] X. Ren, F.W. Kovacs, K.J. Shufon, and S. Gottesfeld, "Passive Water Management Techniques in Direct Methanol Fuel Cells", U.S. Patent Pub. No. US 2004/0209154 A1 (2004)

[56] A. Blum, T. Duvdevani, M. Philosoph, N. Rudoy, and E. Peled, J. Power Sources, 117, 22 (2003)

[57] F. Liu, G. Lu, and C.Y. Wang, J. Electrochem. Soc., 153, A543 (2006)

[58] G.Q. Lu, F.Q. Liu, and C.Y. Wang, Electrochem. Solid-State Lett., 8, A1 (2005)

[59] C. Lim, and C.Y. Wang, J. Power Sources, 113, 145 (2003)

[60] C.Y. Wang and F. Liu, 'A Paradigm Sift in Direct Methanol Fuel Cell Design for Portable Power', Chapter 10, Proceedings from the 8th Small Fuel Cell Symposium, Washington DC, April, 2006

[61] F.Q. Liu, "Optimizing Membrane Electrode Assembly of Direct Methanol Fuel Cells for Portable Power," Ph.D. Dissertation, The Pennsylvania State University, University Park, PA (2006)

[62] F.Q. Liu and C.Y. Wang, Electrochim. Acta, 53, 5517 (2008)

[63] U. Pasaogullari, and C.Y. Wang, J. Electrochem. Soc., 151, A399 (2004)

[64] K.Y. Song, H.K. Lee, and H.T. Kim, Electrochim. Acta, 53, 637 (2007)

[65] J.Y. Park, J.H. Lee, S.K. Kang, J.H. Sauk, and I. Song, J. Power Sources, 178, 181 (2008)

[66] C. Xu, T.S. Zhao, and Y.L. He, J. Power Sources, 171, 268 (2007)

[67] T.A. Zawodzinski, J. Davey, J. Valerio, S. Gottesfeld, Electrochim. Acta, 40, 297 (1995)

[68] T.A. Zawodzinski, C. Derouin, S. Radzinski, R.J. Sherman, V.T. Smith, T.E. Springer, S. Gottesfeld, J. Electrochem. Soc., 140, 1041 (1993)

[69] X. Ren, W. Henderson, S. Gottesfeld, J. Electrochem. Soc., 144, L267 (1997)

[70] C.M. Gates, J. Newman, AIChE J., 46, 2076 (2000)

[71] J.H. Nam and M. Kaviany, Int. J. Heat Mass Transfer, 46, 4595 (2003)

[72] R.H. Brooks and A.T. Corey, 'Hydraulic properties of porous media,' in "Hydrology papers at Colorado State University," March, 1964

[73] M. Kaviany, "Principles of Heat Transfer in Porous Media, 2nd ed.," Springer, (1995)

[74] U. Pasaogullari and C.Y. Wang, Electrochim. Acta, 49, 4359 (2004)

[75] W. Liu, "Methanol, Water, and Heat Transport in Direct Methanol Fuel Cells for Portable Power," Ph.D. Thesis, The Pennsylvania State University, University Park, PA, August 2005

[76] R.A. Bird, W.E. Stewart, and E.N. Lightfoot, "Transport Phenomena, 2nd ed.," Wiley, (2002)

[77] X. Ye, and C.Y. Wang J. Electrochem. Soc., 154, B683 (2007)

[78] M.L. McGlashan, A.G. Williamson, J. Chem. Eng. Data, 21, 196 (1976)

[79] Y. Wang and C.Y. Wang, J. Electrochem. Soc., 153, A1193 (2006)

[80] E.L. Knuth, Phys. Fluids, 2, 339 (1959)

[81] X. Ren, P. Zelenay, S. Thomas, J. Davey, S. Gottesfeld, J. Power Sources, 86, 111 (2000)

[82] Y. Sone, P. Ekdunge, D. Simonsson, J. Electrochem. Soc., 143, 1254 (1996)

[83] T.E. Springer, T.A. Zawodzinski, and S. Gottesfeld, J. Electrochem. Soc., 138, pp. 2334 (1991)

[84] H.A. Gasteiger, J. Garche, 'Fuel Cells,' in "Handbook of Heterogeneous Catalysis, 2nd ed.," C. Ertl, H. Knozinger, F. Schuth, J. Weitkamp (eds.), John Wiley & Sons Ltd., Chichester, UK, Chapter 13.20.2, pp. 3081-3121 (2008)

[85] J. NordlundJ. Electrochem. Soc., 149, A1107 (2002)

[86] J. Newman and K. Thomas-Alyea, "Electrochemical Systems," Wiley (2004)

[87] J.T. Wang, S. Wasmum, and R.F. Savinell, J. Electrochem. Soc., 143, 1233 (1996)

[88] N.W. Deluca, Y.A. Elabd, J. Polym. Sci., Part B: Polym. Phys., 44, 2201 (2006)

[89] V. Tricoli, J. Electrochem.Soc., 145 3798 (1998)

[90] V. Tricoli, N. Carretta, M. Bartolozzi, J. Electrochem.Soc., 147 1286 (2000)

[91] C.W. Lin, K.C. Fan, R. Thangamuthu, J. Membrane Sci., 278, 437 (2006)

[92] S. Gottesfeld, C. Minas, 'Optimization of Direct Methanol Fuel Cell Systems and Their Mode of Operation' in "Mini-Micro Fuel Cells, Fundamentals and Applications", S. Kakac, A. Pramuanjaroenkij, and L. Vasiliev (eds.), Springer, Dordrecht, The Netherlands, pp. 257-268 (2008)

[93] S. Gottesfeld, Presentation at Penn State Electrochemical Engine Center, Fall, 2007

[94] R.B. Mrazek, C.E. Wicks, K.N.S. Prabhu, J. Chem. Eng. Data, 13, 508 (1968)

[95] B.E. Poling, J.M. Prausnitz, J.P. O'Connell, "The Properties of Gases and Liquids, 5th ed.", McGraw-Hill (2001)

[96] Z.J. Derlacki, A.J. Easteal, V.J. Edge, L.A. Woolf, Z. Roksandic, J. Phys. Chem., 89, 5318 (1985)

Appendix A Properties and Parameters

Table A.1. Cell properties and simulation parameters used in chapter 4.

Parameter	Value	Notes
*δ_{BL} / μm	260 w/ MPL 280 w/o MPL	Anode and Cathode
δ_{MPL} / μm	20	Anode and Cathode, if present
δ_{CL} /μm	15	Anode and Cathode
δ_{Mem} / μm	50	Nafion® 112
ε_{BL}, ε_{CL}	0.6	Anode and Cathode
ε_{MPL}	0.4	Anode and Cathode
K_{BL} / m^2	$1.0x10^{-14}$	Anode and Cathode
K_{MPL} / m^2	$2.0x10^{-15}$	Anode and Cathode
K_{CL} / m^2	$3.6x10^{-16}$	Anode and Cathode
K_{Mem} / m^2	$4.0x10^{-20}$	
θ_{BL} / ^{o}	110	Anode and Cathode
θ_{MPL} / ^{o}	120	Anode and Cathode
θ_{CL} / ^{o}	96	Anode and Cathode
Temperature / ^{o}C	60	

*Note that the different BL thicknesses with and without MPL are to ensure equivalent thickness of the diffusion media and study the effects of the MPL properties on the water and methanol crossover.

Table A.2. Baseline DMFC parameters for low-α MEA used in chapters 5 and 7.

Parameter	Value	Notes
δ_{BL} / μm	260	Anode and Cathode
δ_{MPL} / μm	20	Anode and Cathode
δ_{CL} /μm	15	Anode and Cathode
δ_{Mem} / μm	50	Nafion® 112
ε_{BL}, ε_{CL}	0.6	Anode and Cathode
ε_{MPL}	0.4	Anode and Cathode
K_{BL} / m^2	1.0×10^{-14}	Anode and Cathode
K_{MPL} / m^2	2.0×10^{-15}	Anode and Cathode
K_{CL} / m^2	3.6×10^{-16}	Anode and Cathode
K_{Mem} / m^2	4.0×10^{-20}	
θ_{BL} / ^{o}	110	Anode and Cathode
θ_{MPL} / ^{o}	120	Anode and Cathode
θ_{CL} / ^{o}	96	Anode and Cathode
Temperature / K	333	
Pressure / Pa	101325	
Fuel Concentration, $c_{l,o}^{MeOH}$ / M	2.0	
Anode Stoichiometry, ξ_a @ i_{ref} = 150 mA cm^{-2}	2.0	Used in chapter 5
	1.5	Used in chapter 7
Cathode Stoichiometry, ξ_c @ i_{ref} = 150 mA cm^{-2}	2.0	Used in chapter 5
	1.5	Used in chapter 7

Table A.3. Baseline cell properties and simulation parameters for MEA with aTB used in chapters 6 and 7.

Parameter	Value	Notes
δ_{BL}/ μm	260	Anode and Cathode
δ_{aTB}/ μm	260	
δ_{MPL}/ μm	20	Anode and Cathode
δ_{CL}/ μm	15	Anode and Cathode
δ_{Mem}/ μm	50	Nafion® 112
ε_{BL}, ε_{CL}	0.6	Anode and Cathode
ε_{aTB}	0.25	
ε_{MPL}	0.4	Anode and Cathode
K_{BL}/ m^2	1.0×10^{-14}	Anode and Cathode
K_{aTB}/ m^2	1.0×10^{-14}	
K_{MPL}/ m^2	2.0×10^{-15}	Anode and Cathode
K_{CL}/ m^2	3.6×10^{-16}	Anode and Cathode
K_{Mem}/ m^2	4.0×10^{-20}	
θ_{BL}/ ^{o}	110	Anode and Cathode
θ_{aTB}/ ^{o}	120	
θ_{MPL}/ ^{o}	120	Anode and Cathode
θ_{CL}/ ^{o}	96	Anode and Cathode
Temperature / K	333	
Pressure / Pa	101325	
Fuel Concentration, $c_{l,o}^{MeOH}$ / M	10.0	
Anode Stoichiometry, ξ_a @ i_{ref} = 150 mA cm^{-2}	2.0	Used in chapter 6
	1.5	Used in chapter 7
Cathode Stoichiometry, ξ_c @ i_{ref} = 150 mA cm^{-2}	2.0	Used in chapter 6
	1.5	Used in chapter 7

Table A.4. Cell properties and simulation parameters for traditional MEA used in chapter 7.

Parameter	Value	Notes
δ_{BL} / μm	260	Anode and Cathode
δ_{CL} /μm	15	Anode and Cathode
δ_{Mem} / μm	175	Nafion® 117
ε_{BL}, ε_{CL}	0.6	Anode and Cathode
K_{BL} / m^2	1.0×10^{-14}	Anode and Cathode
K_{CL} / m^2	3.6×10^{-16}	Anode and Cathode
K_{Mem} / m^2	4.0×10^{-20}	
θ_{BL} / ^{o}	110	Anode and Cathode
θ_{CL} / ^{o}	96	Anode and Cathode
Temperature / K	333	
Pressure / Pa	101325	
Fuel Concentration, $c_{l,o}^{MeOH}$ / M	10.0	
Anode Stoichiometry, ξ_a @ i_{ref} = 150 mA cm^{-2}	1.5	
Cathode Stoichiometry, ξ_c @ i_{ref} = 150 mA cm^{-2}	1.5	

Table A.5. Model properties and correlations.

Correlation or Value	Description	Comment
$k_{rl}=s^4$	Liquid-phase relative permeability.	Reference [72].
$D_g^{MeOH,H_2O} = D_g^{MeOH,CO_2} = 1.96x10^{-5}\left(\frac{T}{328.15K}\right)^{1.823}\frac{1.013x10^5\,Pa}{p}\,m^2s^{-1}$	Gas MeOH, H_2O and MeOH, CO_2 diffusivity.	Chapman Enskog theory for p, T dependence; reference value from [94] for air-MeOH, approximated same for MeOH, H_2O and MeOH, CO_2.
$D_g^{H_2O,CO_2} = 2.01x10^{-5}\left(\frac{T}{307K}\right)^{1.823}\frac{1.013x10^5\,Pa}{p}\,m^2s^{-1}$	Gas H_2O, CO_2 diffusivity.	Chapman-Enskog theory for p, T dependence; reference diffusivity from [95].
$D_g^{O_2} = 3.57x10^{-5}\left(\frac{T}{352K}\right)^{1.823}\frac{1.013x10^5\,Pa}{p}\,m^2s^{-1}$	Gas O_2 diffusivity.	Chapman-Enskog theory for p, T dependence; reference diffusivity from [95] for O_2, H_2O.
$D_l^{MeOH,H_2O} = 1.4x10^{-9}\left[\frac{647.3K-298.15K}{647.3K-T}\right]^6 m^2s^{-1}$	Liquid MeOH diffusivity.	T dependence from [95]; reference value from [96] for dilute MeOH solution.
$\lambda = \begin{cases} 22 & (s>0.3) \\ 14+8s/0.3 & (s\le 0.3) \\ 0.043+17.81RH-39.85RH^2+36.0RH^3 & (vapor) \end{cases}$	Nafion® membrane water content.	Liquid assumed interpolation, upper and lower values from [68]; vapor from [83].
$\mathfrak{D}_{Mem}^{MeOH} = \mathbb{P}_{Mem}^{MeOH} = 1.5x10^{-10}exp\left[2416\left(\frac{1}{303K}-\frac{1}{T}\right)\right]m^2s^{-1}$	Nafion® membrane effective MeOH diffusivity or MeOH permeability.	T dependence taken from [83] for H_2O transport in Nafion® with reference value experimentally calibrated at ECEC.

$D_{Mem}^{H_2O} = 4.80x10^{-11}\exp\left[2416\left(\frac{1}{303K}-\frac{1}{T}\right)\right]\ m^2 s^{-1}$	Nafion® membrane H_2O diffusivity.	T dependence taken from [83] with reference value calibrated at ECEC.
$n_d^{H_2O} = \begin{cases}\left[\frac{\lambda-14}{8}\right]\left(n_{d,ref}^{H_2O}-1\right)+1 & for\ \lambda \geq 14 \\ 1 & for\ \lambda < 14\end{cases}$	H_2O EOD coefficient.	Interpolation assumed; upper and lower values from [5] and [67].
$n_{d,ref}^{H_2O} = 1.6767 + 0.0155(T-273) + 8.9074\times10^{-5}(T-273)^2$	H_2O reference EOD coefficient for membrane in equilibrium with liquid H_2O.	From reference [5].
$n_d^{MeOH} = n_d^{H_2O}\frac{c_l^{MeOH}}{c_{t,l}}$	MeOH drag coefficient.	Assumed similar to reference [42].

Table A.6. Kinetic parameters for cathode electrochemistry model.

Parameter/Value	Description
$K_r = 5.7 \times 10^{-1}$	Reaction coefficient for purely chemical reaction
$k_1 = 0.2 \times 10^{-10}$ / m s^{-1}	Mixed potential kinetic parameter
$k_1' = 1.54 \times 10^{-10}$ / mol m^{-2} s^{-1}	Mixed potential kinetic parameter
$k_2 = 3.6 \times 10^{-16}$ / mol m^{-2} s^{-1}	Mixed potential kinetic parameter
$k_3 = 1.2 \times 10^{-13}$ / mol m^2 s^{-1}	Mixed potential kinetic parameter
$k_3' = 1.4$ / mol m^{-2} s^{-1}	Mixed potential kinetic parameter
$k_4 = 2.0 \times 10^{-2}$ / mol m^{-2} s^{-1}	Mixed potential kinetic parameter
$\alpha_2 = 0.8$	Mixed potential kinetic parameter
$\beta_3 = 0.5$	Mixed potential kinetic parameter
$\beta_4 = 0.5$	Mixed potential kinetic parameter
$\beta = 1.9$	Concentration exponent for MeOH in chemical reaction
$\gamma = 0.01$	Concentration exponent for O_2 in chemical reaction
$K = 1 \times 10^7$	MOR reaction proportionality constant
a = 10^{-7} / m^{-1}	Specific reactive area for cathode, reaction area per volume
$j_{0,ref}^{ORR}$ / A m^{-3}	ORR reference current density

Appendix B Details on Numerical Implementation

B.1 Discretization methods

On the anode side of the cell, the boundary conditions for liquid MeOH concentration and liquid saturation are given at the flow channel/BL interface, and therefore, a backward differencing scheme is utilized for the MeOH transport equation (3.32). Figure B.1 gives a schematic of the nodes on the anode side. Equation (3.32) is discretized in the following manner:

$$c_l^{MeOH}\Big|_i \left[a1+a2\right] + \left.\frac{dc_l^{MeOH}}{dx}\right|_i \left[b1+b2\right] = c1 \tag{B.1}$$

$$c_l^{MeOH}\Big|_i \left[a1+a2\right] + \frac{c_l^{MeOH}\Big|_i - c_l^{MeOH}\Big|_{i-1}}{\Delta x}\left[b1+b2\right] = c1 \tag{B.2}$$

where $a1 = \dfrac{N^{H_2O}}{c_{t,l} - c_l^{MeOH}}$

$$a2 = \frac{N^{CO_2}}{k_H\left[c_{sat}^{H_2O}\left(\dfrac{D_g^{MeOH,CO_2}}{D_g^{MeOH,H_2O}}\right) + c_g^{CO_2}\right]}$$

$$b1 = \frac{c_{t,l} D_{eff,l}^{MeoH,H_2O}}{c_{t,l} - c_l^{MeOH}}$$

$$b2 = \frac{c_{t,g} D_{g,eff}^{MeOH,CO_2}}{k_H\left[c_{sat}^{H_2O}\left(\dfrac{D_g^{MeOH,CO_2}}{D_g^{MeOH,H_2O}}\right) + c_g^{CO_2}\right]}$$

$$c1 = N^{MeOH}(x)$$

i = node location as per figure B.1

Further solving for the liquid MeOH concentration at node i yields

$$c_l^{MeOH}\Big|_i = \frac{c1 - c_l^{MeOH}\Big|_{i-1}\left[\frac{b1+b2}{\Delta x}\right]}{\left[a1+a2\right]-\left[\frac{b1+b2}{\Delta x}\right]} \tag{B.3}$$

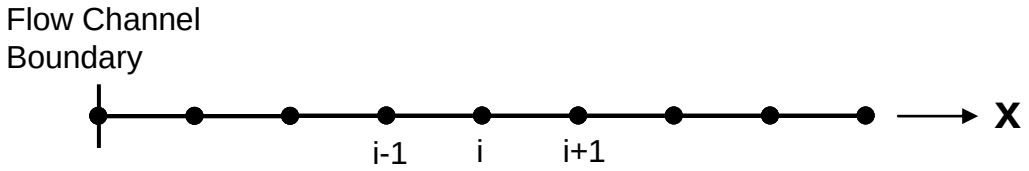

Figure B.1. Node numbering scheme for anode side of the cell.

In the single-phase regions of the anode where equations (3.35) and (3.36) are solved instead of (3.32), similar discretizations are performed yielding the following:

$$c_g^{MeOH}\Big|_i = \frac{f1 - c_g^{MeOH}\Big|_{i-1}\left[\frac{e1}{\Delta x}\right]}{\left[d1+d2\right]-\left[\frac{e1}{\Delta x}\right]} \tag{B.4}$$

where $d1 = \dfrac{N^{CO_2}}{c_g^{H_2O}\left(\dfrac{D_g^{MeOH,CO_2}}{D_g^{MeOH,H_2O}}\right)+c_g^{CO_2}}$

$$d2 = \frac{\left(\dfrac{D_g^{MeOH,CO_2}}{D_g^{MeOH,H_2O}}\right)N^{H_2O}}{c_g^{H_2O}\left(\dfrac{D_g^{MeOH,CO_2}}{D_g^{MeOH,H_2O}}\right)+c_g^{CO_2}}$$

$$e1 = \frac{c_{t,g}D_{eff,g}^{MeOH,CO_2}}{c_g^{H_2O}\left(\dfrac{D_g^{MeOH,CO_2}}{D_g^{MeOH,H_2O}}\right)+c_g^{CO_2}}$$

$$f1 = N^{MeOH}(x)$$

$$c_g^{H_2O}\Big|_i = \frac{k1 - c_g^{H_2O}\Big|_{i-1}\left[\frac{h1}{\Delta x}\right]}{[g1+g2]-\left[\frac{h1}{\Delta x}\right]} \tag{B.5}$$

where $g1 = \dfrac{N^{CO_2}}{c_{t,g} D_{g,eff}^{H_2O,CO_2}}$

$$g2 = \frac{N^{MeOH}}{c_{t,g} D_{g,eff}^{H_2O,MeOH}}$$

$$h1 = 1$$

$$k1 = \frac{\left[c_g^{MeOH}\left(\frac{D_g^{H_2O,CO_2}}{D_g^{H_2O,MeOH}}\right) + c_g^{CO_2}\right] N^{H_2O}(x)}{c_{t,g} D_{g,eff}^{H_2O,CO_2}}$$

It should be noted that in equations (B.1) through (B.5), all of the terms a1, f1, etc. are evaluated at the i node.

On the cathode side of the cell, the O_2 and liquid saturation boundary conditions are known at the BL/flow channel interface, as depicted in Figure B.2. For this reason, on the cathode side a forward differencing scheme is used for the O_2 and MeOH transport equations (3.37) and (3.40), and this leads to the following difference equations:

$$c_g^{O_2}\Big|_i = \frac{p1 + c_g^{O_2}\Big|_{i-1}\left[\frac{m1}{\Delta x}\right]}{\left[\frac{m1}{\Delta x}\right]} \tag{B.6}$$

where $m1 = D_{eff,g}^{O_2}$

$$p1 = N^{O_2}(x)$$

$$c_l^{MeOH}\Big|_i = \frac{u1 + c_l^{MeOH}\Big|_{i-1}\left[\frac{t1+t2}{\Delta x}\right]}{[q1]+\left[\frac{t1+t2}{\Delta x}\right]} \tag{B.7}$$

where $q1 = \frac{N^{H_2O}}{c_{t,l} - c_l^{MeOH}}$

$$t1 = \frac{c_{t,l} D_{eff,l}^{MeoH,H_2O}}{c_{t,l} - c_l^{MeOH}}$$

$$t2 = \frac{D_{g,eff}^{MeOH}}{k_H}$$

$$u1 = N^{MeOH}(x)$$

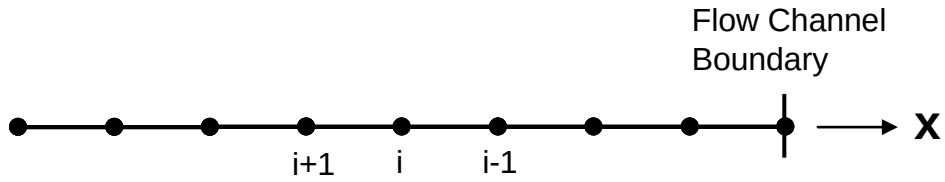

Figure B.2. Node numbering scheme for cathode side of the cell.

For the two phase Darcy Law on both the anode and cathode sides of the cell, we take the following approach. Substituting in equation (2.13) for liquid-phase relative permeability into equation (3.41) and rearranging these equations for ds/dx yields the following expression:

$$\frac{ds}{dx} = \frac{M_l\ \mu_l}{\rho_l\ Ks^q\ (dp_c\ /ds)} N_l\ \ (x) \tag{B.8}$$

As the saturation tends to zero, the right-hand side of (B.8) goes to infinity. For a numerical solution, this becomes a problem. In order to avoid this singularity, both sides are multiplied by $(q+1)s^q$, which after rearranging yields the following:

$$\frac{d}{dx}\left[s^{q+1}\right] = \frac{(q+1)M_l\ \mu_l}{\rho_l\ K(dp_c\ /ds)} N_l\ \ (x) \tag{B.9}$$

On the anode side, we use a backwards difference to approximate the left hand side of equation (B.9), and on the cathode side of the cell we use a forward difference. Then, equation (B.9) is solved for s^{q+1} numerically using the second-order Runge Kutta method. With s^{q+1}, s is directly calculated to determine the liquid saturation within a given porous layer.

On the anode side of the cell, equations (B.3), (B.8), and if necessary (B.4) and (B.5) are solved by marching from the anode flow channel/BL interface to the last node at the CL/membrane interface. On the cathode side, equations (B.6), (B.7), and (B.8) are solved by starting at the cathode flow channel/BL interface, and marching towards the membrane (in the negative x-direction). All of this occurs within the iteration loop for field variables as depicted in figure 3.8.

B.2 Iteration method for source term variables

In order to solve the algebraic equations governing j^{ORR}, r_{chem}, $N_m^{H_2O}$, and N_m^{MeOH}, a hybrid secant/bi-section method is adopted in an effort to optimize the convergence speed, while at the same time making the code robust. In using either the secant or bi-section methods individually, the first step is to move all terms in the algebraic equation to the left-hand side so that the right-hand side equals zero:

$$F(x) = 0 \tag{B.10}$$

where x = generic variable for j^{ORR}, r_{chem}, $N_m^{H_2O}$, or N_m^{MeOH}

For example, for the membrane H_2O flux, equation (2.1) is rearranged in the following manner:

$$F(N_m^{H_2O}) = N_m^{H_2O} - N_{m,EOD}^{H_2O} - N_{m,diff}^{H_2O} - N_{m,pl}^{H_2O} = 0 \tag{B.11}$$

Note here that $N_{m,EOD}^{H_2O}$, $N_{m,diff}^{H_2O}$, and $N_{m,pl}^{H_2O}$ are all function of $N_m^{H_2O}$ as alluded to earlier via the coupling between the differential equations and the membrane flux. In the numerical scheme, the value of $N_m^{H_2O}$ is fixed for the solution loops for the field variables, j^{ORR}, and r_{chem}; after these inner-loop variables converge for the given value of $N_m^{H_2O}$, the components $N_{m,EOD}^{H_2O}$, $N_{m,diff}^{H_2O}$, and $N_{m,pl}^{H_2O}$ are then calculated based on the converged solution of all loops within, based on equations (2.2), (3.12), and (3.13). If the previous value of $N_m^{H_2O}$ matches with the newly calculated component values to within suitable error tolerance, then the correct value of $N_m^{H_2O}$ has been found.

To project a next guess for j^{ORR}, r_{chem}, $N_m^{H_2O}$, and N_m^{MeOH} in the iteration scheme, the secant method is used in conjunction with the function F(x). In the case that the secant method fails to find the root (if F(x) becomes too steep near the root), the bracketed bi-section method is used. As mentioned previously, to ensure that the roots of F(x) have been reached (i.e. the correct values of j^{ORR}, r_{chem}, $N_m^{H_2O}$, and N_m^{MeOH} have been found), the residuals of F(x) are compared with the value of the variable x to ensure that they are at least three orders of magnitude smaller. Directly comparing these two values makes sense here because for j^{ORR}, r_{chem}, $N_m^{H_2O}$, and N_m^{MeOH}, the function F(x) is essentially just $F(x) = x - x_{calc}$, where x is the guessed value and x_{calc} is the calculated value based on the solution from the inner loops.

Appendix C Further Assessment of Model Assumptions

In chapter 3 we noted that we would further evaluate the validity of two assumptions, and particularly their effect on the results presented in this thesis. These assumptions were:

1) Negligible gas-phase H2O flux in a two-phase region of the anode, as per equation (3.3),
2) Approximation of $\frac{dX_l^{MeOH}}{dx} \approx \frac{1}{c_{t,l}} \frac{dc_l^{MeOH}}{dx}$, as given in equation (3.19).

In an updated version of our model, we have removed these two assumptions, and our aim in this section is to compare results from the original model (used to produce the results within the body of this thesis) with the results from the updated model. As will be demonstrated, these assumptions have a minimal effect on our simulated results, and the corresponding conclusion drawn from these results.

In our updated model, dX_l^{MeOH}/dx is determined by the more exact

$$\frac{dX_l^{MeOH}}{dx} = \left(\frac{1}{c_{t,l}}\right)\left[1 - X_l^{MeOH}\frac{dc_{t,l}}{dc_l^{MeOH}}\right]\frac{dc_l^{MeOH}}{dx} \qquad \text{(C.1)}$$

Here, $dc_{t,l}/dc_l^{MeOH}$ is given by equation (3.17). Further, in our updated model, we do not make the approximation $N^{H_2O} \approx N_l^{H_2O}$, as given by equation (3.3). In other words, we explicitly account for the gas-phase H_2O flux in our transport equation. This being the case, in the two-phase anode we must write one further equation for gas-phase H_2O transport. In the updated model, we still utilize the two-phase equilibrium assumption, and ultimately we follow a similar process as we did to obtain equation (3.32), with the final equation given by

$$\frac{dc_l^{MeOH}}{dx} = \frac{F_{62}N_{tot}^{H_2O} - N_{tot}^{MeOH} + \left[\frac{F_{62}\left(C_{80}A_{76} + A_{80}\right) - \left(E_{76}A_{80} + A_{76}\right)}{1 - E_{76}C_{80}}\right]\frac{dT}{dx} + \left[\frac{\left(E_{76}D_{80} + D_{76}\right) - F_{62}\left(C_{80}D_{76} + D_{80}\right)}{1 - E_{76}C_{80}}\right]N_{tot}^{CO_2}}{B_{62} + \left[\frac{\left(E_{76}B_{80} + B_{76}\right) - F_{62}\left(C_{80}B_{76} + B_{80}\right)}{1 - E_{76}C_{80}}\right]} \quad \text{(C.2)}$$

In equation (C.2), we have

$$F_{62} = \frac{X_l^{MeOH}}{X_l^{H_2O}}$$

$$A_{76} = \left[\frac{\frac{\partial c_{sat,mix}^{MeOH}}{\partial T} D_{g,eff}^{MeOH,H_2O}}{X_g^{H_2O} + \Delta_{CO_2}^{H_2O} X_g^{CO_2}}\right]$$

$$B_{76} = \left[\frac{\frac{\partial c_{sat,mix}^{MeOH}}{\partial c_l^{MeOH}} D_{g,eff}^{MeOH,H_2O}}{X_g^{H_2O} + \Delta_{CO_2}^{H_2O} X_g^{CO_2}}\right]$$

$$D_{76} = \left[\frac{\Delta_{CO_2}^{H_2O} X_g^{MeOH}}{X_g^{H_2O} + \Delta_{CO_2}^{H_2O} X_g^{CO_2}}\right]$$

$$E_{76} = \left[\frac{X_g^{MeOH}}{X_g^{H_2O} + \Delta_{CO_2}^{H_2O} X_g^{CO_2}}\right]$$

$$A_{80} = \left[\frac{\frac{\partial c_{sat,mix}^{H_2O}}{\partial T} D_{g,eff}^{MeOH,H_2O}}{X_g^{MeOH} + \Delta_{CO_2}^{MeOH} X_g^{CO_2}}\right]$$

$$B_{80} = \left[\frac{\frac{\partial c_{sat,mix}^{H_2O}}{\partial c_l^{MeOH}} D_{g,eff}^{MeOH,H_2O}}{X_g^{MeoH} + \Delta_{CO_2}^{MeOH} X_g^{CO_2}}\right]$$

$$C_{80} = \left[\frac{X_g^{H_2O}}{X_g^{MeOH} + \Delta_{CO_2}^{MeOH} X_g^{CO_2}}\right]$$

$$D_{80} = \left[\frac{\Delta_{CO_2}^{MeOH} X_g^{H_2O}}{X_g^{MeOH} + \Delta_{CO_2}^{MeOH} X_g^{CO_2}} \right]$$

$$\Delta_{\beta}^{\alpha} \equiv \frac{D_{g,eff}^{\gamma,\alpha}}{D_{g,eff}^{\gamma,\beta}}$$

In the updated model, we also account for the heat pipe effect on MeOH and H_2O transport, which explains the appearance of dT/dx in equation (C.2). We approximate dT/dx by

$$\frac{dT}{dx} = \frac{(1/2)(E_h - V_{cell})}{k_{eff}^T} \qquad \text{(C.3)}$$

The greatest drop in c_g^{H2O}, and correspondingly, the greatest value of N_g^{H2O}, will be realized for a large drop in MeOH concentration across the anode diffusion media (see figure 3.4). Likewise, the approximation given by equation (3.19) will be poorest for more concentrated fuel. This being the case, out of all of the cases simulated in this thesis, the aTB MEA and operating conditions given in table A.3 should yield the greatest error due to the two assumptions in question. We therefore choose this case (given by table A.3) to compare results from the original model with those from our updated model.

Figure C.1 gives the MeOH concentration profiles across the anode diffusion media at i = 175 mA cm^{-2} for the original code and the updated code. From this plot we see that the maximum difference between the profiles is ~ 1%, as a fraction of total change in MeOH concentration over the anode diffusion media. Figure C.2 gives the plot of MCO versus current density. Here we see a maximum difference between the two curves of ~ 3% over the entire range of MCO (0-1). Finally, Figure C.3 shows the plot of α versus current density. Again, here we see a maximum difference between the two curves of ~ 6%, based on the total change in α.

The discrepancies between the results from the original and updated models are "small" with respect to the nature of our model. These results prove that the assumptions made in equations (3.3) and (3.19) do not induce an appreciable amount of error for the cases simulated.

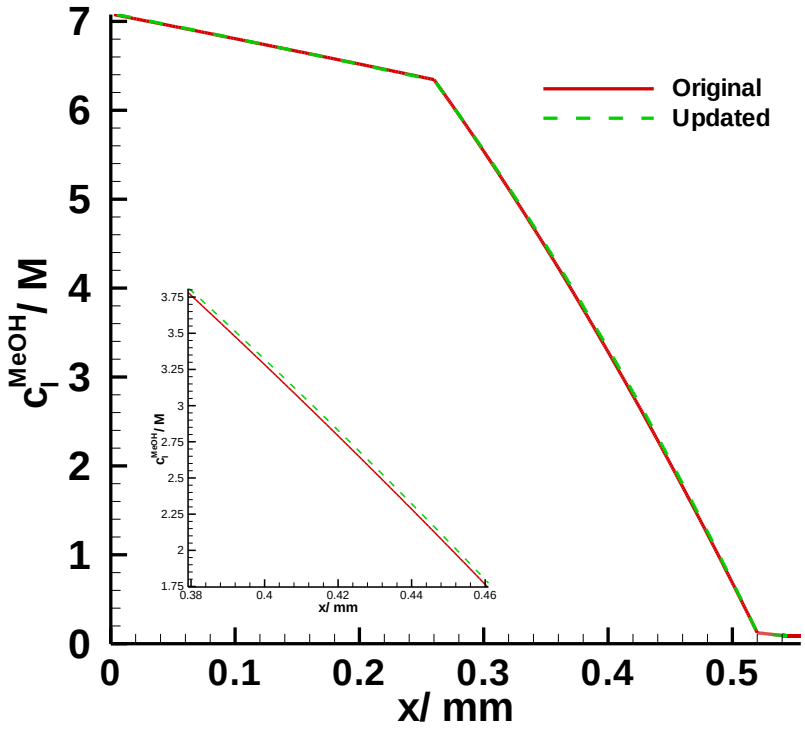

Figure C.1. MeOH concentration profiles on the anode side of the cell for the original and updated models; i = 175 mA cm^{-2}; cell properties and simulation parameters given in table A.3.

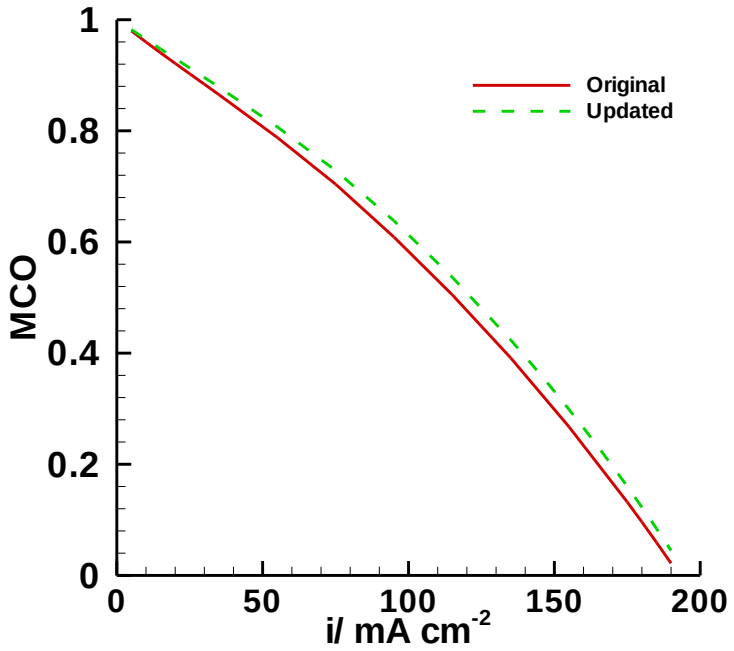

Figure C.2. Methanol crossover ratio (MCO) versus current density for the original and updated models; cell properties and simulation parameters given in table A.3.

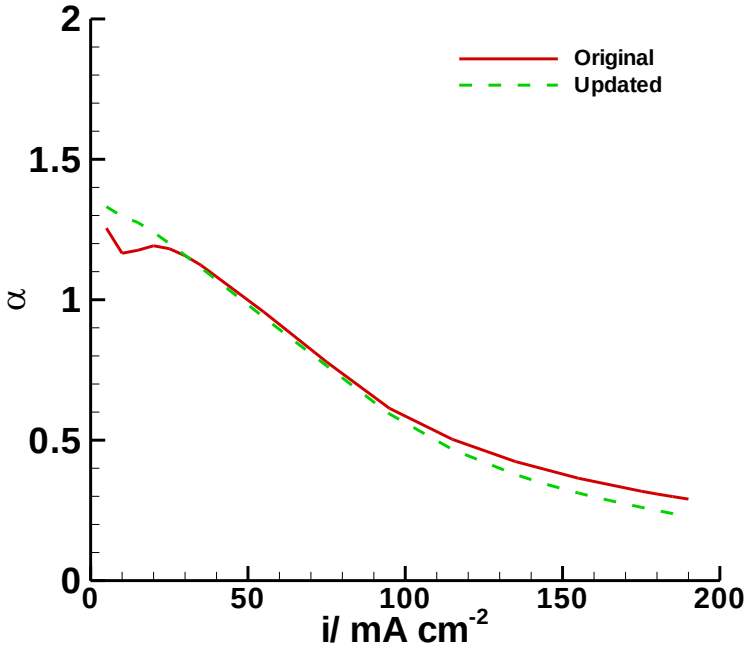

Figure C.3. Net water transport coefficient (α) versus current density for the original and updated models; cell properties and simulation parameters given in table A.3.

Vita

Christian E. Shaffer

Education:

The Pennsylvania State University, **Ph.D. Mechanical Engineering**, 2010
West Virginia University, **M.S. Mechanical Engineering**, 2005
West Virginia University, **B.S. Mechanical Engineering**, 2003

Experience:

Graduate Research Assistant, Penn State, May 2006 - August 2010
University Graduate Fellow, Penn State, August 2005 - May 2006
Graduate Research Assistant, West Virginia University, May 2004 - August 2005
Graduate Teaching Assistant, West Virginia University, January 2004 - May 2004

Peer-Reviewed Publications:

C. E. Shaffer and C. Y. Wang, manuscript to be submitted to J. Power Sources
C. E. Shaffer and C. Y. Wang, J. Power Sources 195, 4185 (2010)
C. E. Shaffer and C. Y. Wang, Electrochim. Acta, 54, 5761 (2009)
C. E. Shaffer and C. Y. Wang, 'Performance Modeling and Cell Design for High Concentration Methanol Fuel Cells,' in "Handbook of Fuel Cells, 6," H. A. Gasteiger, W. Vielstich, and H. Yokokawa, (eds.), John Wiley and Sons, pp. 749-761, Chap. 50 (2009)
I. B. Celik, J. Li, G. Hu, and **C. Shaffer**, J. Fluids Eng., 127, 795 (2005)

Professional Affiliations:

The Electrochemical Society (ECS)
American Society of Mechanical Engineers (ASME)